Title

Anisotropic Deformation Mechanisms of Stress Relaxation in Zircaloy-4 Cladding from Pellet-Cladding Interactions

Author

Nelson, Malachi

Publication Date

2024

Peer reviewed|Thesis/dissertation

Anisotropic Deformation Mechanisms of Stress Relaxation in Zircaloy-4 Cladding from Pellet-Cladding Interactions

By

Malachi Nelson

A dissertation submitted in partial satisfaction of the

requirements for the degree of

Doctor of Philosophy

in

Engineering – Nuclear Engineering

in the

Graduate Division

of the

University of California, Berkeley

Committee in charge:

Peter Hosemann, Chair
David Kamerman
Grace Gu
Guanyu Su

Summer 2024

Anisotropic Deformation Mechanisms of Stress Relaxation in Zircaloy-4 Cladding from Pellet-Cladding Interactions

Abstract

Anisotropic Deformation Mechanisms of Stress Relaxation in Zircaloy-4 Cladding from Pellet-Cladding Interactions

by

Malachi Nelson

Doctor of Philosophy in Engineering – Nuclear Engineering

University of California, Berkeley

Peter Hosemann, Chair

Increases to reactor power cause fuel pellet thermal expansion which can impose strain generating high stresses in the cladding and potentially lead to a breach in the fuel system. This phenomenon is known as a pellet-cladding interaction and the stress accumulation and retention during such an event is highly relevant to the fuel performance. This dissertation investigates the anisotropic deformation mechanisms controlling mechanical behavior of cold-worked stress-relieved Zircaloy-4 under pellet-cladding interaction conditions through mechanical testing, microstructure characterization, and stress analysis. Two loading modes are used to compare the effects of different stress states. These include axial tension which is commonly used to measure the mechanical properties, and internal pressurization loading which better simulates pellet-cladding loading conditions. It is hypothesized that the cladding subjected to internal pressure loaded will display enhanced stress relaxation due to increased stress and defect accumulation during loading and more competitive slip system activity during relaxation. Results confirm these hypotheses and find that the rate-limiting deformation mechanism during relaxation is screw dislocation glide on prismatic planes limited by edge dislocation jog and dipole climbing on basal planes. Differences in stress and defect accumulation are observed and do affect the stress relaxation behavior, but the dissertation finds that the primary reason for enhanced relaxation is because internal pressure loading imposes higher resolved shear stresses on basal slip systems which accelerates the rate-limiting deformation mechanism.

Contents

List of Figures

List of Tables

Acknowledgements

Peter, your persistent support, insight, and mentorship has changed me from a mechanical engineer to a materials scientist in a way that continues to fundamentally change my perspective on how things work. I began this degree during a global pandemic, in a research group that did not work, and in a city drowned in wildfire smoke. I cannot express the gratitude I have for the trust you showed in giving a second chance at this degree. It has been an honor to learn from you.

David, my research with you at Idaho National Laboratory has far exceeded any scenario I could have imagined or hoped for. I am so grateful for your practical and sincere mentorship that helped me learn to focus on what is important while your trust enabled me to become an independent researcher. Your unwavering support has been instrumental in my success and the ability to remain in Idaho means the world to me. I am honored to be graduating from the University of California, Berkeley, but my heart has always been in the mountains over any city.

Chai, Chris, and Darren – I treasure our limited time together as Peter's pirate crew and all the experiences we had together, some things cannot be forgotten. Ryan, Sasha, Christian, and Michael – our shared experiences and especially your continued friendship mean so much to me, you continue to inspire me.

Shmuel, your dedication and generosity has made collaboration with you a highlight of this degree and I have learned so much from you; I am honored by your mentorship and hope we continue to collaborate throughout our careers. Boone, your mentorship, insight, and friendship in all topics from research to life means the world to me. Alex, thank you for all the lessons learned and fun times we had in the sample preparation laboratory, you always can make me smile.

To all the friends I have been able to share adventures in Idaho with, throughout all the ups and downs of my academic journey and career, my time spent with you has made the past few years have been the most rewarding and exciting of my life so far. As life for all of us continues to change, I hope our adventures and friendship never change.

To my family, your continued encouragement has helped me through the most difficult parts of my academic journey. I would not be where I am today without everything you have done for me. To Heather, our shared academic journey has been a unique challenge and pleasure. I love you.

Chapter 1 Introduction

1.1 Motivation

Reliable electricity production and distribution is a critical piece of infrastructure that many industries and consumers depend on. The International Panel on Climate Change recommends renewable wind and solar energy as primary components of a decarbonized electricity production system but includes nuclear energy as an important addition for environmental, social, and technical reasons1 [1]. The U.S. has traditionally operated the existing nuclear reactor fleet at constant power in base load mode to reduce complexity and uncertainty and because fossil fuels such as natural gas provide more attractive load following capabilities. In this context, reactor power increases when reactors are ramped from low power modes used to conserve fuel when electricity is abundant or from zero power after an outage due to refueling or maintenance. However, decarbonization efforts motivate more frequent load following reactor power changes to better meet electricity demand without fossil fuels or excessive energy storage.

Light water reactor (LWR) cores use uranium dioxide (UO2) fuel pellets approximately 1 cm in height and diameter which are stacked in a zirconium alloy cladding tube that is sealed at the ends providing the first layer of radiological containment. Increases to reactor power necessitate raised fuel temperatures to increase heat transfer from the core. Thermal expansion in the UO2 fuel pellets can impose strain and generate high stresses in the cladding, a phenomenon known as a pellet-cladding interaction (PCI) [2], [3]. Such stress conditions can potentially lead to a breach in the fuel system and the release of radionuclides to the coolant water. A mitigation study concerning these mechanisms in cladding recognize that, “[the] role of stress is very important: time to failure increases as the stress decreases” [3].

Reactor power changes are carefully regulated to minimize PCI effects by limiting ramp rates, magnitudes, and frequencies, and employ conditioning periods to allow stress in the cladding to relax [4], [5]. These conditioning periods are crucial to reduce maximum stresses generated in the cladding and improve its ductility, thereby enhancing the fuel system's durability. However, they also limit the reactor's operational flexibility and power production motivating optimization of the costs and benefits [4], [6], [7]. Figure 1-1 shows a schematic representation of the relationship between reactor power and cladding stress in PCI conditions and how conditioning periods are used to benefit it. The axial to hoop stress ratio, hereafter defined as the stress state, in the cladding from a PCI has been measured with the axial to hoop stress ratio between 0.5-1.0 with RIA conditions producing a stress state between 0.7-0.8 [8], [9].

[1] A brief discussion included in Chapter 8 Section 1 provides additional context to the technical aspects motivating nuclear energy as an important energy source in a decarbonized energy market.

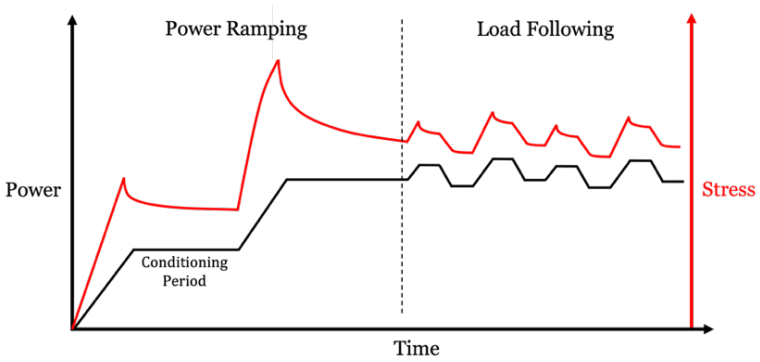

Figure 1-1: Schematic representation of the relationship between reactor power and cladding stress. Power ramping from low power is shown interrupted by a conditioning period used to allow cladding stresses to relax. More frequent power changes during load following typically have lower power change magnitudes.

PCI are most relevant when the fuel and cladding are in direct contact because any change in temperature imposes strain and stress in the cladding. Fuel rods are fabricated with a small gap between the fuel pellet and the cladding to help mitigate PCI effects, but fuel swelling and cladding creep-down closes the fuel-cladding gap at relatively low burnup (~20 GWd/MTU) [4], [10]. A majority of the operational life of a fuel rod occurs when the pellet-cladding gap is closed, and increased fuel efficiency and economic benefits motivate increasing burnup limits further [7], [10]. Therefore, it is increasingly important to understand the deformation mechanism affecting stress in PCI conditions to reduce uncertainty related to these failure mechanisms.

High burnup fuel rods and flexible power generation can improve LWR economics and better support large-scale energy systems, but these advancements necessitate careful consideration of safety implications [4], [6], [7], [10]. This dissertation investigates the deformation mechanisms controlling stress relaxation in zirconium alloy cladding during PCI events. This research aims to reduce uncertainty concerning stress accumulation and retention relevant to failure mechanisms with the aim of informing conditioning period optimization and flexible power generation efforts.

1.2 Zircaloy Nuclear Fuel Cladding

Zirconium alloys, commonly referred to as Zircaloys, are widely used in LWR cladding applications due to their very low thermal neutron absorption (Zr thermal neutron cross section = 0.186 barn) [11], acceptable strength, and good corrosion properties in LWR temperature water [12]. Cladding alloy development has led to two primary Zircaloys, Zircaloy-2 (Zry-2) and Zircaloy-4 (Zry-4) that are optimized for BWR and PWR conditions, respectively, as well as other alloys such as multiphase Zr-Nb and numerous proprietary and even composite layered Zry alloys [13], [14], [15].

Zry-2 and Zry-4 are similar with minor differences in elemental compositions shown in Table 1-1. Cladding tubes dimensions also depend on the reactor design with BWR tubes being slightly larger (⌀ 10.0-12.3 mm, δ 0.660-0.813 mm) than PWR tubes (⌀ 9.4-12 mm, δ 0.6-0.8 mm) [14], [16]. These dimensions are near the diameter-to-thickness ratio that enable thin wall stress analysis which have been validated and are extensively used in literature, so are used for analysis in this dissertation [17], [18], [19], [20], [21], [22], [23], [24]. This dissertation focuses on Zry-4

cladding because PWRs account for approximately two-thirds of the LWRs in the U.S. and a majority of the LWRs worldwide, but much of the analysis is relevant both cladding types [25].

Table 1-1: Alloying element composition of Zry-2 and Zry-4. [14]

	ASTM	Zr	Sn	Nb	Fe	Cr	Ni	O
Zry-2 [wt%]	R 60802	bal.	1.2-1.5	-	0.07-0.2	0.1	0.05	0.12
Zry-4 [wt%]	R 60902	bal.	1.2-1.7	-	0.18-0.24	0.1	-	0.1-0.14

PWRs operate with high pressure primary coolant (14.5-15.5 MPa) that increases from ~280 °C to ~320 °C between the coolant inlet and outlet [10], [26], [27]. PWR burnup limits range between 62-70 GWd/MTU due to fuel and cladding degradation, limiting fuel enrichment to 4-5% [10], [16]. The cladding temperature depends on many factors including the linear heat generation rate (LHGR), fuel-cladding gap, burnup, radial position in the cladding thickness, axial position in the fuel rod, and fuel rod position in the core, but PWR cladding temperatures during normal operation generally range from 300 – 450 °C [16], [27], [28]. Cladding strain is limited to 1% uniform strain under normal operating conditions by regulation but can reach 5% strain during design-basis accident (DBA) conditions [3], [10]. This dissertation focuses on cladding behavior in a normal PWR operating environment to help limit the scope of this analysis, but much of the analysis is relevant to DBA conditions. Irradiation effects are an essential consideration for in-core materials such as cladding, but this dissertation is limited to unirradiated materials with the aim of informing future irradiation testing and providing baseline behavior for comparison.

1.2.1 Crystal Structure

Zry-4 maintains hexagonal close-packed (HCP) α-phase below 810 °C and transitions to a body-centered cubic (BCC) β-phase at 910 °C with an intermediate α+β phase: $\alpha \rightarrow \alpha + \beta \rightarrow \beta$ [29]. The HCP unit cell lattice parameters, a and c, vary locally with alloying elements, so the lattice parameters of pure Zr are reported: S.G. No., 194, $P6_3/mmc$, a = 3.2332(4), c = 5.1466(10) Å [30]. The thermal expansion coefficients of pure Zr are reported for similar reasons: 5.2 and 10.4 E-6/K for the a and c parameters, respectively [31]. The melting temperature of Zry-4 is 1850 °C [32]. The HCP unit cell is shown in Figure 1-2 depicting three primary glide planes in Zr [12], [33], [34], [35]. The β-phase is relevant to the manufacturing process discussed in Section 1.2.2, but discussion is generally limited to the HCP α-phase for this dissertation.

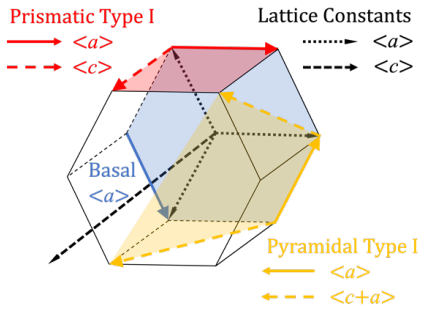

Figure 1-2: Schematic representations of the HCP unit cell with primary glide planes: red, blue, and gold planes colors designate the prismatic, basal, and pyramidal glide planes, respectively.

The crystal structure affects three well-established laws governing the slip behavior of metals which are summarized by Erich Tenckhoff [12] as follows:

a) *The slip plane is normally the plane whose interplanar spacing, that is, whose atomic density, is relatively the largest.*[2]
b) *The slip direction is nearly always the one that contains the shortest Burgers vector.*[2]
c) *From a given set of slip planes and directions, the crystal operates on that system (plane and direction) for which the difference between the resolved shear stress and the critical resolved shear stress is largest.*[2]

The *c/a* ratio strongly affects HCP metals because it defines the glide plane with the highest atomic density, and an ideal sphere packing ratio equal to 1.633 serves as an inflection point for distinct deformation behavior [12]. Zr has a *c/a* ratio of 1.593 resulting in the highest atomic density on the prismatic plane which, thus, is the primary slip plane according to law a) [12], [14]. The <*a*> slip direction is much smaller than the <*c*> direction, permitting much easier slip according to law b). However, slip with a <*c*> component is often required to ensure continuum plasticity and the pyramidal <*c*+*a*> system has been found most active to accommodate this strain component [12], [15], [36], [37], [38], [39]. The critical resolved shear stress (CRSS) of each system is strongly affected by laws a) and b), and with the resolved shear stress (RSS) defined by the applied stress orientation with respect to the slip system orientation, results in law c). Deformation mechanisms resulting from the HCP crystal structure are discussed in more detail in Section 1.3.

1.2.2 Manufacturing

Several thermo-mechanical processes are employed to produce the best seamless Zry cladding possible. First, the Zry ingots are forged to produce tube shaped 'shells', generally above 1000 °C to process the cubic β phase which also permits full homogenization of alloying elements [14], [40]. The shell is water quenched from the β phase which produces α-phase basketweave, or Widmannstätten, microstructure which improves mechanical and corrosion properties [41]. The shells must be at least 10 cm thick because of oxidation kinetics above 1000 °C which requires several more reduction steps to produce cladding dimensions [14]. Drawing, extruding, and pilgering processes can be used to reduce the shell thickness and homogenize precipitate distribution, but the process must be performed iteratively with annealing treatments between 530-600 °C to recrystallize (RX) the material and restore ductility in between reduction steps [14], [41].

Deformation mechanisms active during α-phase processing cause basal planes to reorient in the flow direction to allow <*a*> slip [38], [42], [43]. This produces particularly strong basal texture during shell reduction that is dependent on the method used to reduce the shell to cladding dimensions. Drawing and extrusion methods produce basal texture with a circumferential fiber while pilgering produces basal textures with a radial fiber [15]. Hydrides form on basal planes, so drawing and extrusion methods cause hydrides to form with radial orientations, greatly weakening the cladding, while pilgering causes hydrides to form circumferentially which is less detrimental to the cladding strength [15]. Further, basal texture in the radial direction forces radial strain to occur *via* slip with a <*c*> component which greatly increases the cladding resistance to thinning [12], [15]. Therefore, pilgering in the α-phase is used during the final steps of cladding production

[2] Direct quote from [12].

to produce and retain this texture. In addition to basal texture, pilgering develops a prismatic $\{10.0\}$ fiber in the rolled direction [12], [15]. Pilgering must achieve a thickness-to-diameter reduction ratio greater than one to change the extruded texture to pilgered texture [40].

After the final pilgering step, the cladding is annealed to relieve residual stresses and improve the mechanical properties. Recrystallization causes the basal planes to rotate by ± 30° about the *c*-axis changing the rolled direction fiber from $\{10.0\}$ to $\{2\bar{1}.0\}$ [12], [15]. Annealing can occur at 550-570 °C to achieve fully recrystallized (RX) microstructure and higher ductility or near 475 °C to achieve higher strength by retaining cold worked (CW) microstructure [14], [32]. PWR Zry-4 cladding commonly uses the latter, cold-worked stress-relieved (CWSR) annealing process because CW significantly increases the cladding strength which is especially beneficial for higher PWR temperatures [32]. This dissertation uses CWSR cladding, but much of the analysis is relevant to RX cladding also because both annealing treatments retain similar basal texture. The microstructure following each step of the manufacturing process is shown using scanning electron microscope (SEM) electron backscatter diffraction (EBSD) inverse pole figure (IPF) micrographs in Figure 1-3.

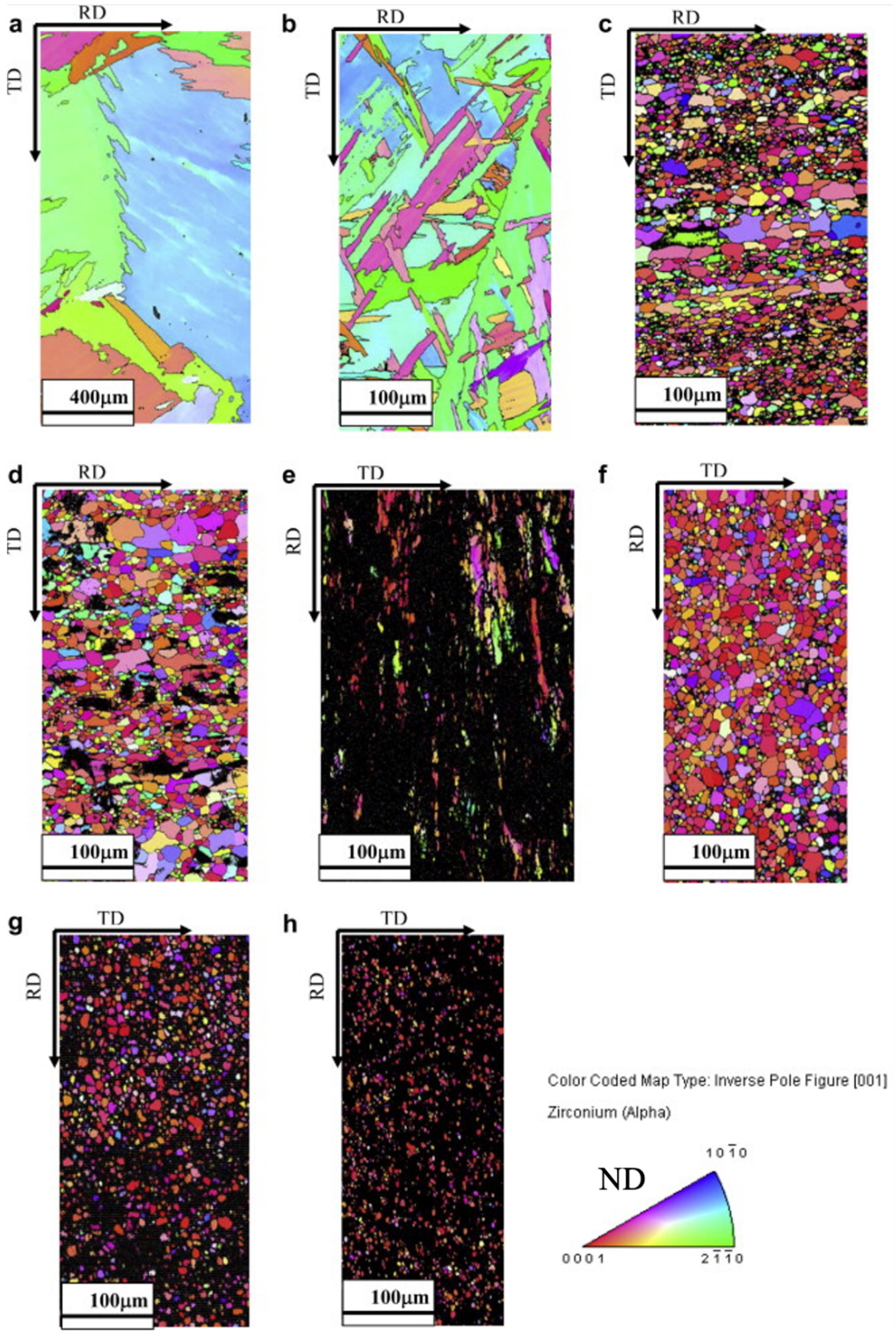

Figure 1-3: EBSD micrographs of (a) as cast (b) β-quenched, (c) hot extruded, (d) first annealed, (e) first pilgered, (f) second annealed, (g) third annealed and (h) final annealed. Images were plotted using inverse pole figure convention – grain boundaries being marked for above 15° misorientation. Measurement points with confidence index (an approximate measure of accuracy of indexing) values below 0.03 are marked as black. RD & TD correspond respectively to axial and hoop directions of the tube. [44].

1.2.3 Microstructure

Pilgered cladding tubes and rolled plates have the same orthogonally anisotropic microstructure with well-defined crystallographic texture fibers. This similarity permits rolled plate mechanical testing to enable more traditional mechanical testing techniques which are extensively used in literature [34], [42], [45], [46], [47], [48], [49], [50], [51], [52], [53], [54], [55], [56], [57], [58], [59], [60]. Cartesian coordinate systems are used to refer to the microstructure characteristics that are relevant to pilgered tube and rolled sheet while cylindrical coordinate systems are used to refer to characteristics relevant to the cladding tube geometry. These correspond to each other as shown in Figure 1-4: the rolling direction (RD), transverse direction (TD), and normal direction (ND) form the Cartesian coordinate system of material anisotropy which correspond to the axial (z), hoop (θ), and radial (r) axes of the cladding tube, respectively.

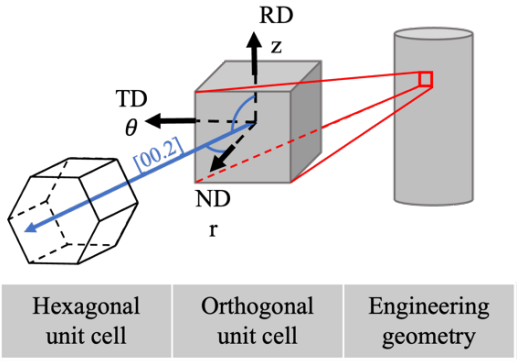

Figure 1-4: Schematic relationship of the cladding coordinate system showing an HCP unit cell with the basal glide plane unit normal in a common orientation.

Pilgering and rolling textures depend on whether the *c/a* ratio is above or below the ideal packing factor and the thickness reduction ratio as shown in Figure 1-5 (a) – (c) [12]. Pole figures are extensively used to visualize texture intensity which require at least two systems to define the preferred lattice orientation and are commonly shown for the RD-TD plane with the RD axis in the vertical direction [12], [14], [15]. In Zry cladding, the basal intensity shown in Figure 1-5 (c) is particularly strong because of the deformation mechanisms discussed in the previous section. The tube reduction ratio controlling the spread of high intensity basal orientations is more variable between manufacturers and can be observed in any of the states shown in Figure 1-5 (d) – (f) [12], [14], [15], [36], [40], [47], [61]. However, it is most common to see high intensity basal peaks at ± 30° from normal in the TD with a peak basal intensity of 4-6 times random [12], [14], [15].

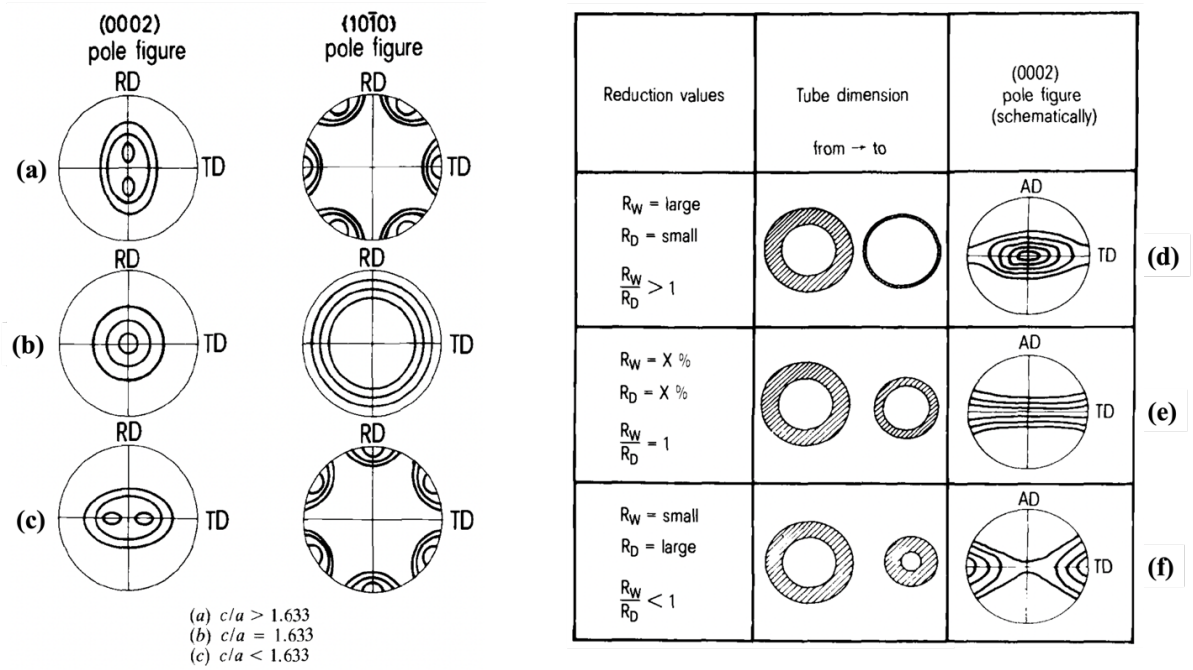

Figure 1-5: Rolled sheet or pilgered tube textures in HCP metals shown schematically using pole figures (PFs) with intensity iso-lines [12]. (a) – (c) shows effect of different c/a ratio, (d) – (f) shows effect of tube reduction ratio.

After pilgering the cladding to final dimensions, the final heat treatment used to produce CWSR or RX cladding produces slightly different microstructures. In general, RX heat treatment produces larger equiaxed grains with few defects or intragranular misorientation. RX grain size distribution depends on the length of heat treatment and whether the number fraction or area fraction is used, but grains generally vary between 3-15 μm with some larger grains near 30 μm [36], [47], [51]. CWSR heat treatment produces microstructure with bimodal grain structure with grains varying from < 1-12 μm including elongated grains with significant intragranular misorientation and equiaxed grains with low intragranular misorientation [36], [61], [62], [63], [64]. Representative microstructures are shown in Figure 1-6 for RX and CWSR heat treatments.

SEM-EBSD is an excellent method to describe the microstructure because it provides the local orientation of the SEM interaction volume showing both intra- and inter-granular data using micrographs as shown in Figure 1-6. However, EBSD is notoriously difficult for Zircaloys, particularly those with CWSR microstructure including small grains and high intragranular misorientation causing low index rates demonstrated in Figure 1-3 (h) and other work [44], [64], [65], [66]. In the current literature review, only two satisfactory EBSD IPF micrographs have been found for CWSR Zry-4 cladding[3]: one is performed on the TD-ND plane revealing axial cross section [62], and one is performed on the RD-TD plane revealing the radial cross section which is shown in Figure 1-6 (b) [63]. Therefore, it is a goal of this dissertation to acquire satisfactory EBSD characterization of CWSR Zry-4 cladding microstructure.

[3] It is noted that Shi et al. [61] achieved excellent EBSD characterization of a CWSR alloy similar to Zry-4 with similar microstructure, and Deng et al. [36], [45], [67] and Fuloria et al. [68] achieved excellent EBSD characterization of a Zry-4 shell at different stages of pilgering which is not representative of cladding microstructure.

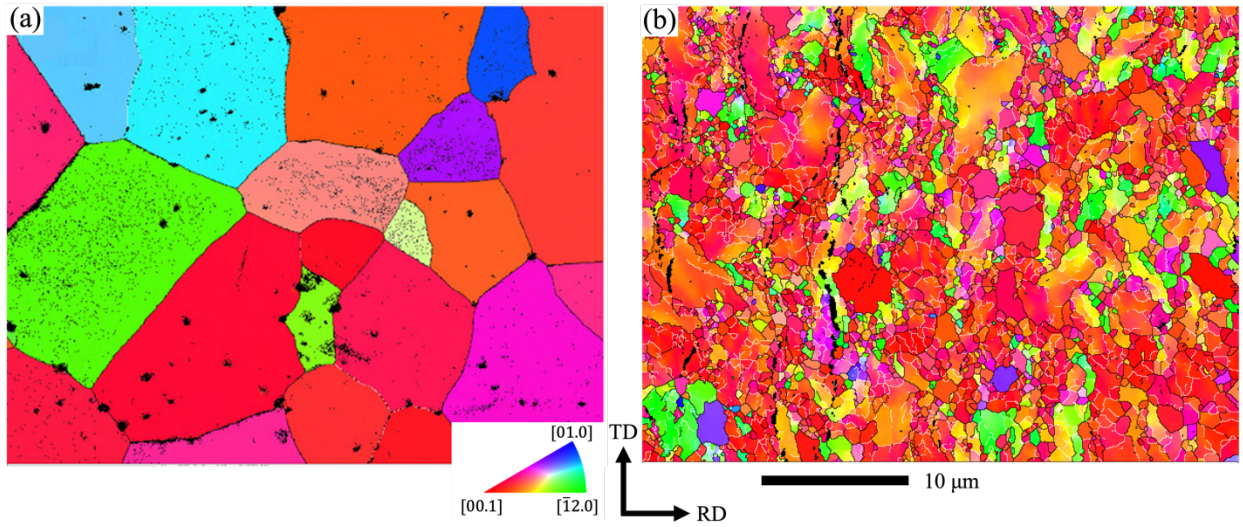

Figure 1-6: EBSD IPF micrographs for (a) RX Zry-4 plate [66] and (b) CWSR Zry-4 cladding [63].

1.3 Deformation Mechanisms

Deformation mechanisms in HCP metals such as Zircaloy are inherently anisotropic at the lattice scale due to the low-symmetry structure discussed in Section 1.2.1. The strong basal texture produced during manufacturing discussed in Sections 1.2.2 and 1.2.3 compounds the effects of the lattice-scale anisotropy, producing strong mechanical anisotropy observed at the macroscopic scale. Therefore, the loading conditions, such as tension versus compression or load orientation with respect to the texture fiber, can produce significantly different deformation mechanism activities. These deformation mechanisms controlling the material response to loading are introduced and discussed in this section. A general introduction is provided to limit the length and complexity of this section, but more specific deformation mechanisms are introduced and discussed in detail in the Chapter 4 and 5. Much of the material in this section is fundamental materials science summarized from the following books and lectures [69], [70], [71], [72], [73], [74], [75], and references are used sparingly for brevity.

1.3.1 Microstructure Defects

Crystal lattices form because they provide stable, or low energy, states for the material under relevant thermal and stress conditions. The thermodynamics and solid-state physics controlling lattice properties is out of the scope of this dissertation, however, it is helpful to consider a perfect crystal lattice as the lowest energy configuration. Therefore, the defects discussed in the following subsections store a quantity of energy in the material which is defined as the defect energy. Although the inclusive term ‘defect’ is used, dislocations are the defect most relevant to the deformation behavior in this dissertation and their properties are discussed in more detail.

1.3.1.1 Dislocations and Slip

Deformation in metals usually occurs by a mechanism known as slip, where a volume of atoms in the lattice slides past another volume on the slip plane (also commonly referred to as the glide plane) to achieve a shear displacement. Taylor and Orowan found that the theoretical strength of crystalline materials did not match the measured strength because deformation occurs *via* a wave-like propagation of the slipped-unslipped volume interface on the glide plane. This interface forms a one-dimensional defect in the lattice called a dislocation. Dislocations remain in the material when slip only occurs on part of the glide plane as shown in Figure 1-7. Because dislocations propagate slip, dislocations properties strongly affect the deformation behavior of the material.

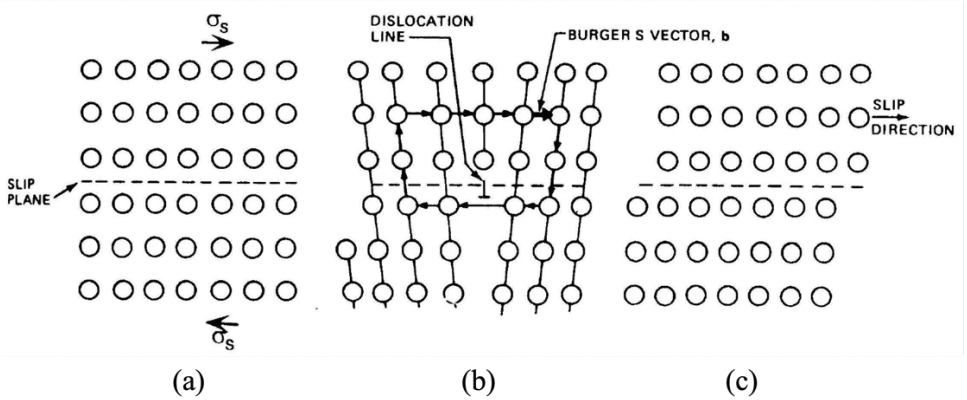

Figure 1-7: Schematic of edge dislocation slip. (a) shows an undeformed crystal lattice with RSS (σ_s), (b) shows an edge dislocation when slip occurs on part of the slip plane, and (c) shows slip completed on the entire glide plane, allowing the dislocation to annihilate at an interface [72].

The Burgers vector (b) is defined as the direction and magnitude of displacement that a dislocation produces in the material. Dislocations with line vectors perpendicular to the Burgers vector are known as edge dislocations and can only move along a single direction parallel to the RSS as shown in Figure 1-7. Dislocations with line vectors parallel to the Burgers vectors are known as screw dislocations and glide perpendicular to the RSS, like a tearing sheet of paper, so can glide on any plane perpendicular to the dislocation line vector. Both dislocation types are often active and multiple dislocations can work together forming mixed dislocations known as kinks if they occur on the same glide plane or jogs if they traverse multiple glide planes.

Lattice strains from dislocations produce local stress fields along the dislocation line vectors as shown in Figure 1-8. Dislocation production requires more stress than dislocation movement because a portion of the stress is stored in the dislocation stress field and does not contribute to motion. Dislocation annihilation is energetically favorable because it dissipates the dislocation stress field, and some dislocation structures such as loops, jogs, and dislocation cells can form because they reduce the stress stored in the lattice compared to individual dislocations. The compressive and tensile stress fields surrounding the dislocation interact with the lattice and other defects such as point defects and other dislocations which can reduce dislocation mobility. When many dislocations are present, repulsive forces between dislocations preventing their motion can produce a phenomenon known as forest hardening which increases the stress required to deform the material. Thus, while mobile dislocations are necessary to propagate deformation, immobile dislocations can prevent deformation.

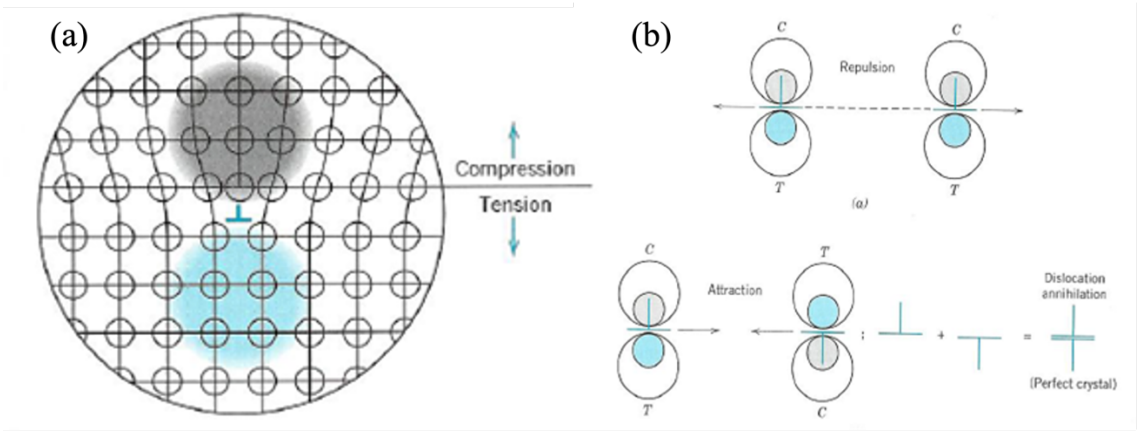

Figure 1-8: Local stress fields around dislocations and their interactions [72].

1.3.1.2 Twins

Twinning is a deformation mode through spontaneous lattice rotation that produces a shear strain with coherent interfaces [12], [15]. HCP metals are particularly susceptible to twinning because of the low-symmetry structure and limited slip systems, so are commonly referenced in Zircaloy literature [12], [15], [36], [37], [45], [52]. Twins for zirconium are shown in Figure 1-9 which produce well-defined lattice rotation to retain coherent twin boundaries. Twinning in can occur in tension but more commonly occurs in compression along the *c*-direction and at low temperatures where slip activation is less favorable [38], [43], [47]. In this dissertation, cladding is tested in tension at room temperature or higher so twinning is not expected [36], [38], [43], [47]; moreover, twinning cannot contribute to stress relaxation in HCP metals [76]. Therefore, further discussion of twinning is limited.

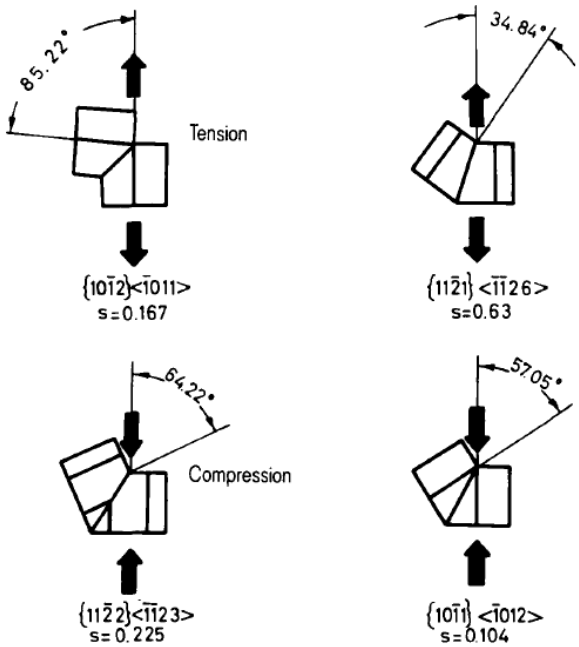

Figure 1-9: Schematic of the twinning systems in zirconium [12].

1.3.1.3 Point Defects

Point defects include substitutional atoms, interstitial atoms, self-interstitial atoms, and vacancies. Zry-4 contains a small percentage of solid solution alloying elements discussed in Section 1.2 which are larger (e.g. Sn) or smaller (e.g. Fe) than Zr, producing minor strains in the lattice structure that impede dislocations and increase mechanical strength. Similarly, interstitial atoms such as H and O produce strains in the lattice and impede dislocations, increasing the strength of the metal. However, interstitial atoms diffuse much easier allowing them to preferentially migrate to areas of tensile strain in the lattice, causing phenomena such as delayed hydride cracking [77]. Self-interstitial atoms and vacancies are produced in great numbers during irradiation and remain in equilibrium solubility concentrations dependent on the temperature of the metal. Vacancies are particularly important for dislocation mobility because they allow dislocations to move in the direction of their line vector and bypass obstacles if they are unable to glide. This movement mode is known as dislocation climb and is discussed further in Section 1.3.2.3.

Point defects pin dislocations in place until they achieve high enough stress for breakaway to occur or the defects diffuse with the dislocation, both effects producing a drag force on dislocation mobility. Figure 1-10 shows this with a dislocation pinned to the diffuse point defects in (a) which bows out under stress in (b) with a solute breakaway marked with the dashed line, B. Figure 1-10 (c) shows concentrated point defects which can occur when mobile point defects such as interstitials are attracted to the dislocation stress fields. A cloud of solute atoms known as a Cottrell atmosphere can form around the dislocation which produces an even larger pinning force than individual point defects. The reduction of dislocation mobility that Cottrell atmospheres cause a macroscopic hardening effect known as dynamic strain aging (DSA).

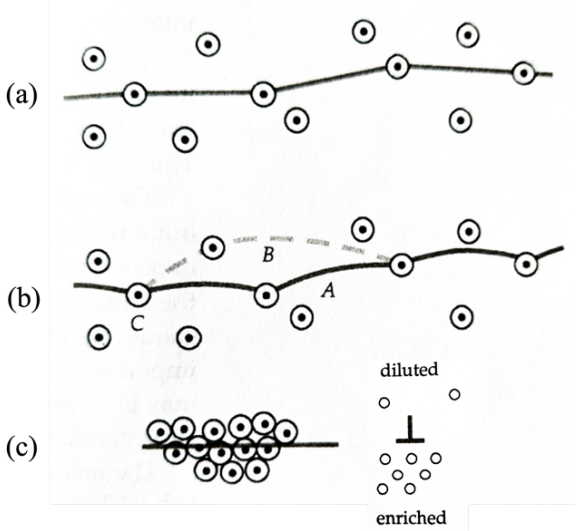

Figure 1-10: Interactions of a dislocation with solute atoms, with atoms represented by dots and their strain fields by circles: (a) dilute solution, (b) dilute solution under stress, (c) concentrated solution [70].

1.3.1.4 Grain boundaries

Grain boundaries are two-dimensional defects with properties strongly dependent on the grain boundary angle as shown in Figure 1-11 (a). Low angle grain boundaries (LAGBs) consist of many dislocations with complementary Burgers vectors compounding their misorientation as

shown in Figure 1-11 (b). These are coherent boundaries that have relatively low grain boundary energy, but the energy increases proportionately with the dislocation density. Higher angle grain boundaries near 10-15 ° begin to form incoherent grain boundaries which saturates the boundary energy reducing dependence on the misorientation angle as shown in Figure 1-11 (a). Grain boundaries are formidable barriers to dislocation motion causing dislocation pileup at grain boundaries and higher grain boundary density from small grains produces the Hall-Petch strengthening effect [78].

Deformation can produce strain gradients requiring geometrically necessary dislocations (GNDs) similar to the low angle boundaries shown in Figure 1-11 (b). At high strains [61], [79], or during creep [80], [81], these misorientation can form sub-grain cells with low-angle grain boundaries (LAGBs) as shown with the transmission electron microscope (TEM) micrograph in Figure 1-11 (c). The angles used to define grain boundaries in analysis can vary based on the nature of the analysis, length-scale of characterization, and author's preference, but usually angles between 5-15° are used [36], [44], [47], [62].

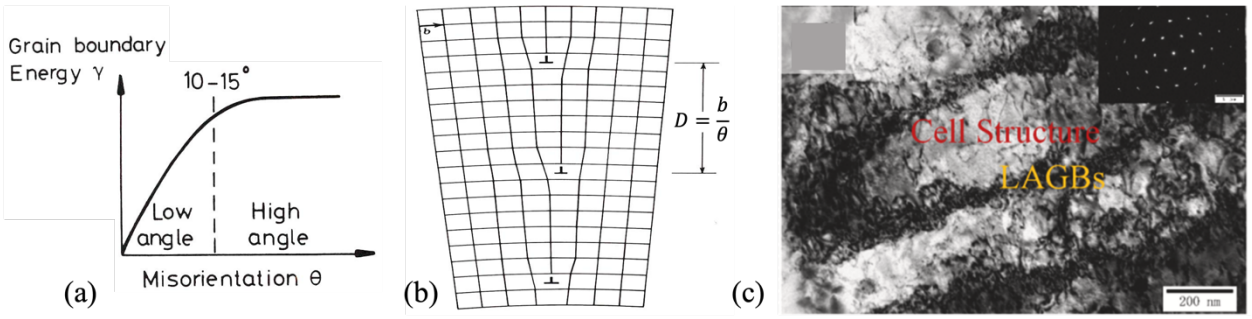

Figure 1-11: Schematics of (a) grain boundary energy dependence on misorientation angle and (b) low angle grain boundary consisting of multiple dislocations [72].

1.3.2 Material Response

Deformation occurs in a material when a force or displacement is applied, and the material response in metals is commonly divided into three categories: elastic, plastic, and viscoplastic. The regimes where these deformation categories are dominant are shown using a schematic representation of a stress relaxation test in Figure 1-12. Elastic deformation is recoverable and time-independent, plastic deformation is unrecoverable and time-independent, and viscoplastic deformation is unrecoverable and time-dependent. The effects of plastic and viscoplastic deformation are sometimes known collectively as inelastic deformation to reference unrecoverable changes made to the microstructure, especially at temperatures where both behaviors are present.

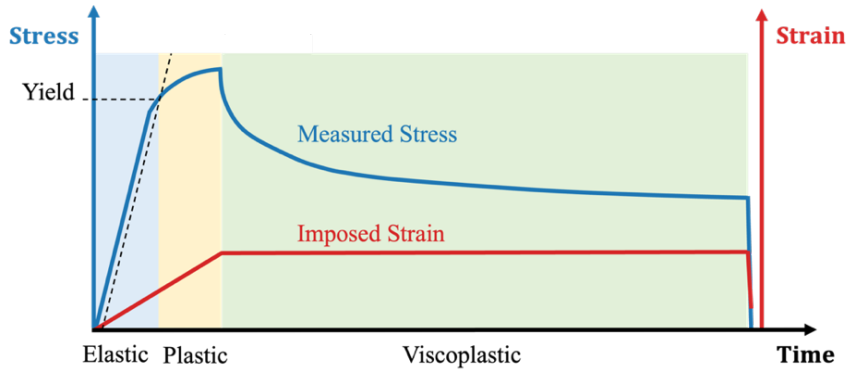

Figure 1-12: Schematic representation of a stress relaxation test using stress and strain versus time axes. Periods where elastic, plastic, and viscoplastic deformation is dominant are shaded and marked.

These phenomena can occur simultaneously and rheological models like those shown in Figure 1-13 show the compound effects of each element on the material response. Rheological models are especially helpful to discuss stress relaxation because significant deformation occurs while the macroscopic strain remains constant. Elements shown in Figure 1-13 (b) and (c) are used in series according to the Maxwell model where the stress is consistent, and the strain is summed over all elements. The elastic, plastic and viscoplastic material behavior represented by their respective rheological components have unique mechanisms and dependencies which are discussed further in the following sections.

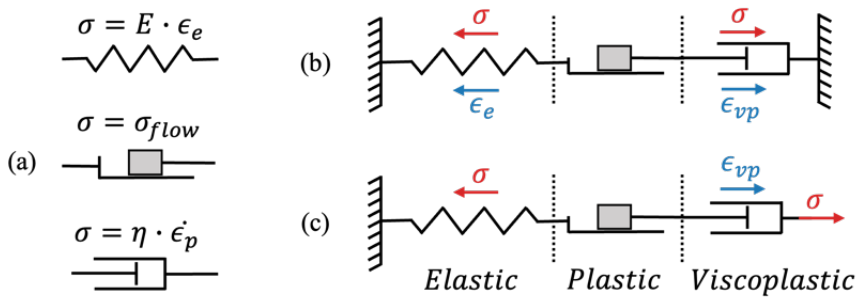

Figure 1-13: (a) Elastic, plastic, and viscoplastic rheological model components. (b) Rheological model for stress relaxation where opposite elastic and viscoplastic strains result in zero net strain. (c) Rheological model for creep where viscoplastic strain increases the total strain.

1.3.2.1 Elastic Response

Elastic deformation occurs when atoms are displaced from their ideal lattice positions, but not so much that they are removed from their current lattice positions. In other words, the applied load is below the CRSS required to activate deformation mechanisms that produce defects such as dislocation slip. Tensile loads stretch the metallic bonds and compressive loads compress them, producing a reactionary force to the applied load resulting in stress that resists elastic deformation. This also causes the material volume to change during elastic deformation. The stress persists while the load is applied, but when it is removed or reduced, the reactionary force returns atoms towards their ideal lattice positions and recovers the elastic strain. Because no defects are produced or activated, no energy is lost, and the process is reversable.

Elastic deformation is a proportional force-displacement relationship that stores work in the material according to Hooke's Law, like a spring which is the rheological element used to represent it. Work is a form of energy, and the energy stored in the material as elastic strain is calculated according to Equation 1-1 [69]. This energy is defined as the elastic energy in the material for this dissertation. In Equation 1-1, the elastic energy (ψ) is a scalar defined per unit volume, $\boldsymbol{\epsilon}^{\mathrm{e}}$ is the elastic strain tensor, and $\boldsymbol{\sigma}$ is the stress tensor.

$$\psi = \frac{1}{2}\boldsymbol{\epsilon}^{\boldsymbol{e}} : \boldsymbol{\sigma} \qquad \text{Equation 1-1}$$

Although Zry-4 displays anisotropic mechanical behavior, the elastic properties are relatively isotropic and are commonly simplified as such [19], [32], [41], [82], [83]. The elastic constants are commonly measured during mechanical loading using the linear region of the stress-strain relationship as shown in Figure 1-12, but they are more accurately measured using resonant beam techniques because elastic deformation is time-independent [75]. Although more accurate material constants are desirable, measurements made during mechanical loading are valuable to observe effective behavior and compare results to literature.

1.3.2.2 Plastic Response

Plastic deformation occurs when atoms are displaced enough to remove them from their current lattice positions, irreversibly dissipating energy and preventing strain recovery when the load is removed. When work is applied to a material through an applied force or displacement, the elastic response can only store a limited amount of energy before the material yields. The rheological model component for plasticity in Figure 1-13 reflects these characteristics using a sled that requires a threshold force for any displacement to occur. Excess energy from an applied load is stored in the material as defects or dissipated from the material as heat as shown in Equation 1-2 [69]. Here, W is work, $\boldsymbol{\sigma}$ is the stress tensor, $\dot{\boldsymbol{\epsilon}}$ is the strain rate tensor, t is time, E_e is the elastic energy, E_d is the defect energy, and D is dissipation.

$$W = \int \boldsymbol{\sigma} : \dot{\boldsymbol{\epsilon}}\, dt = E_e + E_d + D \qquad \text{Equation 1-2}$$

Plastic deformation propagates *via* dislocation production and slip which are strongly dependent on the lattice structure and slip system. The CRSS varies significantly in low-symmetry HCP metals and the three primary slip systems in Zr and Zry-4 are shown in Table 1-2, as introduced in Section 1.2.1. Glide planes are denoted using ( ) for a specific plane or { } for a family of planes, and slip directions are denoted using [ ] for a specific direction or < > for a family of directions. Table 1-2 employs the full Miller-Bravais indices but the rest of the dissertation uses the shorter Miller indices which are more commonly used in equations.

Table 1-2: Primary slip systems in Zry-4

Slip system	Glide Plane	Slip Direction
Basal <*a*>	(0002)	$\langle 11\bar{2}0 \rangle$
Prismatic Type I <*a*>	$\{10\bar{1}0\}$	$\langle 11\bar{2}0 \rangle$
Pyramidal Type I <*c*+*a*>	$\{10\bar{1}1\}$	$\langle \bar{2}113 \rangle$

Thermal energy can assist dislocation mobility by reducing the CRSS required for slip activation which affects distinct slip systems differently. CRSS values for zirconium and Zircaloys have been measured using single crystal tensile [33], microcantilever [84], and micropillar compression [35] experiments and have been calculated with self-consistent modeling in several other studies [34], [45], [59], [85], [86], [87]. Figure 1-14 shows these CRSS values plotted against temperature where available from the literature. Only Zry-4 and Zry-2 data have been plotted due to the high sensitivity to alloying elements and other phases in materials like pure Zr in [33], [84] or multiphase microstructure Zr2.5Nb used by [85]. Oxygen and hydrogen are known to significantly increase the CRSS of Zircaloys which may result in variability, even within the same alloy [14], [84], [88].

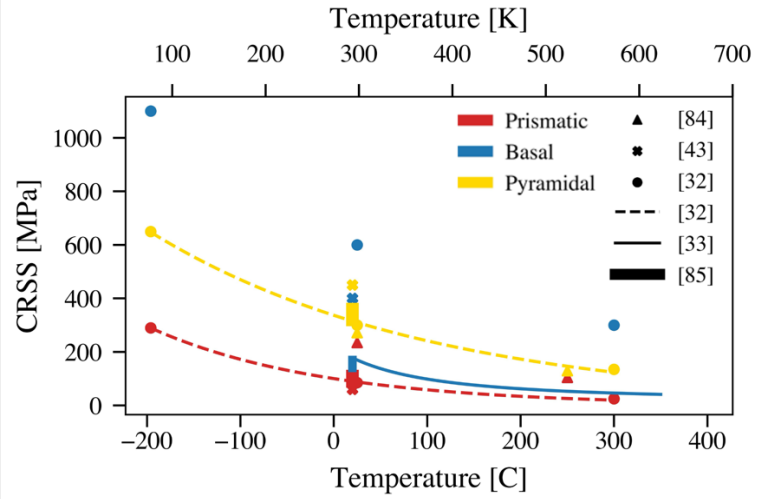

Figure 1-14: CRSS vs. temperature for prismatic type I <a> (red), basal <a> (blue), and pyramidal type I <c+a> (gold) from the literature.

Elastoplastic self-consistent polycrystalline modeling is employed by Xu et al. [59], [87] to derive CRSS value ranges for Zry-2 from mechanical testing at room temperature. Testing included an extensive set of tensile and compression loads with different stress states and *in-situ* neutron diffraction measurements, forming a validated resource for cross-referencing thermal dependence equations. These CRSS ranges included in [87] agree with the prismatic <*a*> and pyramidal <*c*+*a*> equations published Reddy et al. [34], and the basal <*a*> equation published by Wang et al. [35]. Reddy et al. [34] provides data with an equation for basal <*a*> CRSS, but it is extremely high which disagrees with other literature that consistently places basal slip in between prismatic and pyramidal <*c*+*a*> CRSS [12], [15], [48], [87]. This may be due to low basal activity in the compression-only data set leading to high uncertainty. The selected results also agree with [48] which also indicates the pyramidal <*c*+*a*> to prismatic <*a*> CRSS ratio increases with temperature even if the CRSS difference decreases with temperature. The temperature dependent CRSS equations provided by the authors are plotted as lines in Figure 1-14 with corresponding equations in Equation 1-3, Equation 1-4, and Equation 1-5 using absolute temperature [34], [35]. The temperature ranges are shown in Figure 1-14 as provided by the authors and are extrapolated to 400 °C for analysis.

$$\mathrm{CRSS}_{\mathrm{prismatic}\,<a>} = 439 \cdot exp\left(-\frac{\mathrm{T}}{185}\right) \qquad \text{Equation 1-3}$$

$$\mathrm{CRSS}_{\mathrm{pyramidal}\,<c+a>} = 837 \cdot exp\left(-\frac{\mathrm{T}}{300}\right) \quad \text{Equation 1-4}$$

$$\mathrm{CRSS}_{\mathrm{basal}\,<a>} = 11.3 \cdot exp\left(\frac{807.7}{\mathrm{T}}\right) \quad \text{Equation 1-5}$$

Plastic deformation is dependent on the dislocation density in the material because dislocations propagate deformation but can also harden the material *via* the forest hardening mechanism discussed in Section 1.3.1.1. The plastic flow stress increases with strain because of forest hardening and a high defect density in the initial microstructure can increase the yield strength through this mechanism. CWSR cladding exhibits high strength compared to RX cladding because the lower annealing temperature retains high dislocation density in addition to smaller grain size causing Hall-Petch strengthening. Varying defects, stress concentrations, and RSS distributions can cause microplasticity while the material appears to have a linear stress-strain relationship, but plasticity is practically defined when ductility allows the strain to intersect with a linear offset line as shown in Figure 1-12. Because plastic deformation occurs through defects that glide rather than stretching the lattice, it is considered a constant volume process.

Continuum mechanics are helpful in defining deformation in crystalline materials operating in three dimensions simultaneously by considering the displacement of arbitrary points, commonly lattice points, within the material as shown in Figure 1-15. Displacement gradients from plastic deformation can be decomposed into the symmetric and skew-symmetric components known as strain and material rotation, respectively [69], [89]. Points in crystal lattices correspond to glide planes enabling additional lattice rotations which may be different than the material rotation, and differences between material rotation and lattice rotation require plastic deformation [89]. This difference is known as plastic spin which is often required by continuum plasticity in polycrystalline materials to maintain continuity across grain boundaries [90], [91]. Plastic spin is an important consideration for anisotropic materials at high strains, particularly those with HCP structures [89], [91], [92], [93].

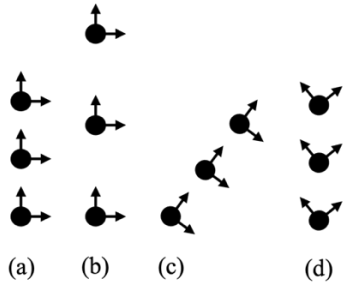

Figure 1-15: Schematic representation of a periodic lattice in (a) an initial configuration, (b) the lattice subjected to strain, (c) the lattice subjected to material rotation, and (d) the lattice subjected to lattice rotation.

Although plasticity is considered a time-independent mechanism, it is slightly sensitive to the deformation rate so care must be taken when selecting experimental loading rates to ensure they are consistent and relevant to the application. However, strain rate sensitivity is mostly relevant at low dislocation densities and very high strain rates ($\dot{\epsilon}$ > 10 %/s) due to mechanisms such as phonon drag that can affect dislocation velocities [94]. Rheological models can incorporate parallel elements according to the Kelvin-Voight model to incorporate this sensitivity, but for

simplicity and especially at elevated temperatures, time dependency is attributed to the viscoplastic deformation mechanisms discussed in the next section.

1.3.2.3 Viscoplastic Response

Viscoplastic deformation occurs when atoms are not displaced enough by the applied load to remove them from their current lattice positions directly, requiring thermal activation for deformation to occur. Distinct from thermally assisted plastic deformation, viscoplastic deformation occurs below the CRSS required for dislocation slip and relies on diffusive effects for deformation to occur which introduces the time-dependent nature of viscoplasticity. This time dependency is represented in the rheological model in Figure 1-13 using a component known as a dashpot[4] that resists high displacement rates but extends at low displacement rates. Viscoplasticity and plasticity both contribute to the defect energy and dissipation terms in Equation 1-2.

Viscoplastic mechanisms and strain rates are sensitive to both stress and temperature and these dependencies are shown using the Ashby deformation mechanism map in Figure 1-16. Although time-dependent diffusive effects are required to activate viscoplastic mechanisms, deformation may occur by dislocation motion or purely diffusive effects. At higher stresses, deformation occurs more quickly through dislocation mechanisms while lower stresses cannot effectively activate dislocation motion and occurs more slowly through diffusive effects.

Common viscoplastic deformation mechanisms are summarized in Table 1-3 from [20], [81], [95], [96], [97], [98]. Multiple mechanisms are usually active under given stress and temperature conditions, but one mechanism generally permits a strain rate much higher than other active mechanisms and is known as the rate-limiting deformation mechanism. The stresses and temperatures relevant to the PCI conditions, including those selected for Chapter 5, are in the viscoplastic regimes of low temperature climb and athermal deformation in Figure 1-16. Therefore, a detailed background is provided for these mechanisms which is omitted for the other viscoplastic deformation mechanisms for brevity.

Table 1-3: Viscoplastic deformation modes and characteristics.

Mode	Rate-Limiting Mechanism	Stress	Temperature	Stress Exponent
Dislocation Glide	Dragging effect of obstacles on dislocation glide.	High	Intermediate	$n > 7$
Dislocation Climb	Dislocation climb around obstacles.	Wide Range	High	$n \approx 5$
Grain Boundary Sliding	Grains sliding through enhanced diffusion at grain boundaries.	Intermediate	Wide Range	$1 < n < 3$
Coble	Grains elongating through enhanced diffusion at grain boundaries.	Low	Wide Range	$n \approx 1$
Nabarro-Herring	Grains elongating through intragranular diffusion.	Low	High	$n \approx 1$

[4] The dashpot is the traditional term for a piston shock dampener.

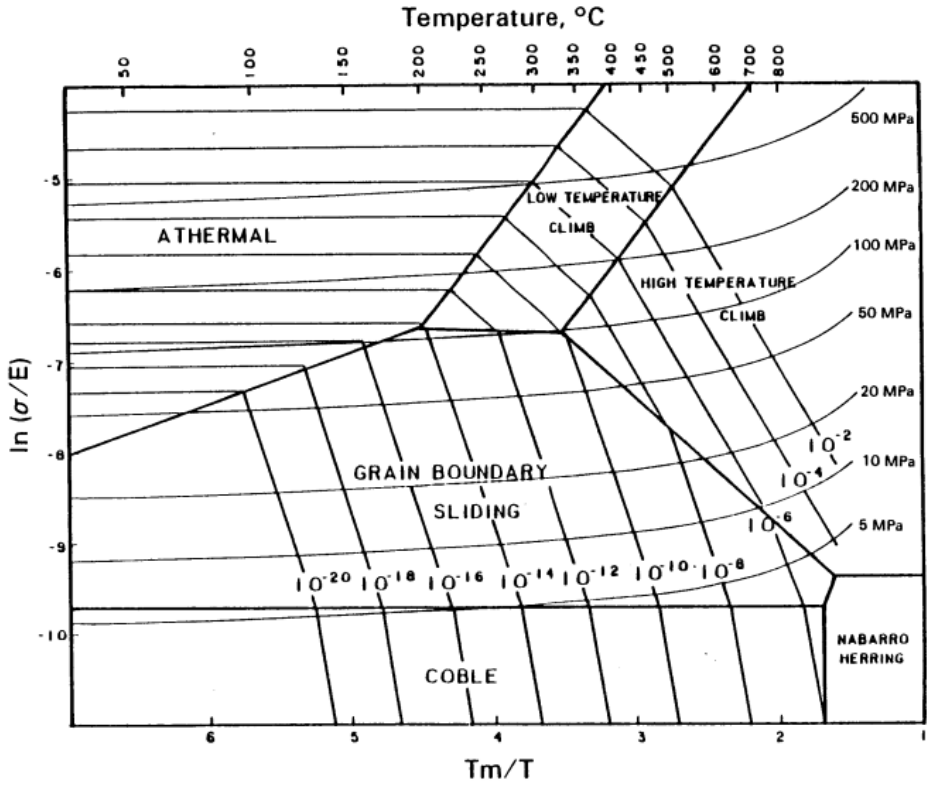

Figure 1-16: Zircaloy deformation mechanism map with constant stress and strain rate contours [95].

Dislocation glide occurs through dislocation movement in the direction of the RSS which is impeded by other defects forming obstacles. Plastic deformation occurs when the RSS is high enough for gliding dislocations to bypass these obstacles or form new dislocations, resulting in low time-dependence. Viscoplastic deformation occurs when mobile dislocations climb around the obstacles or drag them through diffusive mechanisms, resulting in strong time-dependence. High stresses and relatively low temperatures allow mobile dislocations to drag obstacles such as point defects and dislocation jogs faster than climbing around them, resulting in the name dislocation glide or sometimes low-temperature climb. Temperatures high enough for mobile dislocations to climb around the obstacles faster than dragging them is known as dislocation climb. Multiple of these mechanisms can operate simultaneously and the variable spaces shown in Figure 1-16 are attributed to the rate-limiting mechanism.

These deformation mechanisms have different relationships between stress and strain rate, as indicated by the angles between intersecting iso-stress and iso-strain-rate contours in Figure 1-16. This relationship is quantified through the stress exponent (n) in Equation 1-6 which can be used to help identify the rate-limiting viscoplastic deformation mechanism as shown in Table 1-3 [99]. Here, σ is the measured stress, $\dot{\epsilon}_{vp}$ is the measured viscoplastic strain rate, A represents the equivalent global strain rate for unit stress, and σ_1 (1MPa) is the unit stress. Stress exponents near one indicate a proportional relationship between stress and strain rate while high stress exponents indicate high sensitivity.

$$\dot{\epsilon}_{vp} = A\left(\frac{\sigma}{\sigma_1}\right)^n \qquad \text{Equation 1-6}$$

Figure 1-17 shows stress exponent regimes of Zry-4 alloys from literature. At higher temperatures and lower stresses in Figure 1-17 (a), regime I where n = 1 is attributed to Coble deformation, and regime II where n = 3 is attributed to dislocation glide impeded by dispersed solute atoms [20], [99]. These small, dispersed defects produce smaller stress exponents because they are able to diffuse more easily than Cottrell atmospheres and dislocation interactions. Regime III where n = 5 is attributed to dislocation climb which is typically known as power law viscoplastic deformation [80], [97], [98], [100], [101]. At lower temperatures and higher stresses in Figure 1-17 (b), results of the modified jogged-screw dislocation model is shown which extends from the power law regime through the power law breakdown regime at high stresses where n > 7, marked as the athermal region in Figure 1-16 [80], [102], [103]. High stress exponents are indicative of dislocation glide slowed by larger defects such as dislocation jogs and dipoles [97], [102], [103]. Figure 1-16 and Figure 1-17 show how increasing temperature reduce the stress required for mechanism transitions to occur.

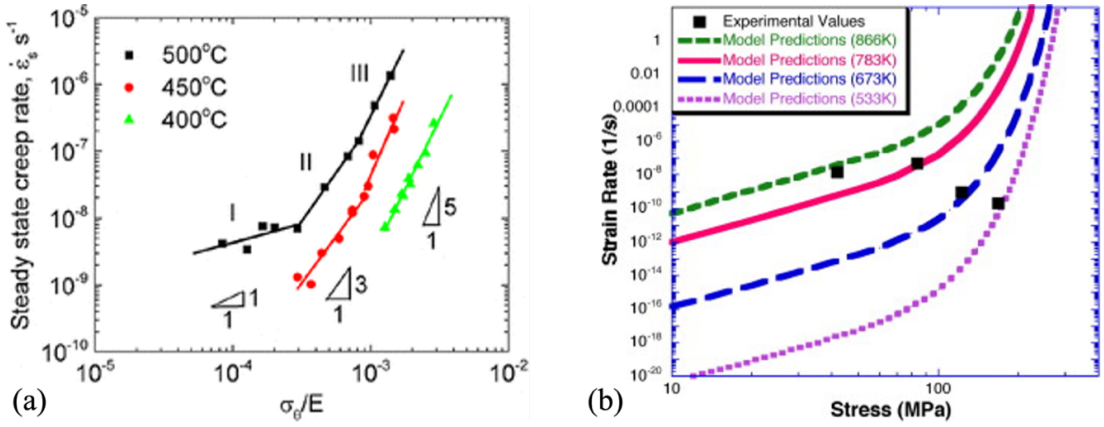

Figure 1-17: (a) Log-log plot of modulus-compensated stress versus viscoplastic strain rate showing results for a Nb-added Zry-4 [20]. (b) Log-log stress-strain rate plot showing modified jogged-screw dislocation model predictions for Zry-4 [102].

Thermodynamic relationships can also be used to help identify active deformation mechanisms are possible such as activation energies and activation volumes [20], [50], [54], [88], [98], [104], [105], [106], [107]. Activation volumes are particularly useful for this dissertation because they may be calculated from stress relaxation tests and provide an estimate of the rate-limiting defect size. For example, diffusion and point-defect interactions have small activation volumes on the order of 1 b^3, where b is the Burgers vector, while dislocation interactions occur with larger activation volumes ranging up to several thousands of b^3 [105], [108], [109]. Decades of research related to deformation mechanisms in crystalline materials and, particularly, zirconium and its alloys have produced an expanse of data related to activation properties which can be used to evaluate rate-limiting deformation mechanisms [50], [51], [98], [104], [105], [107], [108], [109], [110], [111], [112].

Viscoplastic deformation is the material response to an applied load, but as shown using the rheological models in Figure 1-13, the material can respond to imposed force or imposed displacement. Imposed force produces a strain response known as creep while imposed strain produces a stress response known as stress relaxation. Viscoplastic deformation is not apparent while the displacement remains constant, but stress is proportionately related to the elastic strain

and the viscoplastic strain must increase to compensate the decrease in elastic strain according to Equation 1-7.

$$\dot{\epsilon}_{vp} = -\frac{1}{E}\frac{d\sigma}{dt} \quad \text{Equation 1-7}$$

Creep tests generally apply a constant force at a constant temperature which produces a steady-state creep rate for a majority of the test period corresponding to the rate-limiting mechanism. As deformation occurs, defects in the microstructure accumulate at grain boundaries and dislocation structures but are replenished by the consistent work performed on the material, causing this deformation mode to damage the material [113]. In contrast, the constant displacement of a stress relaxation test limits the work performed on the material to the loading period, and the relaxation period allows the material to recover [54], [114], [115], [116]. Additionally, stress inherently is changing during a stress relaxation test so multiple rate-limiting mechanisms can be present in a single stress relaxation test. These are fundamental differences which may complement each other in studying viscoplastic deformation mechanisms but can require extensive discussion to distinguish between them. Further discussion is limited to the primary focus of this dissertation – stress relaxation.

Loading prior to a stress relaxation test is an important parameter that produces distinct behavior when loading above or below yield which can occur within a fraction of a percent strain. Loading above yield results in higher stress and dislocation density which enhances relaxation behavior, particularly because there is a limited amount of work provided to the material [117], [118]. During relaxation, dislocations propagate deformation to homogenize stress fields which dissipates elastic energy, and they can also annihilate or form low energy defects such as dislocation cells which dissipates defect energy [54], [115], [116], [117], [119]. This microstructure recovery improves ductility [115], [118].

Stress relaxation behavior is characterized by a variable-rate relaxation (VRR) period that transitions into a steady-rate relaxation (SRR) period [117]. Rapid deformation mechanisms relying on high stress conditions accelerate deformation during the VRR period, but deactivate at lower stresses, transitioning into some new rate-limiting mechanism during the SRR period [54], [94], [117], [119]. The VRR period is particularly distinct when samples are loaded above yield because mobile dislocations are able to break away from defects and glide which rapidly propagates deformation [54], [120].

Several studies have explored stress relaxation in textured Zircaloys using methods such as uniaxial tension or bent beam techniques, with a notable focus on accelerated creep testing [49], [50], [51], [54], [107], [114], [121], [122], [123], [124], [125]. However, there is no known literature available related to the stress relaxation response of Zircaloy cladding to internal pressure loading. Therefore, it is the goal of this dissertation to investigate the effect of mechanical anisotropy on the stress relaxation behavior in textured Zircaloy cladding using internal pressure to simulate PCI loading conditions.

Chapter 2 Thesis Summary

This chapter presents the thesis of this dissertation with necessary context to provide an independent section. First, the topic is formally defined and the significance for the application is summarized. Second, the principals used to formulate the thesis are described. Next, the hypotheses forming the thesis statement are listed. Finally, the investigation methods used to evaluate the hypotheses are outlined.

2.1 Stress Relaxation in Zircaloy Fuel Cladding

Stress relaxation is a viscoplastic deformation mode where applied displacement loads a material and the resulting stress decreases over time as the microstructure rearranges to dissipate energy. The stress relaxation process involves elastic, plastic, and viscoplastic deformation components. During loading, work is applied which produces elastic strain and stress in the material, here defined as elastic energy. If the material is loaded beyond yield, dislocations form in the material to accommodate the plastic strain, here defined as defect energy. During relaxation, stress decreases as the elastic strain is converted to viscoplastic strain. Dislocations are an important factor because they propagate the viscoplastic deformation that reduces and homogenizes elastic energy as well as storing defect energy which dissipates if they annihilate.

Stress relaxation is relevant to nuclear fuel cladding because operational and accident scenarios can cause the fuel pellet to expand into the cladding, a phenomenon known as a PCI, which imposes a strain for some time. The stress relaxation in cladding materials under PCI conditions is important for several reasons: optimization of power ramping conditioning periods and load following frequencies, accurate quantification of stress accumulation and retention for failure predictions, and better understanding of microstructure recovery mechanisms. Achieving these goals can help improve operational safety and efficiency of reactors. Uniaxial testing is commonly used to characterize mechanical properties, often corresponding to the axial direction for cladding to simplify the testing process. However, reactor conditions such as a PCI creates a multiaxial stress state where the axial and hoop stresses form the principal stress components.

Zircaloy is commonly used for cladding because of its performance in reactor conditions, but Zircaloy claddings display anisotropic mechanical behavior due to HCP structure and strong crystallographic texture. This mechanical anisotropy is sensitive to the applied stress states resulting in significant differences in resulting stresses, strain components, and microstructure between loading modes. This dissertation compares relevant uniaxial and multiaxial stress states to investigate the effect of mechanical anisotropy on stress relaxation mechanisms and response in textured Zry-4 cladding. Uniaxial stress states include tensile axial and hoop stresses corresponding to rolled direction and transverse direction microstructure, respectively. Multiaxial stress states include PCI and capped internal pressure, producing tensile axial to hoop stress ratios of 0.75 and 0.5, respectively.

2.2 Thesis Principles

Zircaloy cladding texture is retained because it orients slip systems with <*c*> components in such a way that resists thinning the cladding thickness [12]. The PCI and internal pressure stress

states develop high radial strain ratios which interact with this mechanism and observe high yield stresses compared to uniaxial stress in the axial or hoop directions as observed by [21]. However, the CRSS ratios affecting this behavior are temperature sensitive and the difference in yield stress is reduced at elevated temperature [58].

There is evidence that intragranular rotation due to plastic slip, known as plastic spin, is minimized in HCP metals when the loading axis is aligned with the symmetric texture fiber [89], [90]. Conversely, the plastic spin is maximized when the loading axis is "most asymmetric" with respect to the symmetric texture fiber [90]. The rolled direction is colinear with the symmetric texture fiber in pilgered texture Zircaloy cladding, and so uniaxial axial tension is the most symmetric loading orientation and other loading modes are less symmetric. The effects of multiaxial loading are unclear but may be less symmetric than other uniaxial loading in directions that are asymmetric. More geometrically necessary dislocations are required to accommodate increased plastic spin and intragranular misorientation.

Wang & Murty [58] present results showing that mechanical anisotropy is temperature dependent for uniaxial loading along the hoop direction but temperature independent along the axial direction. This implies that there is a temperature dependent deformation mechanism for hoop loading which is not present for axial loading, and further, that the deformation mechanism activity is more competitive for the former to allow thermal activation of this mechanism. An analysis is not presented for a biaxial stress state, but internal pressure loading produces high hoop stress compared to axial stress and may behave more similarly to uniaxial hoop loading. Therefore, the internal pressure stress state may have more competitive deformation activity compared to axial loading.

Each paragraph in this section is used to formulate corresponding Hypotheses in the next section. The first implies that there is more stress energy for the internal pressure stress state compared to the uniaxial stress state which could enhance the stress relaxation behavior. The second implies that there is increased defect energy in the microstructure for internal pressure loading which could enhance the strain rates and defect annihilation during relaxation. The third implies that there are more avenues for dislocations to propagate relaxation which could accelerate the relaxation rates. These three mechanisms are hypothesized to affect the relaxation behavior and their effects enhancing the relaxation rates of the internal pressure stress state compared to axial tension is formally posited in a fourth Hypothesis. These are explicitly listed in the following section.

2.3 Hypotheses

Hypothesis 1: Internal pressure loading stores more elastic energy than axial tension loading for the same equivalent strain, especially at low temperatures.

Hypothesis 2: Internal pressure loading develops more defect energy than axial tension loading for the same equivalent strain.

Hypothesis 3: The internal pressure stress state produces more competitive slip system activity than axial tension, especially at elevated temperatures.

Hypothesis 4: Internal pressure loading enhances stress relaxation compared to axial tension.

Thesis Statement: For the same applied equivalent strain, internal pressure loading displays enhanced stress relaxation compared to axial tension loading because there is more elastic energy, defect energy, and competition between active deformation mechanisms.

2.4 Investigation Methods

This dissertation evaluates the Thesis Statement in the context of plasticity to investigate Hypotheses 1-3 and viscoplasticity to test Hypotheses 1-4 and how they contribute to the Thesis Statement. In Chapter 4, the Study of Plastic Deformation, monotonic strain-rate loading is performed using axial tension and internal pressure loading at temperatures from 20-525 ^{o}C to test Hypothesis 1. Microstructure characterization and viscoplastic self-consistent simulations are performed on samples deformed by both stress states at 400 ^{o}C to test Hypothesis 2. Results of mechanical testing and texture characterization are combined with resolved stress analysis to evaluate Hypothesis 3. In Chapter 5, the Study of Viscoplastic Deformation, axial tension and internal pressure stress relaxation tests are performed at 300 ^{o}C to test Hypothesis 4 and determine the effects of Hypotheses 1-3 on the Thesis Statement. Three different equivalent strains vary the initial elastic energy and defect energy to elucidate these effects. Microstructure characterization is performed on samples throughout the loading and relaxation phases of testing to reveal the defect energy evolution for both loading modes to test Hypothesis 2. An activation volume analysis is performed to investigate Hypothesis 3. Experimental results are compared to simulated results of a fuel performance viscoplastic material model to provide context to current approaches.

Chapter 3 Methods

The study of plasticity and the study of viscoplasticity included as Chapter 4 and Chapter 5 in this dissertation use the same materials and methods so are condensed in this chapter to avoid repetition. Chapter 4 and Chapter 5 include brief methods sections providing experimental overviews, noting any variation to the methods described in this chapter, with any methods specific to that chapter. Methods are developed during the study of plasticity and selected methods and optimized parameters are used for the study of viscoplasticity.

3.1 Experimental Methods

Zry-4 cladding samples are mechanically tested using strain-rate controlled axial tension and internal pressurize loading to produce uniaxial and multiaxial tensile stress states for comparison. Samples are deformed at several temperatures anticipated in PWR conditions. Pristine and deformed sample material are characterized using: a synchrotron 3D X-ray microscope (3DXM), X-ray diffraction (XRD), nanoindentation, and SEM-EBSD. Results of nanoindentation and XRD are inconclusive and so the methods and results are not presented for brevity.

3.1.1 Cladding Samples

Typical PWR cladding is used for this dissertation which is CWSR Zry-4 with a nominal outer diameter of 9.5mm and a wall thickness of 0.57mm. The cladding is commercially procured and is nuclear grade, conforming to ASTM B353-12 [126]. The cladding is pilgered during production and all samples used in the dissertation are from the same batch of cladding to ensure consistent initial microstructure (Ingot # 252045, Heat Treat # 291437). Inductively coupled plasma mass spectrometry is used to determine the alloy composition which is listed in Table 3-1. Trace elements are included in the certified test report provided in Chapter 8 Section 2.

Table 3-1: Elemental composition of the current Zry-4 alloy.

	Zr	**Sn**	**Fe**	**Cr**	**O**	**C**	**H**
%	bal.	1.22	0.19	0.11	0.13	0.020	0.0017

Cladding sections are cut into 150 mm lengths, deburred, and swaged into 3/8” SwageLok™ medium pressure tube fittings on both sides to form individual samples as shown in Figure 3-1. The SwageLok™ fittings form the sample fixtures interfacing with the mechanical loading device. The gage section is kept at least 10 mm away from the swages to avoid stress concentration effects.

Figure 3-1: Cladding samples with SwageLok™ fittings.

3.1.2 Mechanical Testing

3.1.2.1 System Description

The loading device used for mechanical testing in this dissertation is a custom system illustrated in Figure 3-2. The loading system incorporates a universal testing machine and a pneumatic system capable of internally pressurizing samples to produce axial tension or internal pressure loads. Extensometers measure the strain which are used in a feedback control system with a venting pressure regulator to achieve pseudo displacement-controlled tests required for constant strain rate and stress relaxation experiments. The extensometers and pressure transducer transmit signals to the data acquisition and controls (DAQC) system. A box furnace with an argon purge encloses the system to achieve elevated temperature while limiting oxidation and providing safety containment. This system is discussed in more detail in the remainder of this section and a photograph of the loading system is included in Figure 3-3.

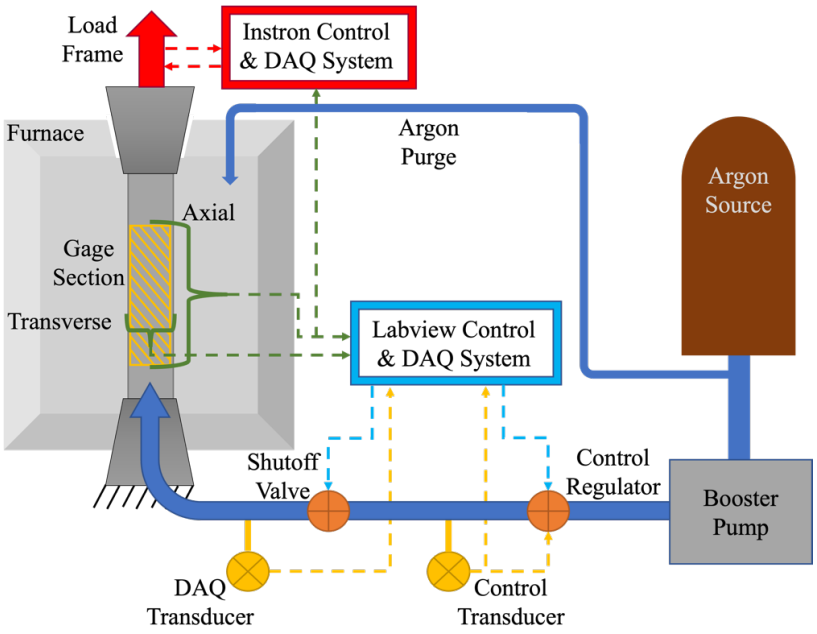

Figure 3-2: Schematic diagram of mechanical testing system.

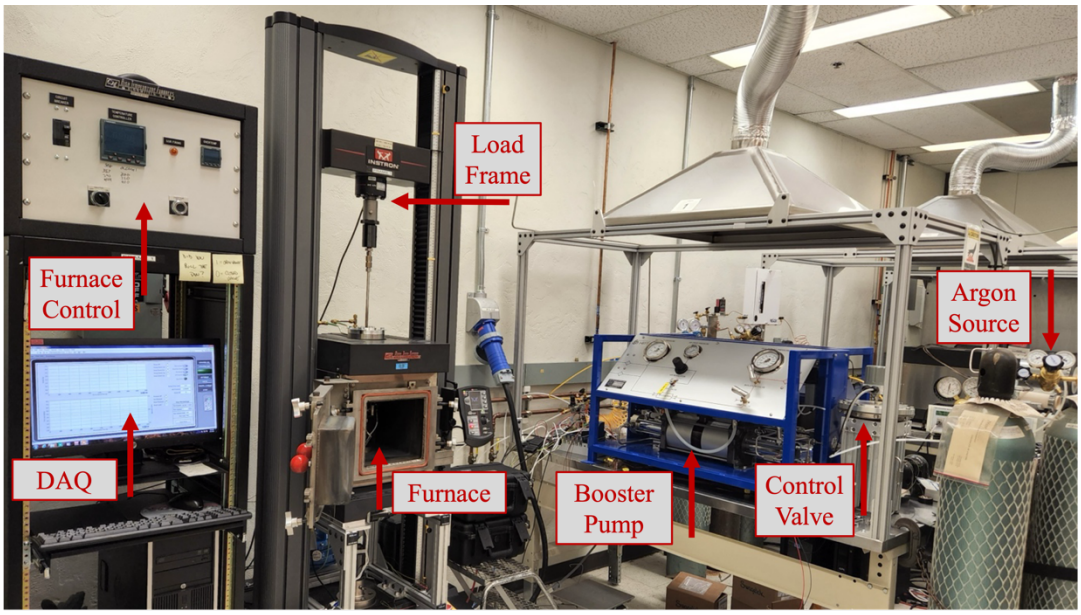

Figure 3-3: Labeled photograph of the experimental testing system.

The sample is connected at the bottom to a fixed bulkhead connection using the SwageLok™ fitting to immobilize the boundary while coupling with the pneumatic system. The top of the sample is connected to a linkage that seals the top of the sample and can connect with the Instron model 5967 universal testing machine. The Instron is colinear with the bulkhead and sample to minimize shear forces. During an axial test, the linkage is attached to the Instron which

transfers the uniaxial load. During a pressure test, the linkage is unattached to the Instron to produce a capped but unconstrained stress state when the sample is pressurized.

A strain history is defined in the control program which uses nested proportional-integral-derivative (PID) feedback loops to adjust the sample load to achieve the desired strain. Epsilon Model 7675-025M and Model 7642-010M-025M high-temperature extensometers are used to measure the axial and transverse (hoop) cladding strain during the tests. The axial extensometer uses a 50 mm gage length, and the transverse extensometer uses the cladding initial outer diameter as the gage length. The PID feedback loop compares the process variable to the set point and adjusts the control variable to reduce the error value. During an axial test, the axial extensometer is the process variable providing feedback to the Instron control system to adjust the control variable, axial load. The extensometer data is used to avoid compliance error from crosshead displacement. During a pressure test, the hoop extensometer is the process variable providing feedback to the pressure control system to adjust the control variable, pressure. A quasistatic strain rate is used load samples at 0.1%/minute (1.67×10^{-5}/s) axial strain for axial tests and hoop strain for pressure tests.

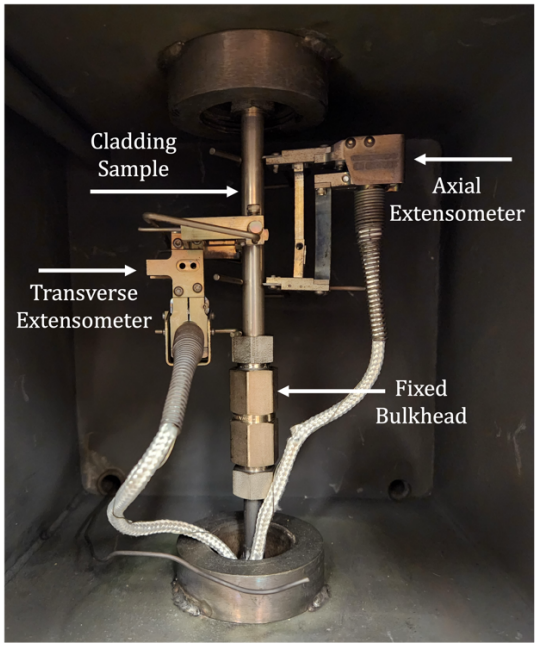

Figure 3-4: Sample in furnace with extensometers attached.

A Maxpro MTIG20-30-75-2 booster pump is used to increase the pressure of an argon gas source up to 135 MPa. A Tescom ER5000 digital controller pneumatically adjusts a Tescom 26-2000 pressure-reducing diaphragm regulator to achieve the desired pressure. The pressure set point is relayed from a Labview control program to the ER5000 controller which uses another PID feedback loop to adjust the control regulator to reduce the error between the measured pressure and pressure setpoint. The sample pressure is increased using the high-pressure source or reduced by venting to atmospheric pressure. A Tescom 2168 pressure transducer is used to provide feedback for the control system and an additional Omega PX01S0 pressure transducer is located close to the sample to obtain the most accurate internal pressure measurement in the sample. A nominally open Remarco D Series solenoid valve programmed to close upon a significant pressure

drop is located between the two pressure transducers to close if the test sample ruptured, limiting the amount of high-pressure compressed gas being expelled through the ruptured test sample.

A box furnace from CM Inc. is used to elevate the test sample temperature to a maximum of 700 ºC. The box furnace also provides safety containment for the pressure tests in case of sample rupture. An argon purge line is regulated by a Alicat Scientific digital flow meter to provide consistent 0.10 standard liters per minute of flow to the furnace to limit sample oxidation during high-temperature testing without causing significant temperature fluctuations. A thermal calibration of the sample temperature profile in the furnace with the Ar purge is used to determine the correct furnace power settings. The thermal calibration and condition are described in Chapter 8 Section 3.

3.1.2.2 Test Procedure

Samples are coupled with the loading system at the bulkhead fitting at the bottom and the deadleg linkage at the top. For axial tests, the linkage is connected to the Instron crosshead. For pressure tests, the linkage remains unconnected and unconstrained, but the Instron crosshead is lowered to prevent excessive displacement if the sample ruptures. The axial and hoop extensometers are attached, and zero strain positions set using calibration pins before sealing the furnace door.

For elevated temperature tests, the Ar purge is turned on at high flow rate for several minutes to evacuate the air in the furnace before returning the flow to 0.1 SLPM and activating the furnace. The furnace brings the temperature up to the set point in ~ 1 hour, but the furnace remains on for 3 hours before testing to ensure isothermal conditions. The normalized thermal heating profile is included in Figure 3-5.

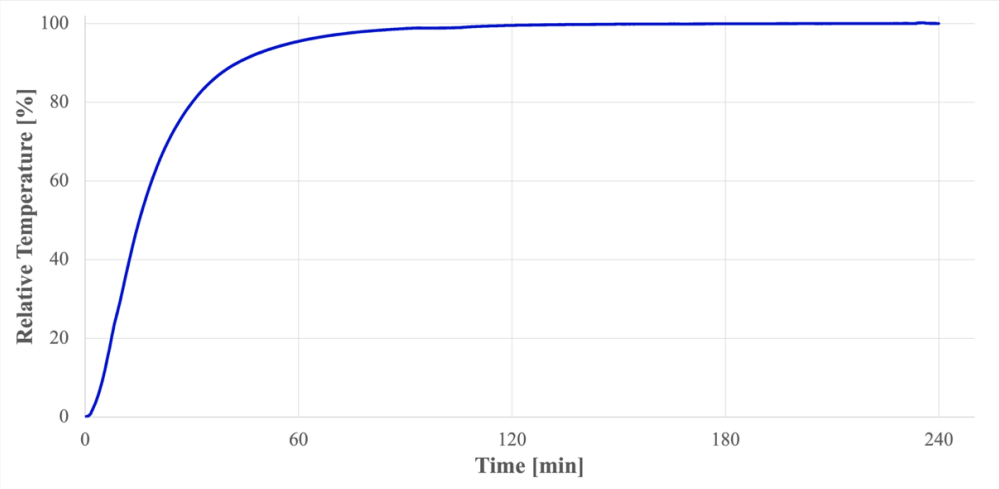

Figure 3-5: Furnace heating profile for a 300 ºC test.

Before testing, the extensometer signals are redefined as zero strain. The axial tests are automated by the Instron universal testing machine and samples. For pressure tests, the booster pump is activated to charge high pressure reservoir to higher pressure than the maximum required for the test. The nested feedback loops and high pressure in the pneumatic system challenge the limits of the controller and actuator and some pressure oscillations can occur. The PID coefficients shown in Table 3-2 are chosen to limit the pressure oscillations to the greatest extent possible.

After unloading, the furnace and argon purge are turned off and the samples are removed from the furnace. Samples tested at 300 ºC for the study of viscoplasticity are cooled using compressed air and immediately removed from the furnace to preserve sample microstructure.

Table 3-2: PID settings for pressure control system.

Test Temperature [ºC]	P	I	D
20	35	0.0067	0
150	35	0.0067	0
275	30	0.0067	0
300	30	0.0067	0
400	30	0.0067	0
525	5	0.0067	0

3.1.3 Metallographic Preparation

The 50mm gage section of the mechanical samples is removed from the mechanical sample using a high-speed saw at 2500rpm with a SiC blade and water to cool and lubricate the cut. The feed rate varies between 0.05-0.15 in/min depending on the sensitivity of the cut and fixturing. The cladding gage section is further sub-sectioned into rings which are then cut axially to produce sample chips as shown in Figure 3-6. All samples are cut and polished to expose the axial-hoop plane with a plane normal vector colinear with the cladding radial axis.

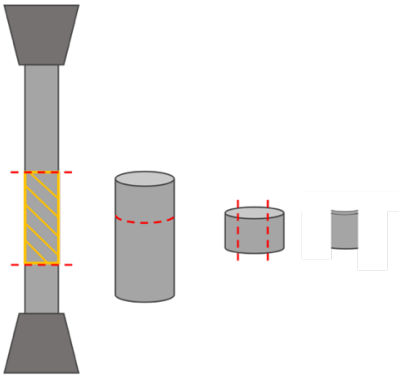

Figure 3-6: Sample subsectioning process for sample characterization.

Samples are mounted to an Al puck using Crystalbond 509. The Al puck is heated until the Crystalbond becomes a viscous liquid, then sample chips are pressed into the glue and level against the puck. Sample heating is minimized to preserve deformation microstructure and the maximum temperature for an average mounting measured using an infrared thermometer was 85 ºC. A conductive carbon sticker is used to achieve high emissivity.

Mounted samples are hand ground with low grit SiC paper and water to remove excessive Crystalbond and deburr samples. Next, the samples are grinded to a flat surface in a Bueler Automet grinding jig shown in Figure 3-7 with gears producing contrary rotations from the wheel direction. The low wheel speed is used with water lubricant and 600 grit then 800 grit SiC grinding paper from Allied High Tech Inc. Samples are rinsed or sonicated to remove abrasive contaminates

between stages. The soft Zry-4 frequently galls with higher grit grinding paper and traditional polishing suspensions, producing defects much larger than the abrasive media and sometimes displaying rolling features as shown Figure 3-8.

Figure 3-7: Grinding samples on SiC paper with water lubricant.

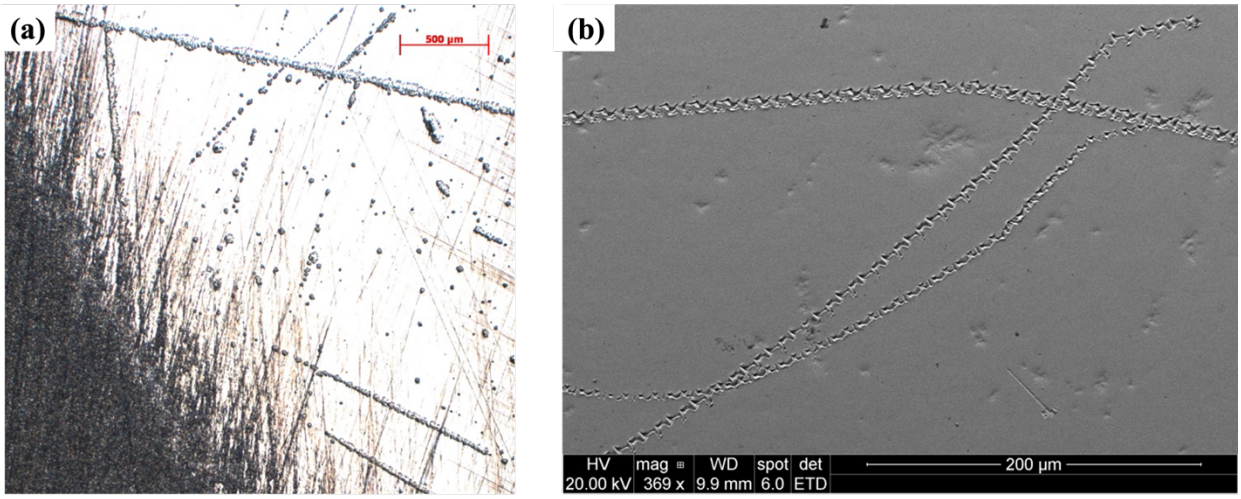

Figure 3-8: (a) Optical photograph of sample after partial polishing with 9 µm SiC suspension with residual 800 grit ground area in the bottom left. (b) Secondary electron micrograph of sample surface after polishing with 3µm SiC suspension.

Diamond lapping films with 3 µm and then 1 µm roughness from Allied High Tech Inc. are used to prevent galling while remove the deformation layer from grinding. Contrarotation with

150 wheel-rpm and 100 sample-rpm is used for 10 minutes with water lubricant and 10 N per sample. A sample was microindented with a Vicker's tip to quantify lapping removal rates using the geometry and measured dimensions of the indent. Under these conditions, the 3 μm lapping film removed 30 μm and the 1 μm film removed 15 μm of Zry-4 in 10 minutes.

Chemo-mechanical polishing is performed using Bueler Mastermet2 which is a 0.02 μm colloidal diamond solution with a ph of 10; additionally, some hydrogen peroxide is added to the polishing cloth to improve polishing quality. Samples are polished for 30 minutes with 10 N of force and complementary rotations (150 wheel-rpm and 100 sample-rpm) on a Final A polishing pad from Allied High Tech. The resulting surface presented in Figure 3-9 displays little topology, and electron channeling provides backscatter contrast indicating low surface deformation. Samples are removed from the Al puck by sonicating in acetone and then alternately rinsing with acetone and ethanol to dissolve then flush remaining Crystalbond.

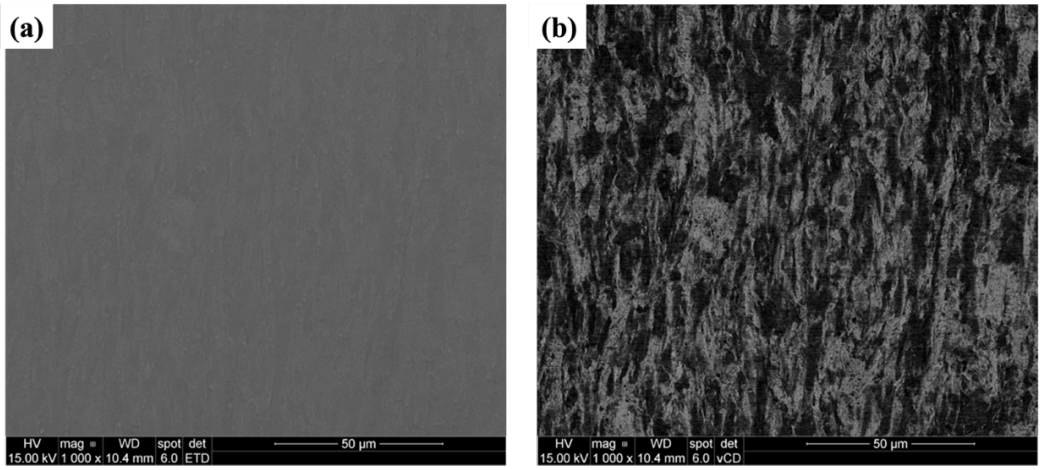

Figure 3-9: SEM micrograph of polished sample surface at 1000x magnification. (a) Secondary electron detector and (b) backscatter electron detector.

SEM-EBSD samples have residual strains from polishing removed using cryo-EP to improve electron diffraction indexing. Cryo-EP is conducted for 1 min using the following conditions: solution (93 vol% ethanol, 7 vol% perchloric acid), and electropolishing parameters (0°C, 95mA, 25V). Samples are mounted to 10 mm SEM stubs using conductive carbon tape and silver paint to improve the conductivity and prevent charging.

3.1.4 Synchrotron 3D X-ray Microscope

The 3D X-ray Microscope (3DXM) used for this work is located at Argonne National Laboratory (ANL) in the Advanced Photon Source (APS) synchrotron, beamline 34-ID-E. The 3DXM performs Laue micro-diffraction using a focused beamline with a differential aperture and area detectors to illuminate sub-micron volumes called voxels. The sample surface is oriented at 45^{o} to the incident beam path which penetrates and diffracts from the material producing Laue diffraction peaks from the entire illuminated depth on the charge-coupled device area detectors. A highly absorbing platinum wire acts as the differential aperture by scanning 100 µm above the surface providing interference between the diffracting X-ray peaks and the area detectors. The diffraction peak interference at different aperture positions is used to determine the depth that each

diffraction peak originates from. Then the Laue diffraction patterns corresponding to each voxel are used to determine the localized orientation, microstrains, and other properties. This process is repeated to create 2D or 3D characterized volumes by moving the sample in X and H (colinear and normal to wire axis). A schematic of this process is included in Figure 3-10 and a labeled photograph of the beamline is included in Figure 3-11 (a). A more detailed description of the APS 34-ID-E and its capabilities is available on the beamline website [127] and in [128], [129].

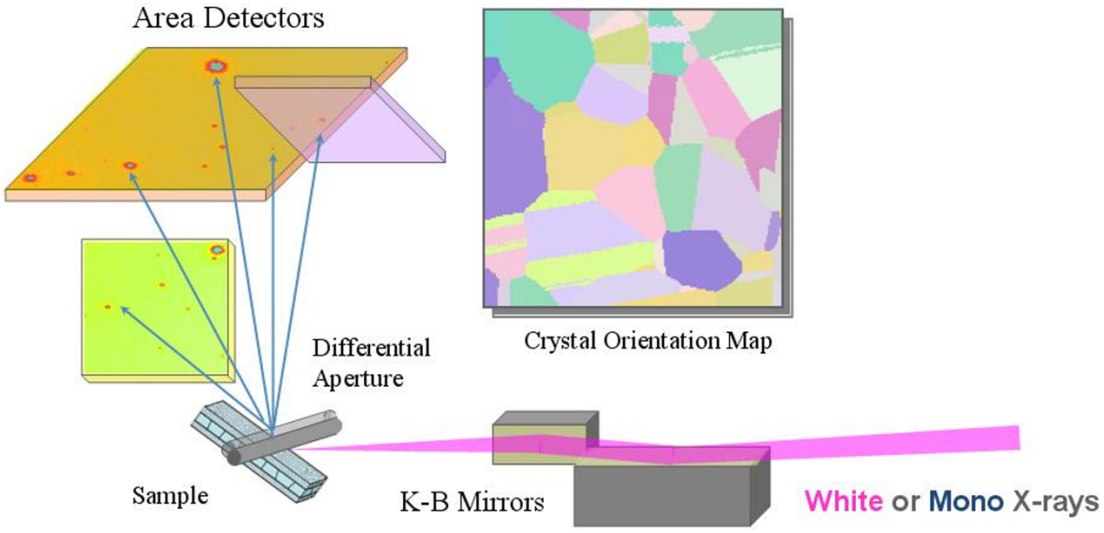

Figure 3-10: Schematic showing function of APS Beamline 34-ID-E 3DXM [127].

This study primarily employs the polychromatic x-ray beam with energies in the range of 7-30 keV which is focused using a pair of Kirkpatrick-Baez (KB) mirrors to a spot of approximately 300 × 300 nm^2 with a flux of about 10^{11} photons/s. Laue diffraction patterns are collected by the pixel-array Perkin-Elmer detector (2048 × 2048 pixel grid, 200 x 200 μm^2 pixel size) positioned about 500 mm above the sample centered at a scattering angle of 90°. The geometry of the detector and wire are calibrated using a strain-free 5 µm thick silicon wafer [130]. The Zry-4 sample is mounted in a 45° reflection geometry as shown in Figure 3-11 (b), so the cladding RD (axial), TD (hoop), and ND (radial) axes correspond with the H, X, and F axes, respectively. Sample structure is imaged in the X-Z plane with 0.5 µm resolution by analyzing Laue diffraction patterns collected with exposure time of one and two seconds for pristine and deformed Zry-4 samples, respectively, in a 2D type scan. At each X-sample position a differential aperture scan is performed by moving wire along the H direction across the diffracted X-rays to resolve diffracted signals from sample along the Z. For each surface location, 1101 patterns are acquired at 1100 aperture positions to decompose all the diffraction peaks for the diffracting depth.

Depth resolved Laue pattern reconstructions and Laue diffraction peak indexing are performed using the high-performance computing cluster at ANL. For the indexing of Laue patterns lattice parameters, *a* and *c*, are measured in the pristine sample using monochromatic energy scans across relevant spectra to determine the photon energy with the strongest diffraction conditions. Three different systems, $(\bar{1}2.4)$, $(\bar{2}3.5)$, and $(\bar{3}3.8)$, are scanned in this manner to measure lattice parameters. Local deviatoric lattice strain is calculated and visualized using Igor Pro 9 and MATLAB R2020b. Due to beamline availability, only the pristine and biaxial-deformed samples are characterized using 3DXM.

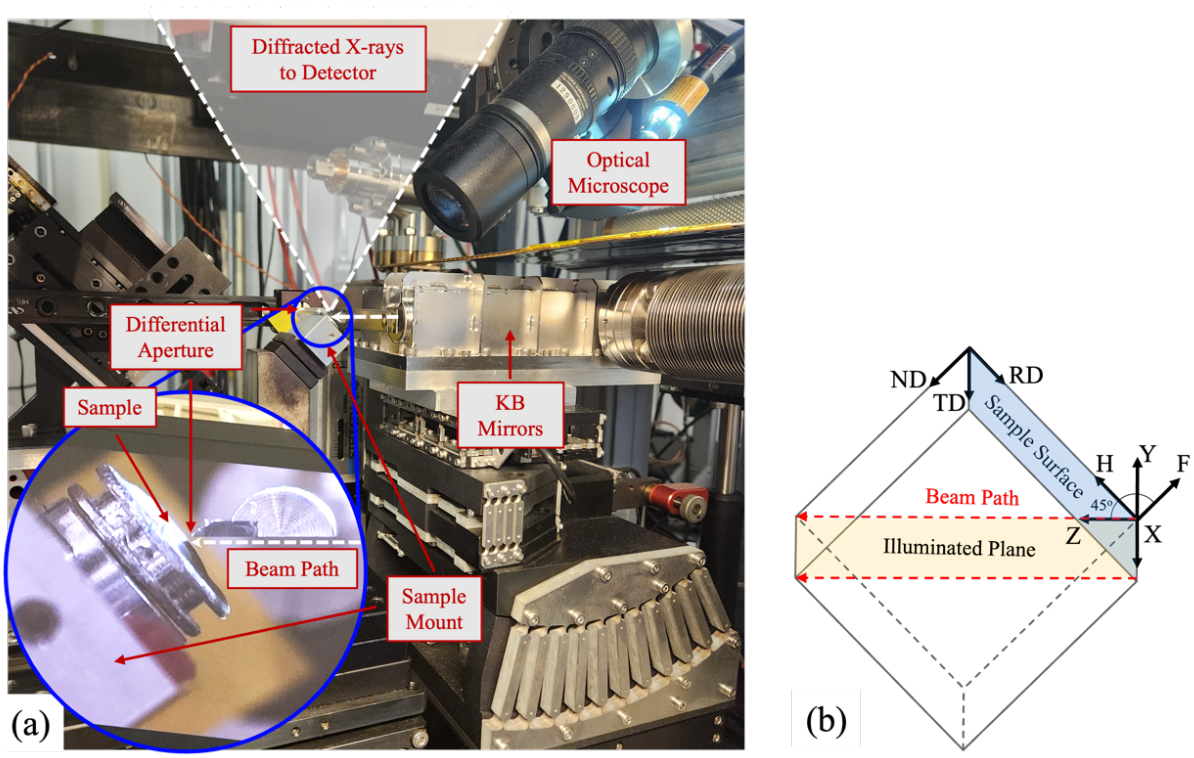

Figure 3-11: (a) Schematic of the sample coordinate system (X, H, F) and the beamline coordinate system (X, Y, Z). (b) Photograph of the APS beamline 34-ID-E with an inlay showing the sample target and differential aperture.

Lattice parameters, *a* and *c*, are essential to relate Laue diffraction patterns to crystallographic properties. Measurements from XRD characterization are used initially, but then measured with higher resolution using monochromatic energy scans with the beamline. After measuring Laue patterns with a whitebeam, a monochromatic beam with increasing energy is used to determine the photon energy with the strongest diffraction conditions. Three different systems, the $(\bar{1}24)$, $(\bar{2}35)$, and $(\bar{3}38)$, are scanned in this manner to measure lattice parameters.

3.1.5 Electron Back Scatter Diffraction

EBSD characterization is performed using the ThermoFisher Scientific Scios 2 DualBeam scanning electron microscope coupled with the Symmetry S3 EBSD detector (Oxford Inc.). The EBSD acquisitions are performed with the sample surface highlighted in Figure 3-11 (b) at 70° tilt to the beam axis, using a 6.4 nA current at an accelerating voltage of 20 kV at a working distance of 15mm. Four magnifications are used to investigate different length-scales with parameters included in Table 3-3. Grid size varies slightly at 7500x (345 ± 26) because some electron charging occurs towards the end of the acquisition, and the affected data is deleted.

Table 3-3: ESBD characterization parameters

Magnification	Step Size [nm]	Grid Size	Area [μm^2]
600x	750	461 x 317	82,200
2500x	250	200 x 140	3,500
4000x	150	346 x 237	1,850
7500x	50	553 x 345	484

3.2 Data Analysis Methods

3.2.1 Mechanical Testing

The data acquisition system records load, axial and hoop strain, and elapsed time at 1 Hz and 10 Hz for pressure and axial testing, respectively. The resulting data files are iteratively processed using three python scripts using the structure shown in Figure 3-12. The data processing user interface (UI) file calls functions from the data processing script to calculate and record stresses, true strains, and material properties, and visualize results for the sample. Then, the data processing UI file calls functions from the data visualization file to read, visualize, and record data from multiple samples on the same figures. The following section provides a summary of the calculations performed in the data processing function which is available upon request.

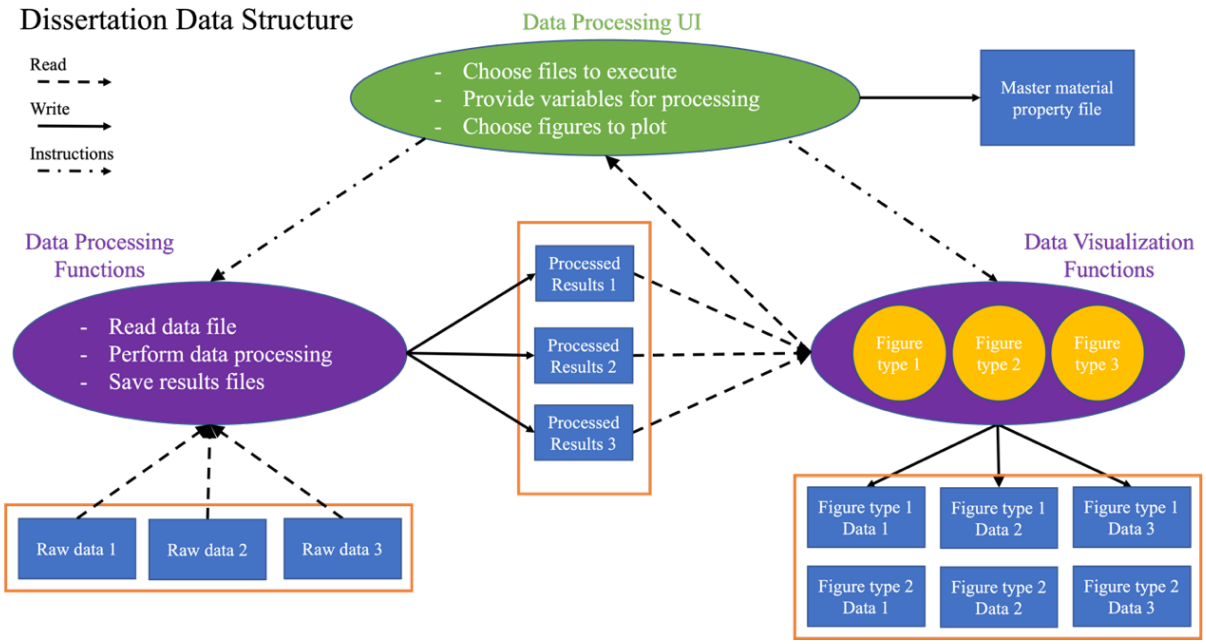

Figure 3-12: Mechanical testing data processing structure.

The data processing function receives the sample number, identification, index, and testing temperature from the UI script. The first module of the function uses the sample identification to import the correct data file and defines the initial dimensions of the sample gage section. The

second module of the function contains all equations used to facilitate verification which are listed as defined in the python script in Chapter 8 Section 4 for verification. The third module of the function uses the engineering stresses and strains to calculate isotropic elastic constants using least square linear regression error minimization to find stiffness constants; low strain minimizes the error of engineering values. The fourth module of the function calculates the total true (logarithmic) strains according to cylindrical coordinate equations provided in [69]. The elastic constants and load values are used to calculate elastic strains and decompose the measured total strains into elastic and plastic components. It further uses the incompressible plastic flow condition to calculate the radial plastic strain and then calculate true stresses. The fifth module of the function calculates true effective stresses and equivalent strains which are used to calculate the yield stress using least square linear regression error minimization and a 0.02% yield offset. Although 0.2% yield offsets are more commonly used, internal pressure loading caused significant plastic deformation to occur within that offset and 0.02% provides better sensitivity to plasticity. The final module saves the processed data to a new file.

For the axial tension stress state, the axial (σ_z), hoop (σ_θ), and radial (σ_r) stresses are defined according to Equation 1-2 where L is axial load, r_o is cladding outer radius, and r_i is cladding inner radius. For the multiaxial-pressure stress state, the stresses are calculated using thin wall stress assumptions which are defined according Equation 3-2 where p_i is the inner gage pressure and δ is the cladding thickness. The thin wall stress assumption for PWR cladding is discussed in x and is validated using FEM analysis by [19]. The engineering stresses may be calculated using initial cladding dimensions or the true stresses using the true cladding dimensions at a time of interest.

$$\sigma_z = \frac{\mathrm{L}}{\pi(r_o^2 - r_i^2)} \qquad \sigma_\theta = 0 \qquad \sigma_r = 0 \qquad \text{Equation 3-1}$$

$$\sigma_z = \frac{p_i r_i}{2\delta} \qquad \sigma_\theta = 2\sigma_z \qquad \sigma_r = 0 \qquad \text{Equation 3-2}$$

Isotropic elasticity behavior is assumed for the cladding which use the Young's modulus (E) and Poisson's ratio (ν) to relate the measured engineering strain (ε) to the engineering stress (s) according Equation 3-3; the tensor is simplified to two dimensions because only two equations are required and no radial strain is measured. The resulting elastic constant equations for the axial stress state is provided in Equation 3-4. The internal pressure stress state uses the axial-hoop stress ratio in Equation 3-2 and stiffness constants (C) in Equation 3-5 to define the elastic constants according to Equation 3-6.

$$\begin{bmatrix}\varepsilon_z \\ \varepsilon_\theta\end{bmatrix} = \frac{1}{\mathrm{E}}\begin{bmatrix}1 & -\nu \\ -\nu & 1\end{bmatrix}\begin{bmatrix}s_z \\ s_\theta\end{bmatrix} \qquad \text{Equation 3-3}$$

$$\mathrm{E} = \frac{s_z}{\varepsilon_z} \qquad \nu = -\frac{\varepsilon_\theta}{\varepsilon_z} \qquad \text{Equation 3-4}$$

$$C_{zz} = \frac{s_z}{\varepsilon_z} \qquad C_{\theta\theta} = \frac{s_\theta}{\varepsilon_\theta} \qquad \text{Equation 3-5}$$

$$\nu = \frac{C_{\theta\theta} - C_{zz}}{0.5C_{\theta\theta} - 2C_{zz}} \qquad \mathrm{E} = C_{\theta\theta} - \frac{\nu C_{\theta\theta}}{2} \qquad \text{Equation 3-6}$$

All elastic strains may be calculated using elastic constants and true stresses according to Equation 3-7 and the axial and hoop plastic strains are calculated by subtracting the elastic strains from the true (logarithmic) measured strains. However, the plastic radial strain is unknown, and the incompressible plastic flow condition is used to determine this value according to Equation 3-8. This formulation uses the outer radius (r), cladding thickness (δ), and axial gage length (z) with initial positions designated by the $_{(0)}$ subscript and positions at any time step designated by the $_{(t)}$ subscript. The positions at any time are calculated from the true strains, using the true radial strain from the previous time step and accounting for volume change effects due to elastic deformation.

$$\epsilon_z^e = \frac{\sigma_z - \nu\sigma_\theta - \nu\sigma_r}{E}$$
$$\epsilon_\theta^e = \frac{\sigma_\theta - \nu\sigma_z - \nu\sigma_r}{E} \qquad \text{Equation 3-7}$$
$$\epsilon_r^e = \frac{\sigma_r - \nu\sigma_z - \nu\sigma_\theta}{E}$$

$$\epsilon_{r(t)} = \ln\left(\frac{r_{(t)} - \sqrt{{r_{(t)}}^2 - \frac{\left(r_{(0)}^2 - \left(r_{(0)} - \delta_{(0)}\right)^2\right) z_{(0)}}{z_{(t)}}}}{\delta_{(0)}}\right) \qquad \text{Equation 3-8}$$

The von Mises effective stress is used to compare uniaxial and multiaxial stress magnitudes by representing the maximum distortion energy resulting from the stress fields which is simplified to neglect applied shear strains according to Equation 3-9. The equivalent strain in Equation 3-10 provides a comparable strain magnitude for uniaxial and multiaxial strains which relates to the von Mises effective stress using the stress-power balance [131]. Work hardening rates are calculated by taking the derivative of the effective stress with respect to the equivalent strain according to Equation 3-11.

$$\sigma_{eff} = \sqrt{\frac{(\sigma_z - \sigma_\theta)^2 + (\sigma_\theta - \sigma_r)^2 + (\sigma_r - \sigma_z)^2}{2}} \qquad \text{Equation 3-9}$$

$$\epsilon_{eq}^p = \sqrt{\frac{2}{9}\left(\left(\epsilon_z^p - \epsilon_\theta^p\right)^2 + \left(\epsilon_\theta^p - \epsilon_r^p\right)^2 + \left(\epsilon_r^p - \epsilon_z^p\right)^2\right)} \qquad \text{Equation 3-10}$$

$$H = \frac{d\sigma}{d\epsilon} \qquad \text{Equation 3-11}$$

3.2.2 Synchrotron 3D X-ray Microscope

Thousands Laue diffraction patterns are generated for each line scan and most of the reconstruction process is automated and processed using the high-performance computing (HPC)

center at ANL After the reconstruction, orientations and microstrains are calculated and visualized using Igor Pro 9 and MATLAB R2020a.

3.2.3 Electron Back Scatter Diffraction

EBSD data are post-processed and visualized using the software package ATEX by [132], v. 4.14. Texture is calculated with monoclinic symmetry in the RD, using pole figures to visualize the macro-texture of the 600x magnification data and IPF to visualize the micro-texture of the 2500x data from the second round of characterization. IPF micrographs provide the local orientations of the microstructure.

Grain boundaries are defined where misorientation from the nearest neighbors exceeds 10° and grains are defined where grain boundaries form a closed area. The grain size, d, is defined according to Equation 3-12 where S is the surface area of the grain. The grain number and grain area fraction integrals are used to quantify the grain size distribution. The grain morphology is quantified using an ellipsis fitting function within ATEX to find the best fit length and width of that must pass through the grain center of gravity. The aspect ratio defined as the length (long axis) over the width (short axis) and the elongation angle is defined as the angle of the grain length with respect to the RD.

$$\mathrm{d} = 2 \cdot \sqrt{\frac{\mathrm{S}}{\pi}} \qquad \text{Equation 3-12}$$

The kernel averaged misorientation (KAM) quantifies local lattice misorientation using the average misorientation angles of nearest neighboring pixels that form a kernel as shown in Equation 3-13 and Figure 3-13. N is the set of all nearest neighbors within order q, ω is the disorientation angle, o is the orientation of a pixel, (i, j) corresponds to the coordinates of the pixel of interest, and (k, l) corresponds to the coordinates of neighboring pixels. A kernel order size of three is used for all magnification step sizes except 7500x which uses five. Hexagonal pixel formatting is used in this analysis.

$$\mathrm{KAM_{ij}} = \frac{1}{|N(i,j)|} \sum_{(k,l)\in(i,j)} \omega\left(o_{i,j}, o_{k,l}\right) \qquad \text{Equation 3-13}$$

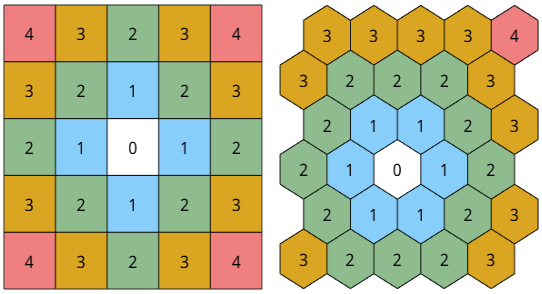

Figure 3-13: Schematic visualization of pixels forming a kernel of nearest neighbors used by KAM analysis. The pixel of interest is denoted by 0 and the nearest neighbors are denoted by their order number (q).

The microstructure is sorted into RX and CW categories based on the KAM within the grain. Grains with maximum KAM under 5° and average KAM under 2° are classified as RX while grains failing to meet either criterion are classified as CW. For more sensitive analysis, the band

slope (BS) is used with KAM to highlight grains exhibiting RX properties because BS provides better contrast for index quality than band contrast [133]. This sorts the micrograph data into two subsets which are used to determine the properties of RX and CW microstructure.

The ATEX software package provides a function to identify twin defects based on the known misorientation angle of the twin boundary. The function uses the twin boundary angles and twin plane Miller indices to identify matches within the EBSD data. The twin systems and angles discussed in Chapter 1 Section 3.1.2. are used to search for twins in the microstructure ± 2°. The ATEX software package also provides a function to calculate the Schmid factor of various slip systems within the material. The Euler angles defining the orientation of each pixel form a rotation matrix (g) to determine the correct orientation of the slip glide plane normal vector (n) and slip direction vector (b). These are compounded with a user defined stress tensor to calculate the Schmid factor.

Chapter 4 Study of Plastic Deformation

4.1 Introduction

The study of plastic deformation provides an opportunity to characterize the mechanical properties and microstructure of the CWSR Zry-4 cladding and refine methods in a relatively simple deformation system. Data related to plastic deformation in Zry-4 cladding is widely available in literature because of decades of research providing references to validate experimental methods and results. The numerous published analyses provide clues to reveal active deformation mechanisms in the temperature range and stress states of interest. This study of plasticity across a range of temperatures is a first step to better understand the material, active deformation mechanisms, and experimental techniques selected for the dissertation.

Samples are tested at a range of ambient to elevated temperatures to measure thermal dependence of mechanical properties. Axial tension and internal pressure testing provide two stress states to investigate mechanical anisotropy and its effect on deformation microstructure. Mechanical testing employs pseudo strain-rate controlled experiments to measure the elastic and plastic deformation behavior of the cladding. Pristine and deformed samples are selected for microstructure characterization and results of successful methods including SEM-EBSD and 3DXM are presented. Necessary experimental and data analysis methods are described in Chapter 3. Viscoplastic self-consistent simulations are performed to investigate effect of differing RD, TD, and ND strain ratios from the applied loading modes.

First the effective mechanical behavior of the cladding is measured for literature comparison as validation, and to measure stress accumulation to test Hypothesis 1. Second, microstructure characterization and viscoplastic self-consistent simulations of pristine and deformed samples is performed to reveal prototypic microstructure and whether internal pressure loading produces more defect energy than axial tension to test Hypothesis 2. Third, an RSS analysis is performed and evaluated with the measured cladding texture to investigate the relationship between stress state, temperature, and slip system activity to better understand the deformation mechanisms and evaluate Hypothesis 3. These topics help define the variables contributing to the enhanced stress relaxation from internal pressure loading that is hypothesized in the Thesis Statement.

This chapter contains work from the following articles:

- *'Multiaxial Plastic Deformation of Zircaloy-4 Nuclear Fuel Cladding Tubes'* [18]
- '*Temperature-Dependent Mechanical Anisotropy in Textured Zircaloy Cladding'* [134]
- *'Deformation Microstructure in Stress Relieved Zircaloy-4 Cladding'* [135]

4.2 Methods

4.2.1 Experimental

Five full-tube axial tension tests and thirteen internal pressure tests are conducted according to the procedures described in Chapter 3 Section 1.2. Of the five axial tests, three tests are conducted at room temperature and two at 400 °C. Of the thirteen pressure tests, four tests are conducted at room temperature, two at 150 °C, three at 275 °C, three at 400 °C, and one at 525 °C. The samples are loaded using a monotonic strain rate of 0.1 %/min to achieve the highest strain possible to measure the ultimate tensile stress without damaging the extensometers as part of [18] Sample names and testing parameters are included in Table 4-1.

Microstructure characterization is performed on samples deformed by axial and pressure loading at room and elevated temperature samples but is dependent on sample and resource availability at the time the characterization is performed. Samples with axial tension and internal pressure loading at room temperature and 400 °C provide four samples in a two-variable test matrix with a fifth, pristine, reference (pristine) sample for initial characterization. Deformation *via* internal pressure at 400 °C is considered the most prototypic conditions so the REF and biaxial-deformed samples are characterized in most detail. Characterization methods for each sample are included in Table 4-1 and all characterization is performed according to the procedures described in Chapter 3 Sections 1.3-5 and 2.2-3.

Table 4-1: Experimental parameters for all samples loaded in the study of plasticity

Sample ID	Loading Mode	Temperature [^{o}C]	Characterization Methods
REF	None	20	SEM-EBSD, 3DXM
AX-RT-1	Axial	20	SEM-EBSD
AX-RT-2	Axial	20	n/a
AX-RT-3	Axial	20	n/a
AX-400-1	Axial	400	SEM-EBSD
AX-400-2	Axial	400	n/a
PR-RT-1	Pressure	20	SEM-EBSD
PR-RT-2	Pressure	20	n/a
PR-RT-3	Pressure	20	n/a
PR-RT-4	Pressure	20	n/a
PR-150-1	Pressure	150	n/a
PR-150-2	Pressure	150	n/a
PR-275-1	Pressure	275	n/a
PR-275-2	Pressure	275	n/a
PR-275-3	Pressure	275	n/a
PR-400-1	Pressure	400	SEM-EBSD, 3DXM
PR-400-2	Pressure	400	n/a
PR-400-3	Pressure	400	n/a
PR-525-1	Pressure	525	n/a

4.2.2 Viscoplastic Self-Consistent Simulations

The texture and grain morphology of the pristine cladding from EBSD datasets at all magnifications are used to perform viscoplastic self-consistent (VPSC) simulations using the software ATEX by [132], v. 14. The pristine microstructure is used to provide identical initial conditions and the strain rates of characterized samples (AX-400-1 and PR-400-1 included in Table 4-3) are used to define the macroscopic velocity gradient tensor for 5% strain. The slip system families discussed in Section 4.2.3 and Chapter 1 Section 3.2.2 are simulated using relative strengths of each slip system calculated at 400 °C with the prismatic, basal, and pyramidal systems achieving relative strengths of 1, 3.2, and 7.7, respectively.

In addition to modeling the internal pressure and RD tension velocity tensors, a TD tension velocity tensor is simulated using the AX-400-1 velocity tensor with the RD and TD rates switched. These strain rates may not perfectly represent experimental strain rates of uniaxial tension in the TD, but Wang & Murty [58] show that Zry-4 anisotropy constants are similar at 400 °C indicating that this assumption is applicable. The uniaxial-TD simulation is performed to investigate differences between uniaxial and multiaxial loading versus uniaxial loading-texture orientation. All simulation variables other than the macroscopic velocity gradient tensor are identical for each simulation.

4.2.3 Resolved Stress Analysis

The resolved stresses in the microstructure are calculated using the applied stress tensor, the desired slip system, and the orientation of the HCP crystal lattice. In this analysis, the biaxial stress state is defined as the axial stress over the hoop stress with all other applied stresses assumed to be zero. The axial tension and internal pressure stress states employed for experimental work are listed in Table 4-2 along with hoop tension and PCI stress states for additional analysis. The glide plane unit normal vector (GPUN) and slip direction unit normal vector (SDUN) of the following slip systems discussed in Chapter 1 Section 3.2.2 are computed across all crystallographic orientations:

- Basal <*a*> (00.2) $\langle 1\bar{2}.0 \rangle$
- Prismatic type 1 <*a*> {10.0} $\langle 1\bar{2}.0 \rangle$
- Pyramidal type 1 <*c*+*a*> {10.1} $\langle 11.3 \rangle$

Table 4-2: Evaluated stress states.

Stress State:	σ_{axial} / σ_{hoop}
Axial	∞
Hoop	0
Pressure	0.5
PCI	0.75

To determine the slip system vectors for each crystallographic orientation, an HCP unit cell is initially defined in the stress state coordinate system and then rotated to the proper orientation. The HPC unit cell is initially defined with the basal (00.1) GPUN and *c*-pole colinear with the radial axis and prismatic (10.0) GPUN normal to the axial axis as shown in Figure 4-1. Using the

[z, θ, r] vector order results in the basal GPUN [0, 0, 1] and prismatic GPUN [1, 0, 0] with the <*a*> SDUN [0, 1, 0] for both systems. Pyramidal systems are at some angle between basal and prismatic planes and can be found using the HCP lattice parameters, *a* and *c*. Pyramidal slip has two <*c*+*a*> slip directions defined as [*a, c*, 0] and [*a**cos(π/6), *a**sin(π/6), *c*]. The pyramidal <*a*> slip direction is defined as [*a**cos(π/6), -*a**sin(π/6), 0]. These slip directions are normalized to unit vectors by dividing each component by the vector magnitude. The pyramidal GPUN is defined using the cross product of <*c*+*a*> and <*a*> or both <*c*+*a*> SDUNs to find the vector orthogonal to two slip directions on the glide plane.

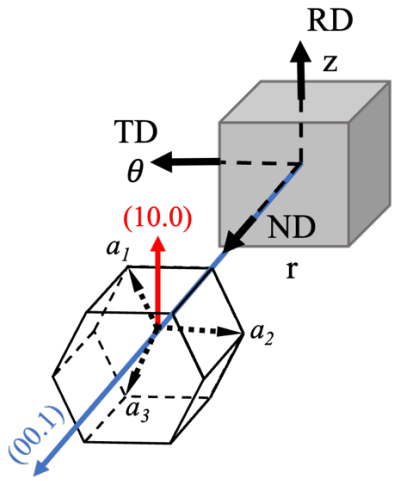

Figure 4-1: Schematic representation of the HCP crystal unit cell initial orientation with respect to principal axes of the sample coordinate system.

The initial unit cell orientation is redefined to the desired orientation using intrinsic chained rotations in the Tait-Bryan order. Chained rotation operations can be intrinsic where each coordinate is dependent on the previous or extrinsic being measured from an absolute coordinate system. Intrinsic rotations redefine axes between rotations which employ prime notation for axes that are the product of one (‘) or two (“) prior rotations. Intrinsic rotations are used so the rotation angles retain the HCP unit cell coordinate system. Independent rotation around each axis is necessary to iterate through prismatic and pyramidal slip directions for a given basal orientation, so the Tait-Bryan z, y’, x” method is used instead of the Proper Euler method such as Z, Y’, Z”.

Figure 4-2 illustrates the chained rotation operations. The first operation rotates the vector from the r-axis around the z-axis by α in the r-θ plane creating the vector r’. The second operation rotates the vector around the θ’ axis by β in the r’-z plane creating the vector r”. This vector is the basal GPUN and shows the c-pole orientation of the crystal. A third operation rotates the vector around the r” axis by γ to evaluate different pyramidal and prismatic slip systems for a given basal orientation. The right-hand rule gives the sign of angles and β requires a negative sign to measure in the directions shown in Figure 4-2.

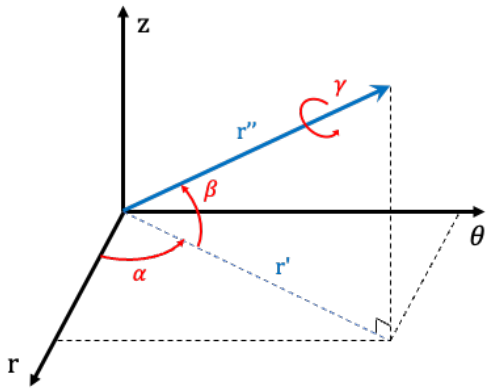

Figure 4-2: Illustration of chained rotation operations.

These rotations are individually written using second-order tensors in Equation 4-1 and condensed into one second-order tensor using inner products calculated in the order shown in Equation 4-2. The initial GPUN and SDUN vectors are multiplied by the resulting rotation matrix (g) to calculate the vectors in the desired crystallographic orientation. GPUNs are calculated by iterating through angles α and β. Basal orientations are calculated by iterating through angles α and β. All SDUNs and additional prismatic and pyramidal GPUNs are evaluated by iterating though angle γ for each basal orientation displayed on the pole figures.

$$R_z(\alpha) = \begin{bmatrix} \cos(\alpha) & -\sin(\alpha) & 0 \\ \sin(\alpha) & \cos(\alpha) & 0 \\ 0 & 0 & 1 \end{bmatrix}$$

$$R_{\theta'}(\beta) = \begin{bmatrix} \cos(\beta) & 0 & \sin(\beta) \\ 0 & 1 & 0 \\ -\sin(\beta) & 0 & \cos(\beta) \end{bmatrix} \qquad \textit{Equation 4-1}$$

$$R_{r''}(\gamma) = \begin{bmatrix} 1 & 0 & 0 \\ 0 & \cos(\gamma) & -\sin(\gamma) \\ 0 & \sin(\gamma) & \cos(\gamma) \end{bmatrix}$$

$$\mathrm{g} = R_z(\alpha)R_\theta(\beta)R_r(\gamma) \qquad \textit{Equation 4-2}$$

The rotation process reorients the GPUN (n_j) and SDUN (b_j) of the desired slip system and crystallographic orientation in the same coordinate system as the applied stress tensor (σ_{ij}). Then, the traction (t_i) and normal stress (σ_n) on the glide planes are calculated as shown in Equation 4-3 and Equation 4-4. The law of cosines is used to find the RSS (τ) on the plane in the as shown in Equation 4-5. System activity is estimated by subtracting the CRSS of the slip system from the applied RSS. Negative difference values indicate that the system is inactive while increasingly positive values indicate that the system is increasingly active. Applied stress values used for this RSS-CRSS activation analysis come from averaged yield stresses using experimental mechanical in Table 4-3 and literature equations are used for CRSS as discussed in Chapter 1 Section 3.2.2.

$$t_i = \sigma_{ij} \cdot n_j \quad \textit{Equation 4-3}$$

$$\sigma_n = t_i \cdot n_j \quad \textit{Equation 4-4}$$

$$\tau = t_i \cdot b_j \quad \textit{Equation 4-5}$$

The generalized Schmid factor (GSF) stands as a useful geometric relationship between the applied stress state and the RSS on a slip system which is generalized to multiaxial stresses. Several formulations of effective and generalized Schmid factors have been defined by other authors [60], [136], [137], [138]. This work uses the method discussed in [137] which defines the GSF according to Equation 4-6. The applied stress tensor is first normalized using the Frobenius (square root) norm to determine the GSF.

$$\mathrm{GSF} = \mathrm{b} \cdot \mathrm{g} \cdot \sigma \cdot \mathrm{g}^{\mathrm{T}} \cdot n \quad \textit{Equation 4-6}$$

Results of the RSS, CRSS, and GSF analysis are all visualized on (00.1) basal pole figures which cannot describe all slip directions or orientations of the prismatic and pyramidal glide planes. Figure 4-1 and Figure 4-2 show how the basal plane is defined and presented on the pole figure using angles α and β while the prismatic and pyramidal systems and slip directions are dependent on an additional angle, γ. The results of the analysis presented using basal pole figures display the maximum Schmid factors of γ orientations for a given (α, β) basal plane orientation. Results are visualized on a stereographic Wulff net by projecting results from the bottom of the unit sphere instead of the center.

4.3 Results

The samples are tested and characterized according to methods listed Table 4-1 and discussed in Chapter 3 Section 1 and the data are further processed using procedures described in Chapter 3 Section 2.

4.3.1 Mechanical Testing

Measured time, axial and transverse strain, and load data are recorded and shown in Figure 4-3 for both axial tension and internal pressure loading experiments. The axial and hoop strains are decomposed into elastic and plastic components and the radial strains are calculated to help reveal the mechanical anisotropy which are shown in Figure 4-4 and Table 4-3. An isotropic material would produce equal plastic strain rates for unloaded axes from the axial tension loading in Figure 4-4 (a), but results reveal the radial strain rate is less than the transverse strain rate. Results from the internal pressure test in Figure 4-4 (b) are less clear because the Poisson effect competes with positive tensile stress in the axial axis. The mechanical testing results of all samples are shown in Figure 4-5.

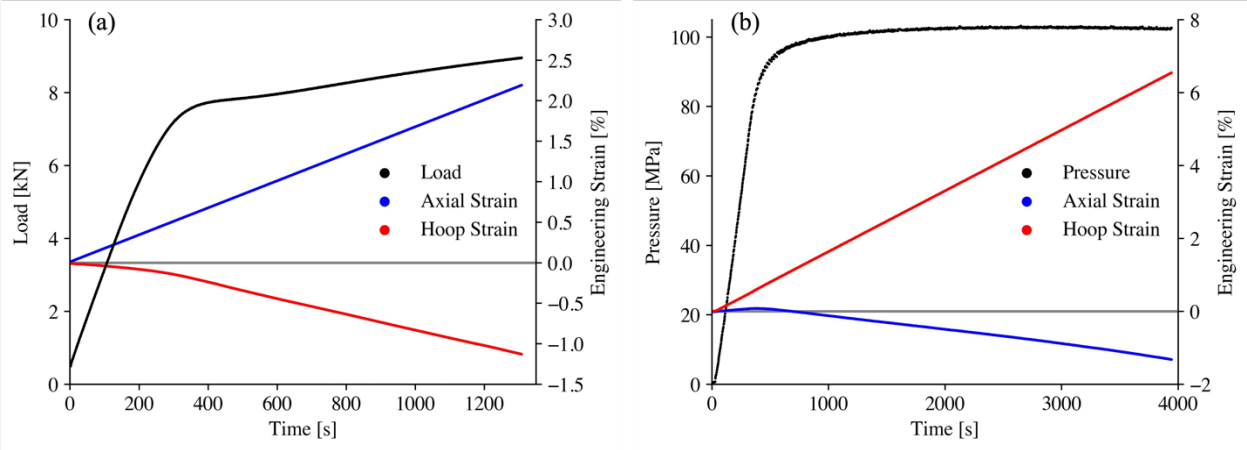

Figure 4-3: Representative experimental data measured during mechanical testing. Data shown for samples tested at room temperature using (a) axial mode and (b) pressure mode.

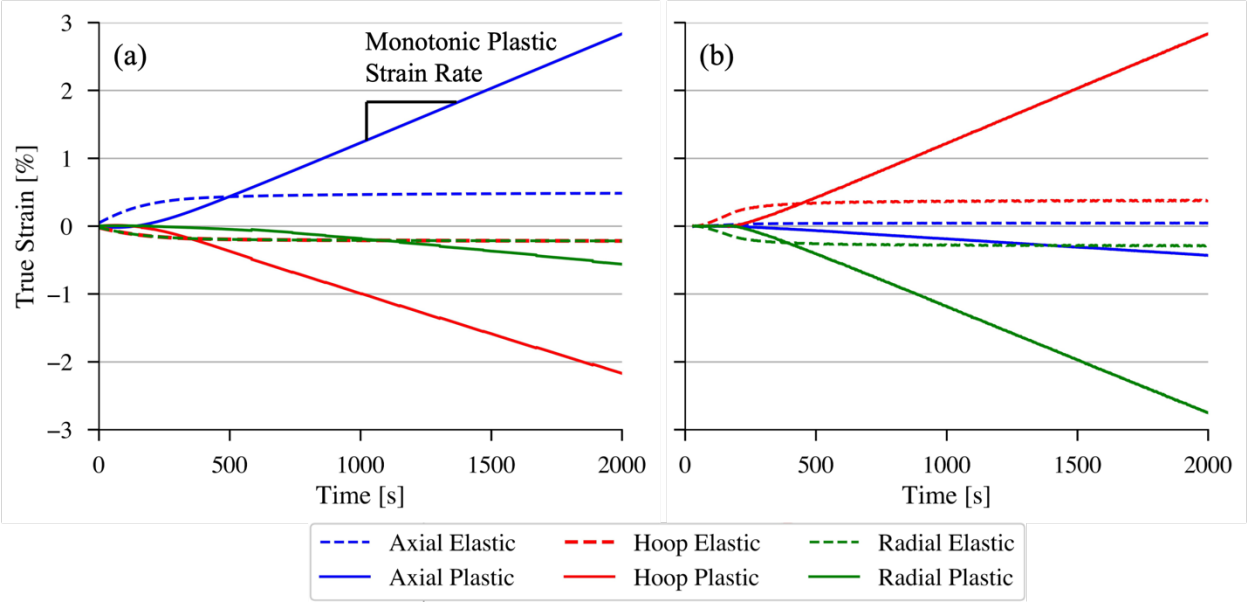

Figure 4-4: (a) Axial test and (b) internal pressure test strain decomposition at 400 °C.

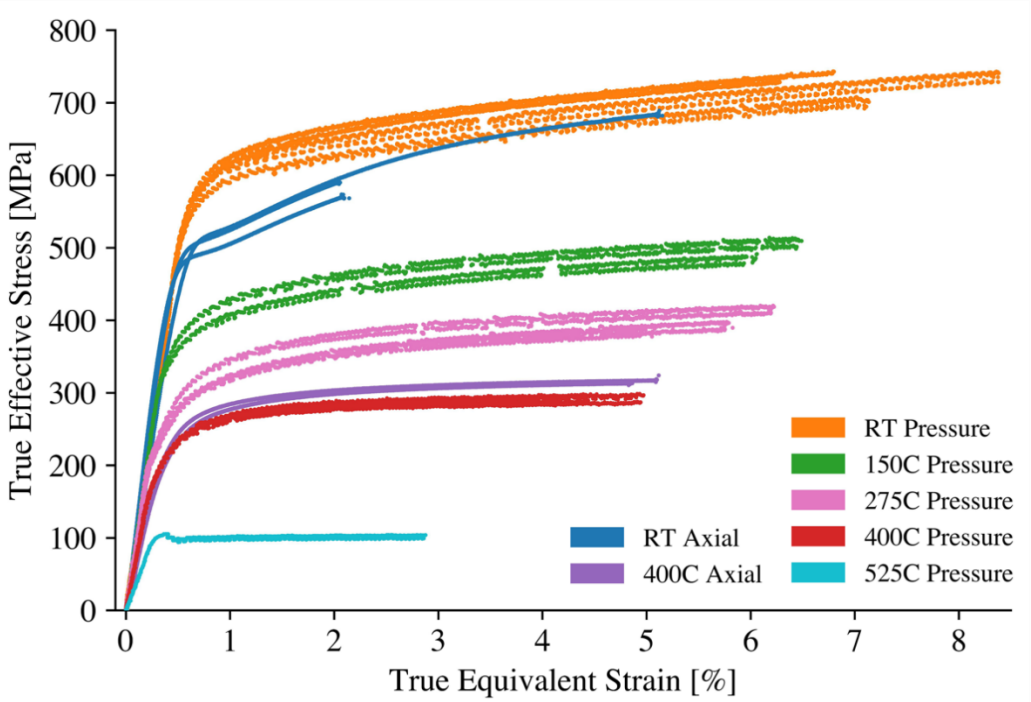

Figure 4-5: Mechanical data summary of all samples tested in the study of plasticity.

Mechanical properties shown in Table 4-3 are generally consistent at a given temperature and in good agreement with literature values plotted in Figure 4-6 - Figure 4-8. Data in these figures from axial tension tests are plotted as squares, data from ring tension tests are plotted as triangles, and data are plotted as dots when only effective stresses are listed with no additional information on testing direction. For the measured Young's modulus values shown in Figure 4-6, data from both internal pressure and axial tension tests are in good agreement with literature from a large variety of sources up to 400 °C [14], [19], [32], [82], [139], [140], [141], [142], [143], [144], [145], [146], [147], [148], [149], [150], [151]. Changes in are most notable between 275°C and 400°C. Over this temperature range, Young's modulus decreases from an average value of 84.5 GPa to an average value of 68.4 GPa. Measured values for Poisson's shown in Figure 4-7 are slightly higher than literature data with an increasing trend with temperature [19], [139], [141], [142], [146], [147], [149], [152]. The von Mises effective yield stress values shown in Figure 4-8 are also consistent with literature values [32], [45], [47], [139], [140], [142], [146], [153], [154], [155], [156], [157], [158]. At room temperature, the von Mises effective yield stress is 420. ± 19 MPa for axial tension testing and 529 ± 17 MPa for internal pressure testing, displaying significant mechanical anisotropy. This effect is significantly reduced at elevated temperatures where the effective yield stress is 171 ± n/a MPa for axial tension loading and 186 ± 4 MPa for internal pressure loading.

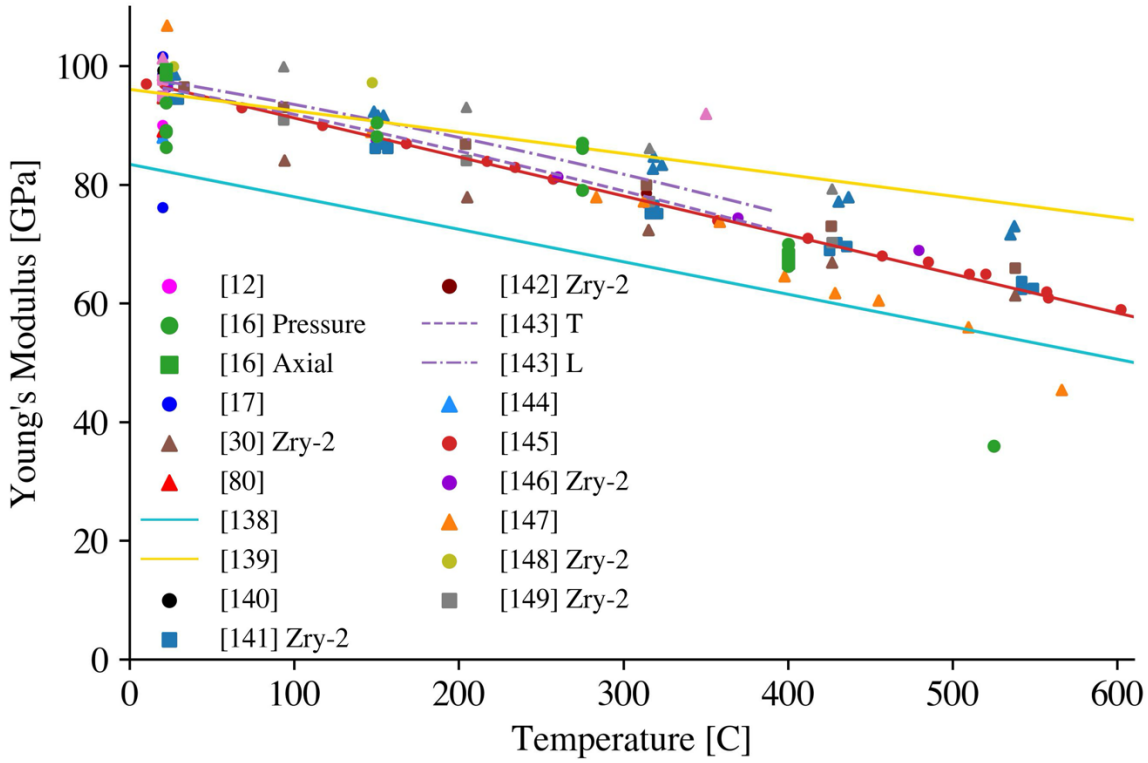

Figure 4-6: Young's modulus literature comparison. Measurements from [16] *are part of this work, measurements from* [143] *marked with T and L designate transverse (hoop) and longitudinal (axial) measurement respectively, and Zry-2 samples are marked with all others being Zry-4.*

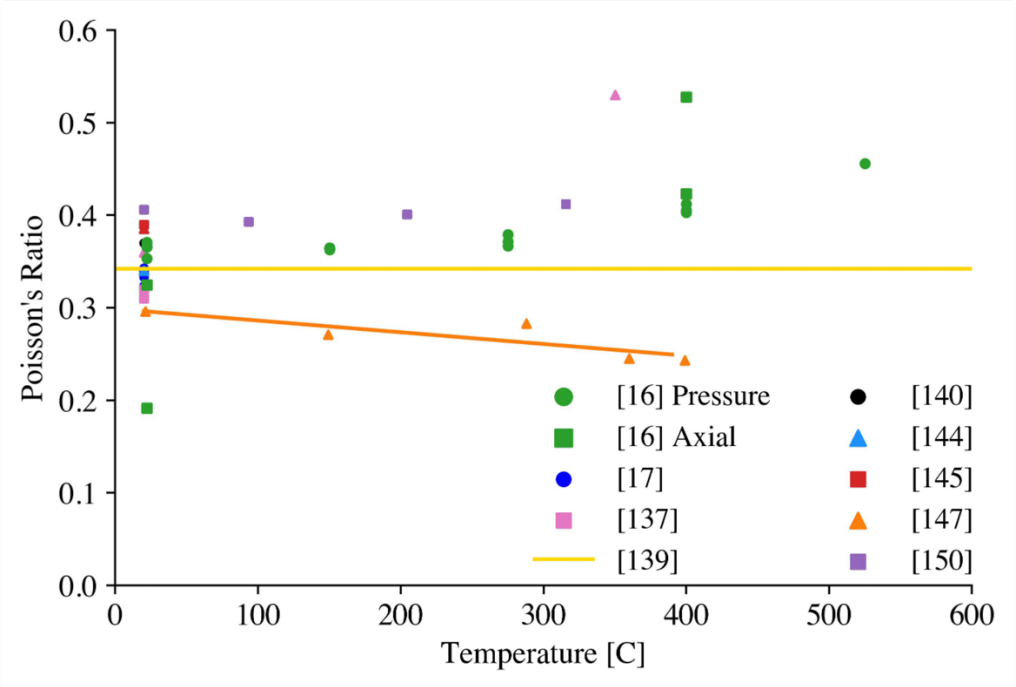

Figure 4-7: Poisson's ratio literature comparison. Measurements from [16] *are part of this work.*

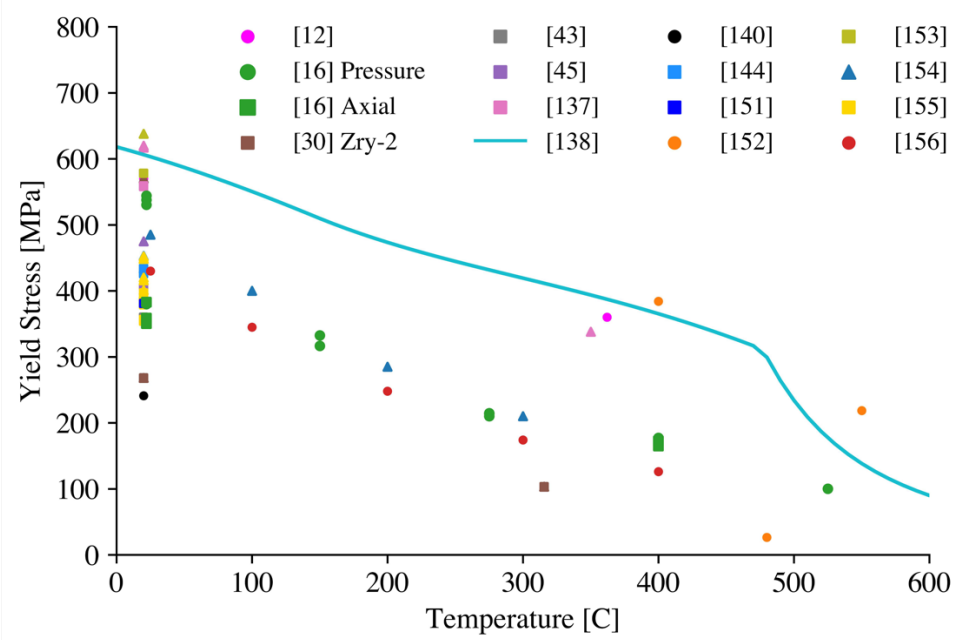

Figure 4-8: Yield stress literature comparison. Measurements from [16] *are part of this work and Zry-2 samples are marked with all others being Zry-4.*

Table 4-3: Results of mechanical testing

Sample ID	E [GPa]	υ	YS_{eff} [MPa]	$\dot{\epsilon}_z^p$ [x10^{-6}/s]	$\dot{\epsilon}_\theta^p$ [x10^{-6}/s]	$\dot{\epsilon}_r^p$ [x10^{-6}/s]	$\epsilon_{max\ eq}$ [%]
AX-RT-1	95.5	0.335	414	15.3	- 11.4	- 3.85	2.08
AX-RT-2	93.6	0.225	405	15.4	- 9.62	- 5.53	2.02
AX-RT-3	91.2	0.369	442	31.1	-19.6	- 10.9	5.15
AX-400-1	68.7	0.419	170.	16.0	- 11.8	- 3.75	5.12
AX-400-2	64.4	0.369	171	16.0	- 13.1	- 2.18	4.91
PR-RT-1	90.0	0.368	541	- 3.98	15.7	- 13.5	6.80
PR-RT-2	89.5	0.366	541	- 4.28	15.4	- 12.8	8.38
PR-RT-3	87.5	0.372	527	- 3.90	15.7	- 13.6	6.29
PR-RT-4	90.4	0.364	506	- 4.40	15.8	- 13.1	7.15
PR-150-1	90.1	0.365	372	- 6.56	15.9	- 10.9	6.07
PR-150-2	88.6	0.367	392	- 6.17	15.8	- 11.3	6.50
PR-275-1	87.7	0.370	227	- 5.27	15.9	- 12.4	5.07
PR-275-2	80.0	0.380	217	- 4.98	15.8	- 12.6	5.83
PR-275-3	86.0	0.370	257	- 5.04	15.9	- 12.6	6.23
PR-400-1	70.3	0.406	191	- 2.42	16.1	-15.6	4.15
PR-400-2	68.6	0.402	185	- 2.52	16.1	-15.5	4.43
PR-400-3	66.4	0.411	183	- 2.48	16.1	-15.5	4.98
PR-525-1	36.5	0.463	104	- 3.85	16.4	-14.4	2.89

4.3.2 Microstructure Characterization

The AX-RT-1 sample has low strain (2.08 %) compared to the PR-RT-1 sample (6.80 %), preventing these samples from testing Hypothesis 2 from Chapter 2. However, the AX-400-1 sample has higher strain (5.12 %) than the PR-400-1 sample (4.15 %) which could provide strong evidence supporting the hypothesis if the PR-400-1 sample produces more defect energy than the AX-400-1. Further, elevated temperature deformation is more prototypic of reactor conditions. Therefore, for brevity, results presented in this section are limited to the pristine sample (REF), the sample deformed by internal pressure at 400 ºC (PR-400-1), and the sample deformed by axial tension at 400 ºC (AX-400-1). The sample names included in Table 4-1 and Table 4-3 (REF, AX-400-1, PR-400-1) are adjusted to "pristine", "uniaxial-deformed", and "biaxial-deformed", respectively, for clarity.

The pristine and biaxial-deformed samples are first analyzed in detail for prototypic pristine and deformed microstructures including a single grain analysis for comparison between 3DXM and EBSD results. Then the pristine, uniaxial-deformed, and biaxial-deformed microstructures are compared to investigate the effects of loading mode and resulting plastic strain ratio on the deformation microstructures. The residual cold-worked microstructure from pilgering and annealing display similar characteristics to the deformation microstructure, so both are referred to as un-recrystallized (uRX) microstructure.

4.3.2.1 3D X-Ray Microscope

The live signal of a scan on the charge-coupled device are detector with the platinum wire is shown in Figure 4-9 displaying many Laue diffraction peaks resolved from different diffraction conditions throughout the beam depth. These are reconstructed into the Laue diffraction patterns for each voxel which are matched to a simulated diffraction pattern as shown in Figure 4-10. The simulated peak patterns provide the orientations of each voxel which are shown in Figure 4-11 using IPF micrographs. The index rate declines with depth as the X-rays must diffract further out of the sample so micrographs are truncated to show the depths with relatively high index rate.

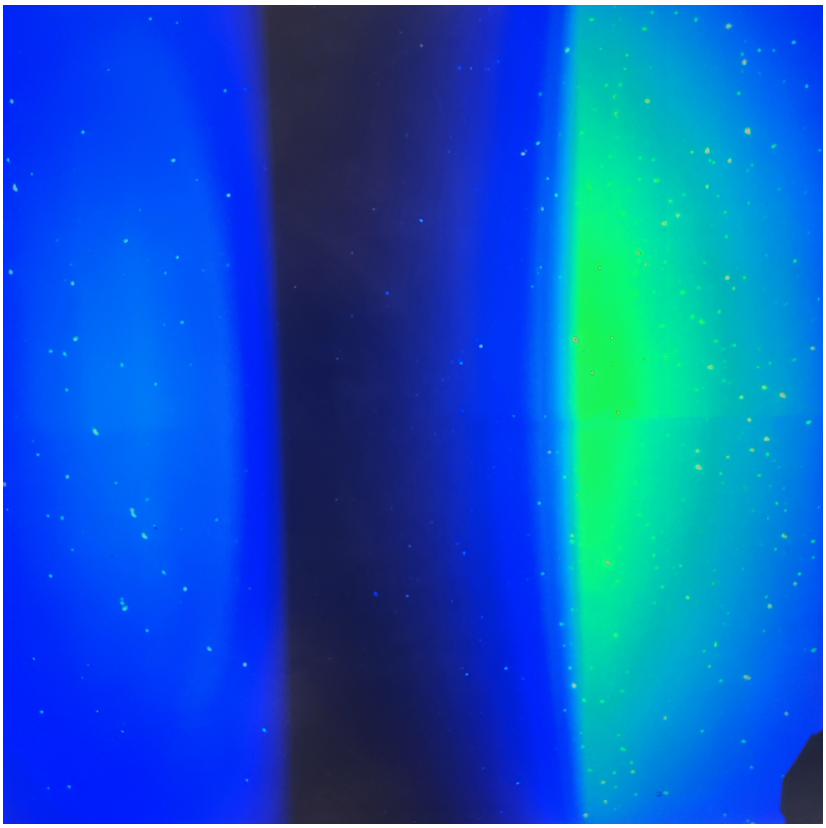

Figure 4-9: Live data from the charge-coupled device area detector with platinum wire in the middle of the scan.

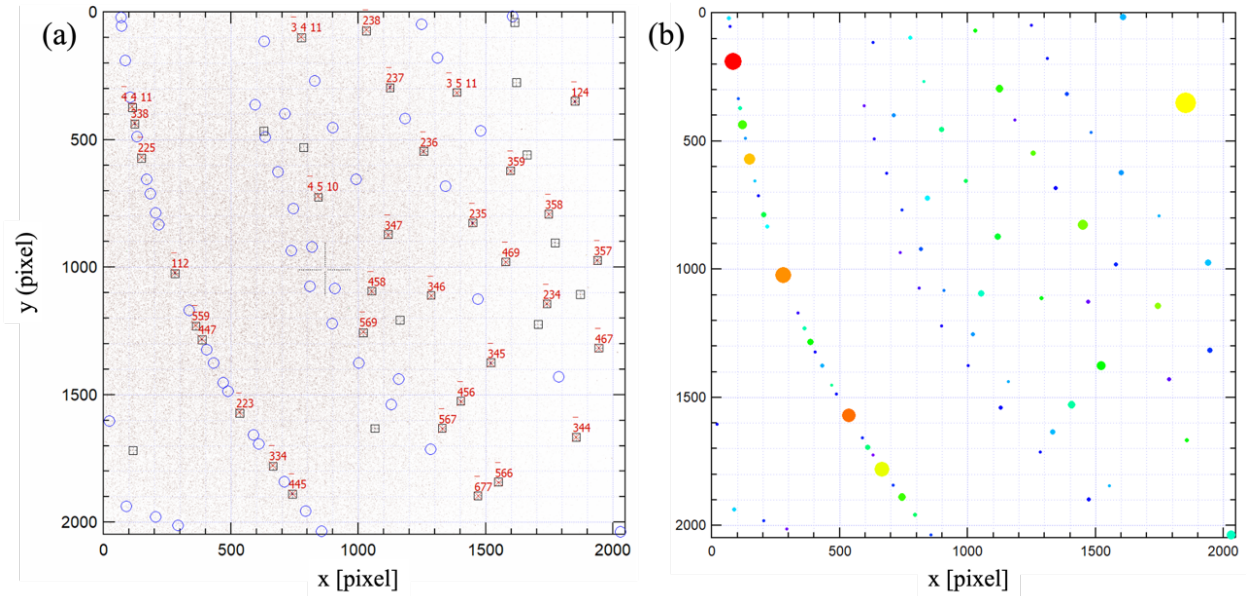

Figure 4-10: (a) Reconstructed Laue diffraction pattern of a voxel with the corresponding simulation of the diffraction pattern shown in (b). Expected diffraction peaks in (a) with matched measurements are identified with boxes and those without peaks are shown plotted as circles.

The basal (00.2) orientation characteristics of the pristine and biaxial-deformed samples are shown in Figure 4-11. The orientation data are presented in the sample coordinate system using ND projection pole figures with each voxel directly projected on the pole figure. The micrographs show the indexed voxels of the illuminated plane displaying the orientation data using the ND pole figure coloring. Figure 4-12 is included to help relate the RD-TD axes used to display the ND projection of the sample surface and the X-Z axes of the illuminated plane. The 3DXM acquires a relatively high index rate in the pristine sample and a low index rate in the biaxial-deformed sample and the micrograph sizes are adjusted to display areas with relatively high index rates. Only one grain in the biaxial-deformed sample is well-resolved, so a grain with similar orientation and size is selected from the pristine results for direct comparison. The grain in the pristine sample is 7.1 μm and the grain in the biaxial-deformed sample is 5.7 μm, which are marked in Figure 4-11 to show the grain orientations (a)-(b) and morphologies (c)-(d). The basal DAO of these grains are shown in Figure 4-11 (d)-(f) with the basal orientations within ± 0.05° for the pristine grain and ± 1.5° for the biaxial-deformed grain.

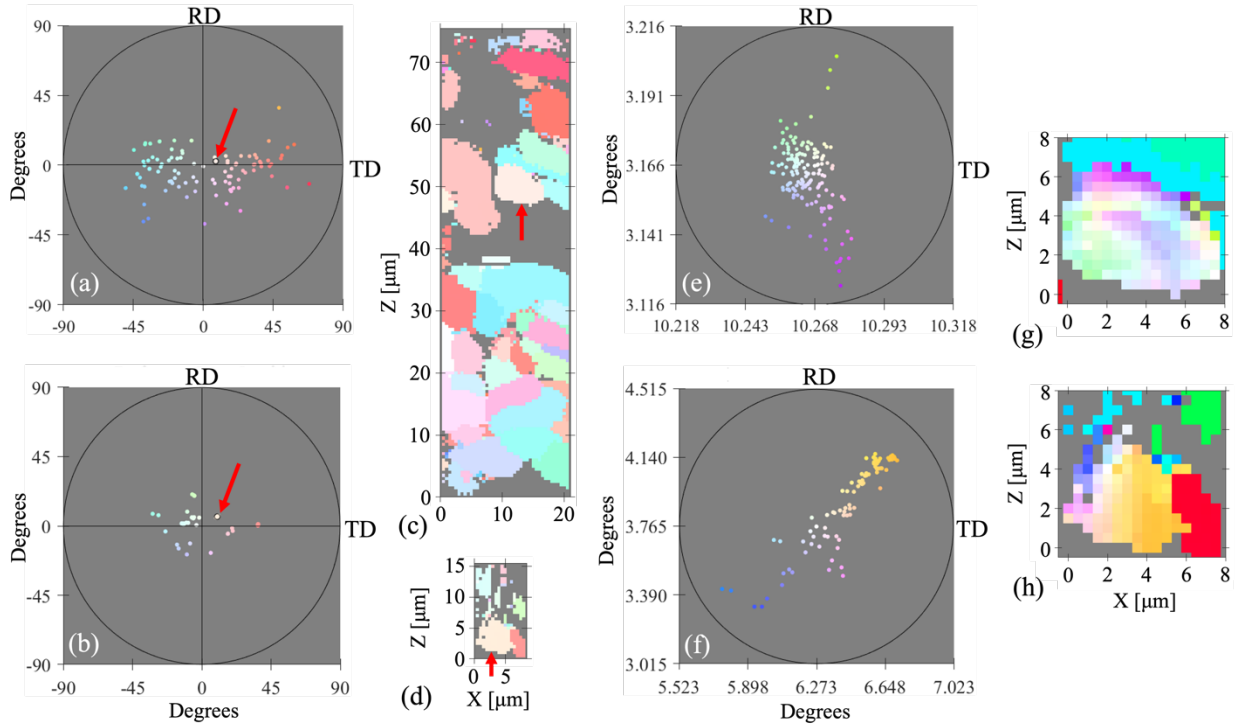

Figure 4-11: Basal (00.2) orientation characteristics of the pristine (a), (c), (e), (g) and biaxial-deformed (b), (d), (f), (h) samples. ND pole figures show the texture (a)-(b) and intragranular disorientation (e)-(f) and provide the coloring used by the corresponding IPF micrographs of the illuminated plane, (c)-(d) and (g)-(h), respectively. Grains are marked using arrows in (a)-(d) for single grain analysis and (e)-(h) show the intragranular disorientation of each grain.

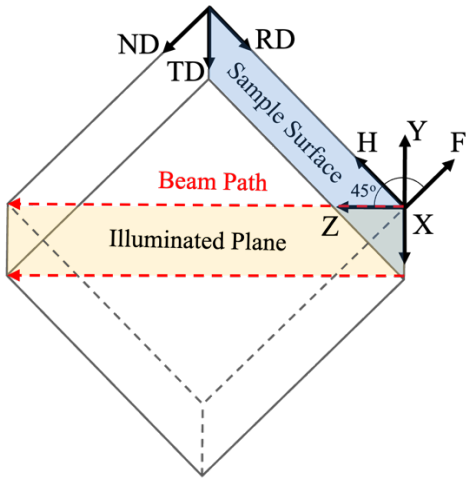

Figure 4-12: Schematic of the sample coordinate system (X, F, H) and beamline coordinate system (X, D, Z).

The lattice strain components of the chosen pristine and biaxial-deformed grains are shown in Figure 4-13 (a)-(f) using red and blue to indicate tension and compression, respectively. Histograms with Gaussian fits are included in Figure 4-13 (g)-(i) to better quantify the strain variation which are significantly higher in the biaxial-deformed sample and display localized tension-compression variations compared to the pristine sample. The relationship between the trace lattice strains (HH, XX, FF) and the sample axes (RD, TD, ND), respectively, is provided in Figure 4-12. The lattice strain components are used to calculate the equivalent strains and the *a/c* ratio variation assuming constant unit cell volume. The results of the equivalent strain and *a/c* ratio variation are shown in for all indexed pixels (a)-(b) and the single grain analysis (c)-(d). Particularly within the single grain, the pristine sample displays narrow distributions of these metrics. The average (μ) and standard deviation (σ) fitting parameters for the distributions are listed in Table 4-4. The lattice parameters measured using the monobeam energy scans in Figure 4-15 are a = 0.32289 nm and c = 0.51435 nm which are similar to the results of pure zirconium [30].

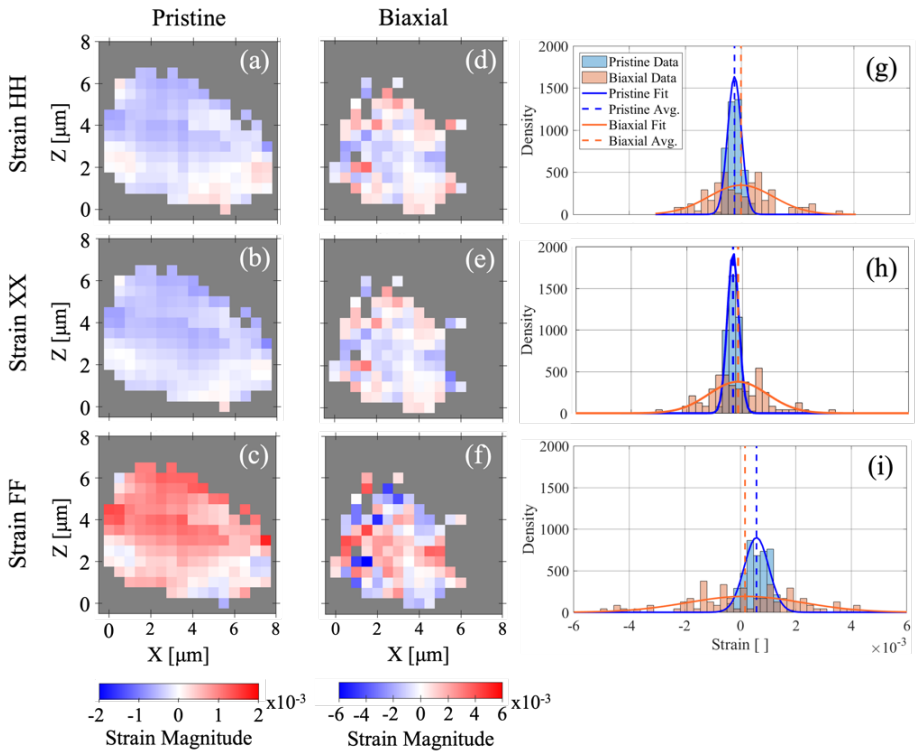

Figure 4-13: Trace strain components of intragranular analysis shown using 2D micrographs (a)-(f) and probability density function histograms (g)-(i). Note the different limits of the color bars for the pristine (a)-(c) and biaxial-deformed (d)-(f) samples; the strain magnitude variation is more clearly shown point by point using the histograms (g)-(i). Red indicates tension and is shown as positive strain and blue indicates compression and is shown as a negative strain.

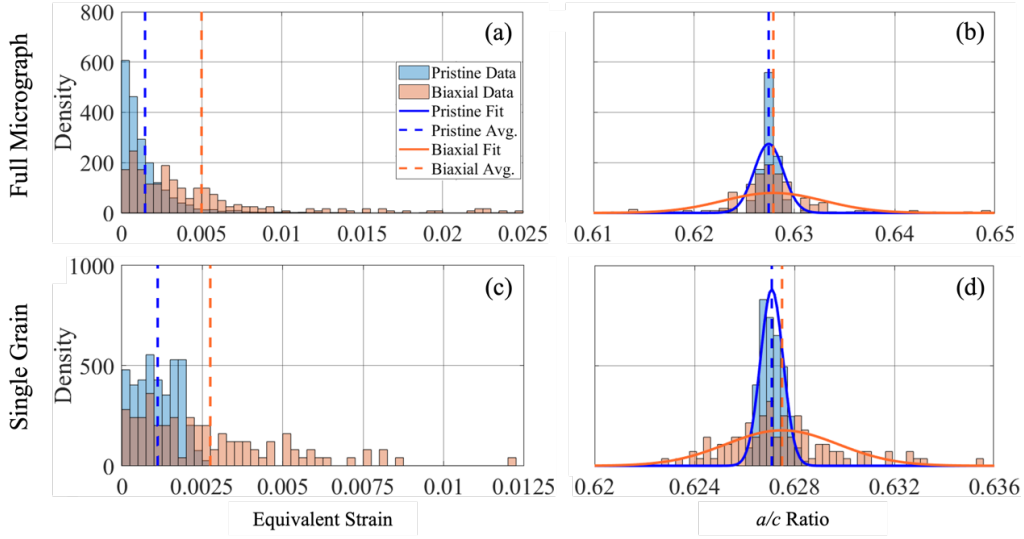

Figure 4-14: Histograms of the (a) von Mises lattice strain and (b) lattice parameter ratio of all indexed voxels. The corresponding values of single grains selected for analysis are plotted in (c) and (d). The lines plotted in (c)-(d) show the c/a ratio calculated from the measured lattice parameters.

Table 4-4: Mean (μ) and standard deviation (σ) of the strain and a/c ratio distributions shown in Figure 4-13 and Figure 4-14.

Single Grain	Pristine		Biaxial-Deformed	
	μ	σ	μ	σ
HH (RD) Strain x 10^{-3} [ ]	-0.25	0.24	-0.020	1.2
XX (TD) Strain x 10^{-3} [ ]	-0.33	0.21	-0.15	1.1
FF (ND) Strain x 10^{-3} [ ]	0.58	0.44	0.17	2.1
Equivalent Strain x 10^{-3} [ ]	1.11	-	2.75	-
a/c Ratio	0.6271	0.0005	0.6275	0.0023
Full Microstructure				
Equivalent Strain x 10^{-3} [ ]	1.47	-	4.99	-
a/c Ratio	0.6274	0.0015	0.6279	0.0050

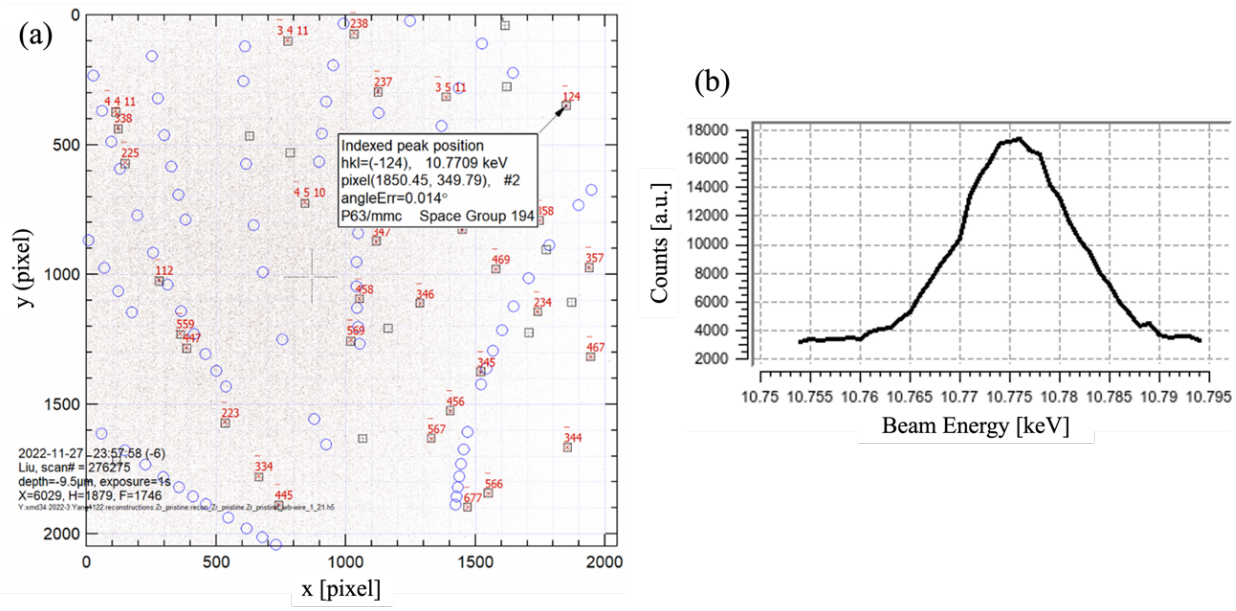

Figure 4-15: (a) Reconstructed Laue diffraction pattern of a voxel showing the $\{\bar{1}2.4\}$ diffraction peak which is selected for a monoenergy scan shown in (b) to determine the ideal diffraction conditions.

4.3.2.2 Electron Backscatter Diffraction

The pristine, as-received microstructure and texture of CWSR Zry-4 cladding are shown in Figure 4-16 and Figure 4-17. Figure 4-16 provides IPF micrographs showing the bimodal RX and uRX microstructures at three magnifications with strong basal texture indicated by the IPF coloring using the ND projection (ND||IPF). This texture is better quantified in Figure 4-17 using

basal (00.2) and prismatic type 1 {10.0} pole figures. The microstructure of each sample at all magnifications are examined for twin systems discussed in Chapter 1 Section 3.1.2 and Chapter 3 Section 2.2, but no twins are identified.

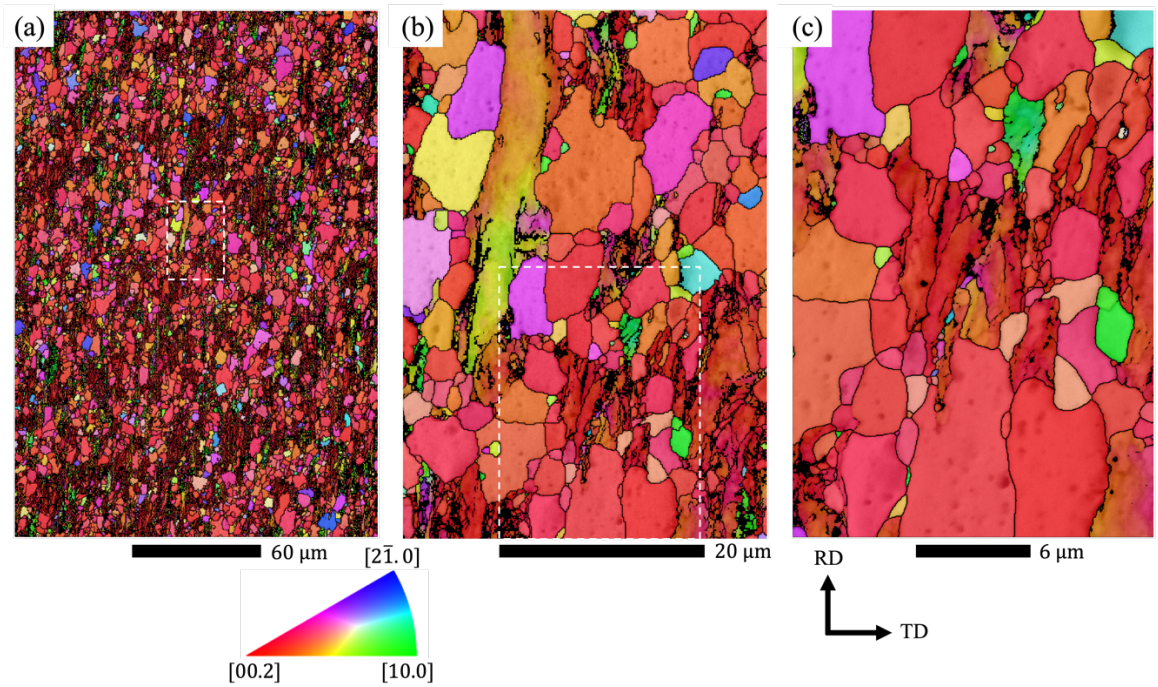

Figure 4-16: Micrographs of pristine CWSR Zry-4 cladding using ND||IPF coloring at (a) 600x (b) 4000x and (c) 7500x magnification. Dashed overlays show areas characterized at higher magnification.

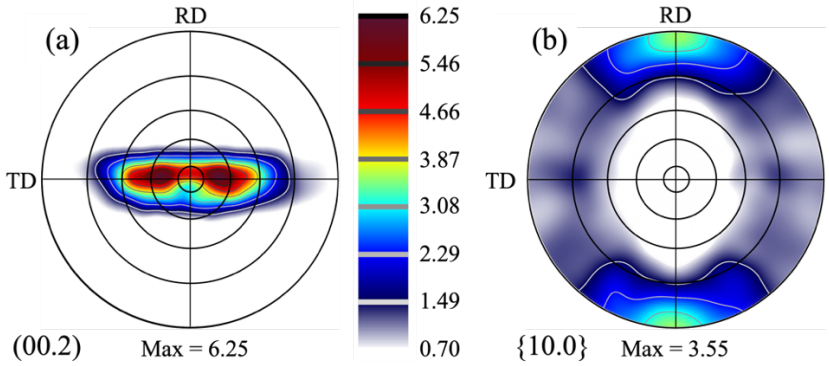

Figure 4-17: (a) Basal (00.2) and (b) prismatic type I {10.0} texture pole figures of pristine CWSR Zry-4 cladding from characterization at 600x magnification. The (00.2) pole figures are projected on a stereographic Wulff net with reference circles at 10°, 30°, 50°, 70°, 90° from normal.

Figure 4-18 shows the microstructure characteristics of the pristine, biaxial-deformed, and uniaxial-deformed samples using ND||IPF micrographs at 4000x magnification. The residual cold-worked microstructure from pilgering and annealing during manufacturing display similar characteristics to the deformation microstructure, so are collectively referred to as un-recrystallized (uRX) microstructure herein. Grains are elongated by approximately 50% in the RD, and the uRX fraction is higher in the deformed sample compared to the pristine sample. The band

slope and index rate are high in RX grains, but the band slope is much lower in the uRX microstructure which corresponds with most of the unindexed points. Additional histograms and micrographs are available in Chapter 8 Section 5 to help visualize and quantify these characteristics.

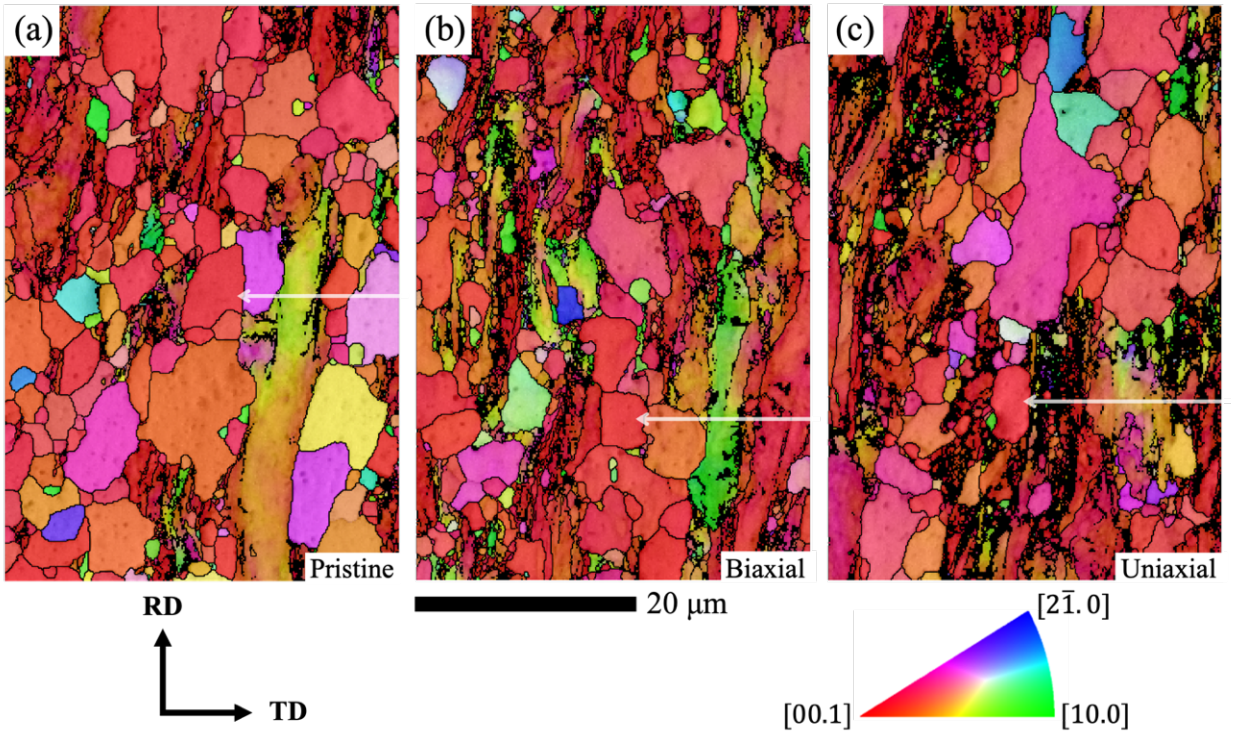

Figure 4-18: EBSD ND||IPF micrographs for (a) pristine, (b) biaxial-deformed, and (c) uniaxial-deformed samples. Grain boundaries with more than 10^o misorientation are marked with black lines and arrows in show grains selected for single grain analysis.

Single grains from each sample marked in Figure 4-18 are selected with similar orientations and sizes to those used in the 3DXM analysis to compare results of both characterization methods. The pristine grain is 6.31 µm, the biaxial-deformed grain is 4.91 µm, and the uniaxial-deformed grain is 5.08 µm and each grain has similar orientations to those used for the 3DXM single grains which are defined in Chapter 8 Section 5. The deformed grains display similar DAO and KAM compared to the pristine grain in Figure 4-19, although both grains selected are RX with relatively low misorientation compared to uRX microstructure.

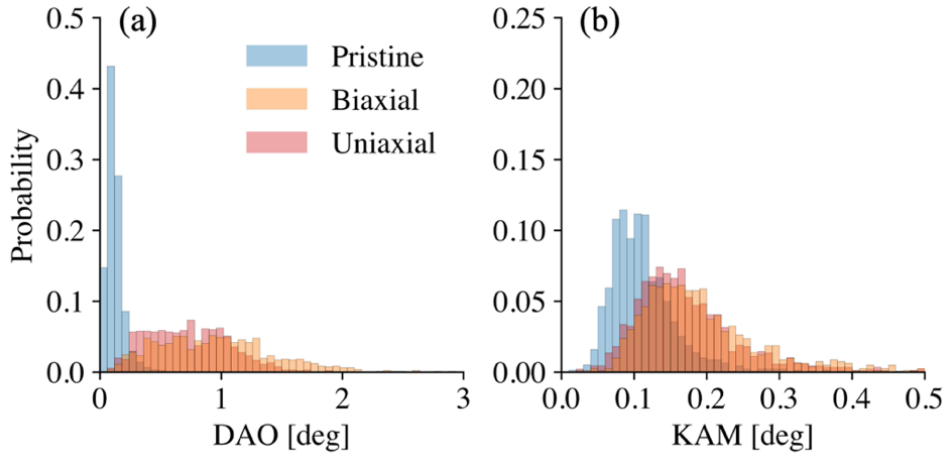

Figure 4-19: Histograms of EBSD results for selected single grains marked in Figure 4-18 showing (a) the DAO and (b) the KAM at 4000x magnification.

Grain size cumulative area fractions are shown in Figure 4-20 at 4000x and 600x magnifications. The 600x magnification effectively captures large grains, while the 4000x magnification provides detailed resolution of small grains, ensuring a comprehensive analysis of the grain size distribution. The deformed samples display cumulative area fractions higher than the pristine area fraction up to about 9 μm, indicating a smaller grain size distribution. The uniaxial-deformed sample displays a grain size distribution similar to the biaxial-deformed sample with a slightly lower area fraction for intermediate sized grains.

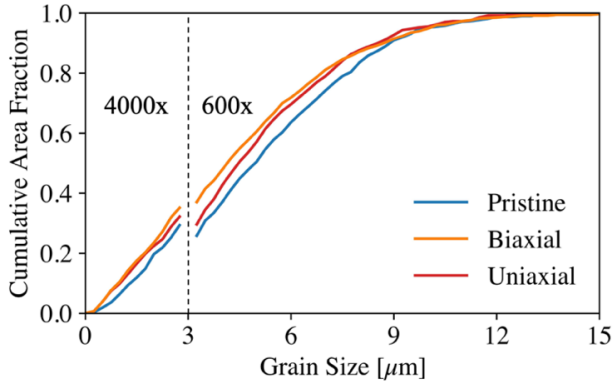

Figure 4-20: Grain size distribution shown using the cumulative area fraction of each sample. Grain sizes below 3 μm are derived from the 4000x micrographs, while those above are from the 600x micrographs.

High magnification KAM micrographs show orientation gradients present in pristine (a) and deformed (b)-(c) microstructures in Figure 4-21. Typical areas are segmented to reveal representative deformation structures in detail, but the full micrographs are included in Chapter 8 Section 5. Figure 4-21 (a) shows an area from the pristine sample, displaying typical undeformed RX grains with some residual uRX microstructure from manufacturing. The low-angle orientation gradients in Figure 4-21 (b) form walls around domains with low misorientation and in (c) many of these domains have achieved the necessary misorientation to classify as nanoscale sub-grains.

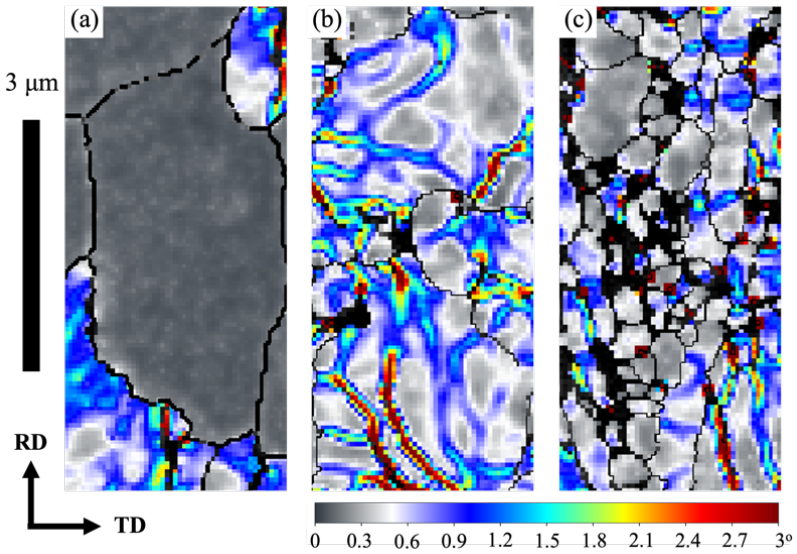

Figure 4-21: High magnification (7500x) micrographs showing the KAM data for typical microstructure from the (a) pristine and (b)-(c) biaxial-deformed samples.

Similar to the previous single grain analysis, deformation in the microstructure is quantified using DAO and KAM but is assessed at different length scales on several microstructure categories: total, RX, and uRX. Grains larger than 1 µm with low intragranular misorientation are classified as RX grains, nanograins with low misorientation are classified as sub-grains, and the remaining microstructure with high misorientation are classified as uRX. The area fractions are reported in Table 4-5 and the intragranular deformation characteristics of these microstructure categories are compared using DAO and KAM histograms, as summarized in Figure 4-22. The RX fraction decreases while the sub-grain and uRX fractions increase between the pristine and deformed samples, and similarly, the RX and DAO values are higher in the deformed samples compared to the pristine sample. However, the biaxial-deformed sample shows more significant changes in the total and RX categories compared to the pristine sample than the uniaxial-deformed sample does. No difference is observed in the uRX fraction between any of the samples. Additional data are included in the Chapter 8 Section 5.

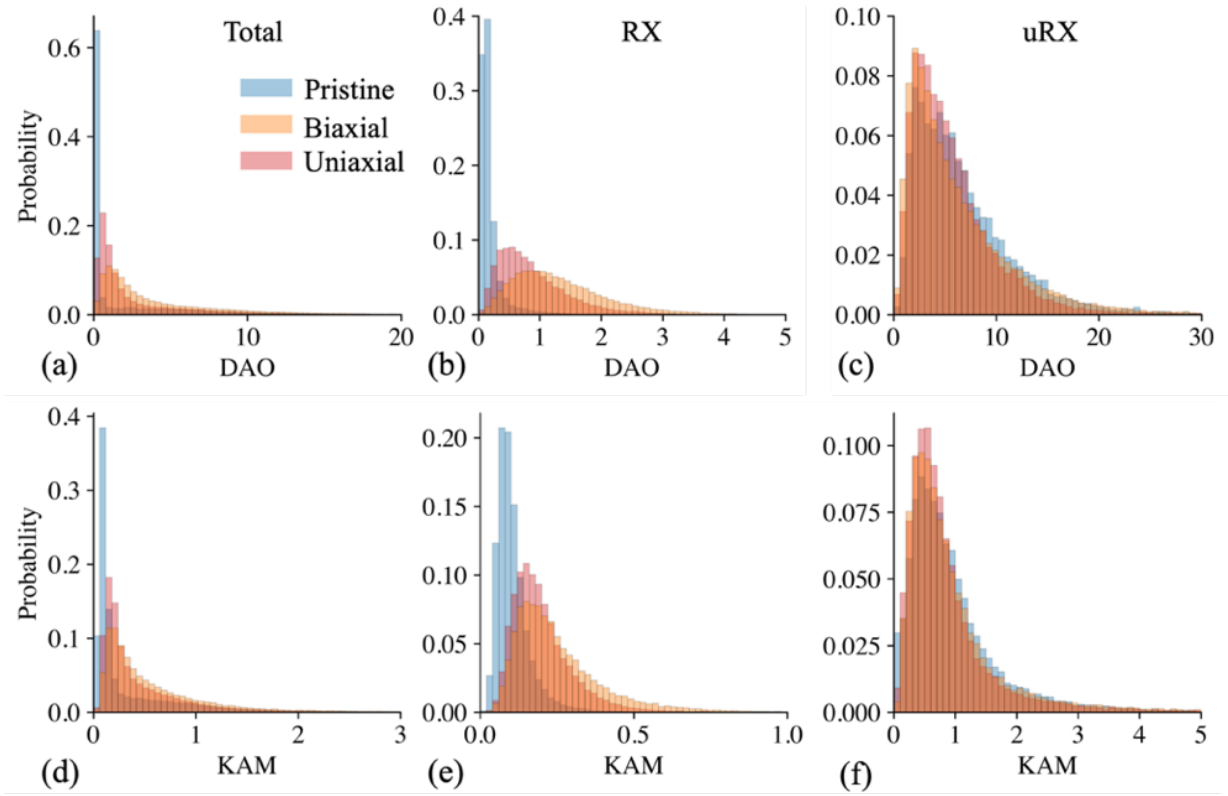

Figure 4-22: Total, RX, and uRX misorientation characteristics quantified using (a)-(c) DAO at 600x magnification and (d)-(f) KAM at 4000x magnification.

The RD texture shown in Figure 4-23 display typical $\{2\bar{1}.0\}$ and $\{10.0\}$ fibers for the RX and uRX microstructure categories [15]. The uRX fiber is particularly strong and decreases from the pristine to the biaxial-deformed sample microstructures but increases from the pristine to the uniaxial-deformed sample microstructures. Multiple RX-uRX partitioning techniques are performed to ensure this effect is not an artifact of the higher misorientation in RX fraction of the biaxial-deformed sample, but these texture characteristics are consistent. Partitioning methods include the KAM-based methods described in Chapter 3 Section 2.2 with results presented in Figure 4-23, band slope filtering, and manual selection at 600x and 4000x magnification. Additional figures are provided in the Chapter 8 Section 5 to help quantify these data.

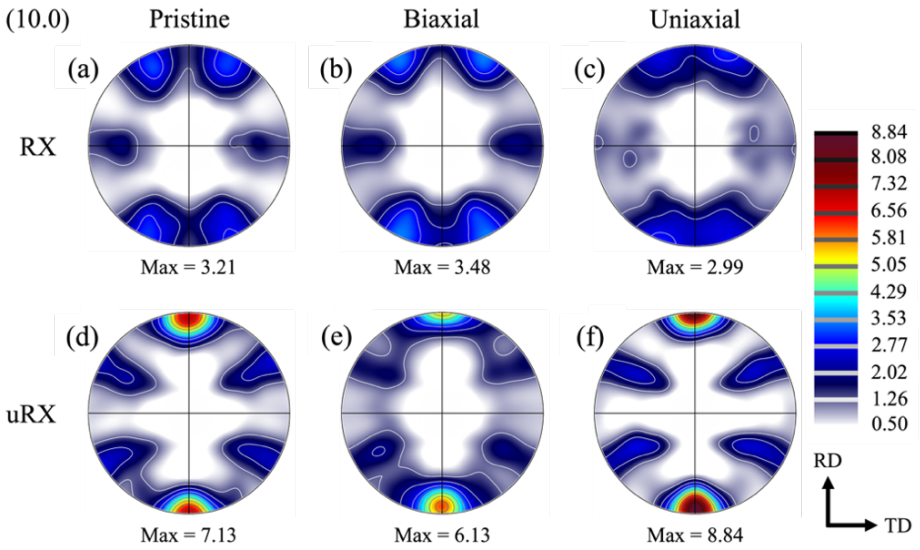

Figure 4-23: Prismatic (10.0) texture of the (a)-(c) RX and (d)-(f) uRX fractions for each sample at 600x.

Table 4-5: Summary of EBSD data.

	Pristine		Biaxial-Deformed		Uniaxial-Deformed	
	600x	4000x	600x	4000x	600x	4000x
Index Rate:	77%	90%	81%	82%	49%	75%
Grain elongation – median:	1.51	-	1.43	-	1.64	-
Average:	1.45		1.50		1.09	
RX:	0.58	0.65	0.32	0.40	-	0.52
Area Fraction – sub-grain:	-	0.021	-	0.032	-	0.027
uRX:	-	0.32	-	0.55	-	0.43

4.3.3 Viscoplastic Self-Consistent Simulations

The plastic spin is defined as the difference between the material spin and the lattice spin corresponding to rotation from plastic slip only [89], [132]. Figure 4-24 shows the VPSC simulation results of the plastic spin for the pristine microstructure at 600x magnification for different initial velocity tensors which Figure 4-25 summarizes using histograms for all magnifications. The results using the macroscopic velocity gradient tensor defined by the biaxial strain rates display higher plastic spin distributions compared to results defined by the uniaxial strain ratios while all other variables are constant. The applied velocity gradient tensors of both uniaxial tests are similar, particularly by including the same ND strain rate which is small compared to the biaxial velocity tensor. However, switching the tensile axis results in the uniaxial-TD simulation displaying higher plastic spin than the uniaxial-RD simulation, especially at higher magnifications with large area and reduced variability.

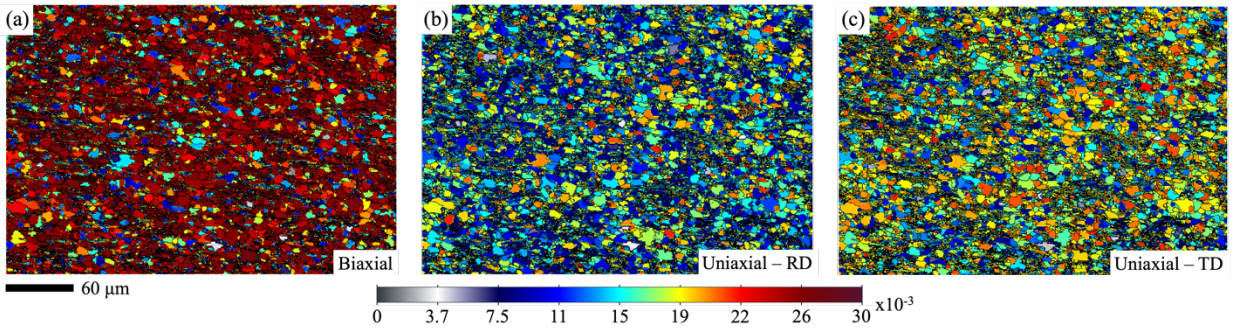

Figure 4-24: Micrographs showing the VPSC simulation plastic spin results at 600x magnification for the (a) biaxial, (b) uniaxial-RD, and (c) uniaxial-TD velocity tensors.

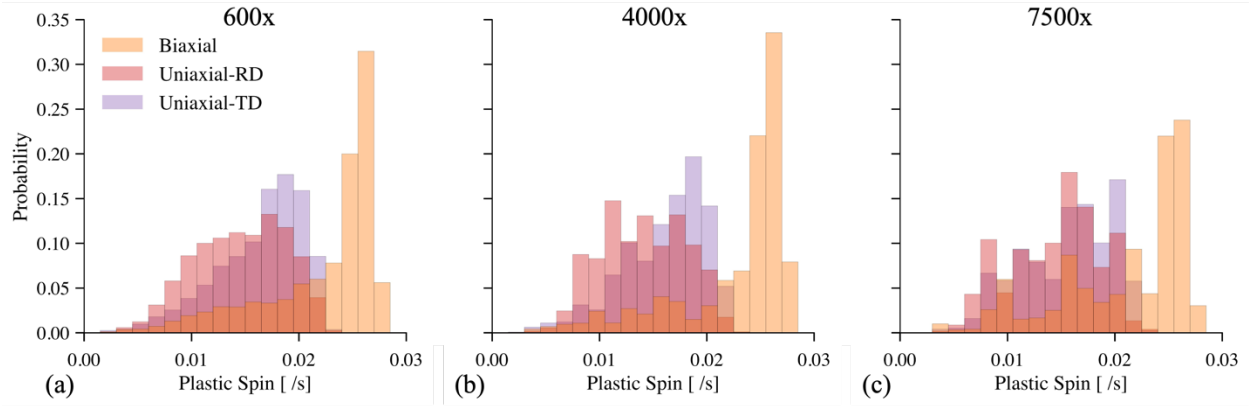

Figure 4-25: Histograms summarizing the VPSC simulation plastic spin results at (a) 600x (b) 4000x, and (c) 7500x magnification. Note that higher magnification and reduced area introduces variability in the distributions.

4.3.4 Resolved Stress Analysis

Calculated GSF results for prismatic <a>, basal <a>, and pyramidal <c+a> slip systems are visualized on (00.2) basal pole figures in Figure 4-26 for the four stress states included in Table 4-2. For uniaxial stress states, the GSF results for the basal systems are the simplest to interpret because the glide plane normal corresponds to the pole figure. These show low GSF (0-0.2) for orientations that are colinear or normal to the loading axis and high GSF (0.4-0.5) bands at 45o from the loading axis. The prismatic systems have additional glide plane orientations that are evaluated so the GSF is low only where the glide planes are nearly aligned with the loading axis. The pyramidal planes have even more glide systems and have a c-component resulting in high GSF except for medium GSF (0.2-0.4) bands at 45o from the loading axis.

The biaxial stress states produce lower GSF over all slip systems. The prismatic systems have particularly low GSF zones centered around 45° and 30° from normal in the TD for the pressure and PCI stress states, respectively. These angles are related to the biaxial stress state by the law of cosines. The biaxial stress calculations for basal and pyramidal systems show similarities to the uniaxial stress states compounded with each other. As the biaxial stress state approaches unity, the pole figures become axisymmetric around the ND.

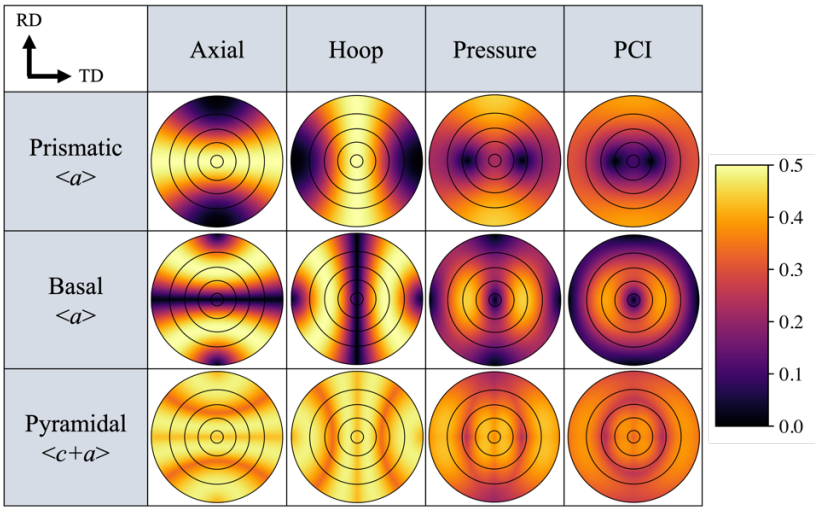

Figure 4-26: Generalized Schmid factors of three slip systems under four different stress states visualized using the color bar on the right of the figure. The (00.2) pole figure is projected on a stereographic Wulff net with reference circles at 10º, 30º, 50º, 70º, 90º from normal.

The relationship between orientation, GSF, and texture intensity are represented using the histograms shown in Figure 4-27. For the axial case, the high GSF band for prismatic planes aligns with the high texture intensity band so nearly all the microstructure has a high prismatic GSF. Conversely, the low GSF band for basal planes aligns with the high texture intensity resulting in especially low basal GSF for most of the microstructure in the axial stress state. The hoop stress state is more distributed as the high/low GSF bands for prismatic and basal systems are perpendicular to the high texture intensity band. Uniaxial stress state results are consistent with the Schmid factor analysis performed by [47] on a similarly textured RX Zry-4. The biaxial stress states limit the maximum GSF and show especially low GSF distributions for prismatic activity. The pyramidal GSF distributions are relatively high for all stress states.

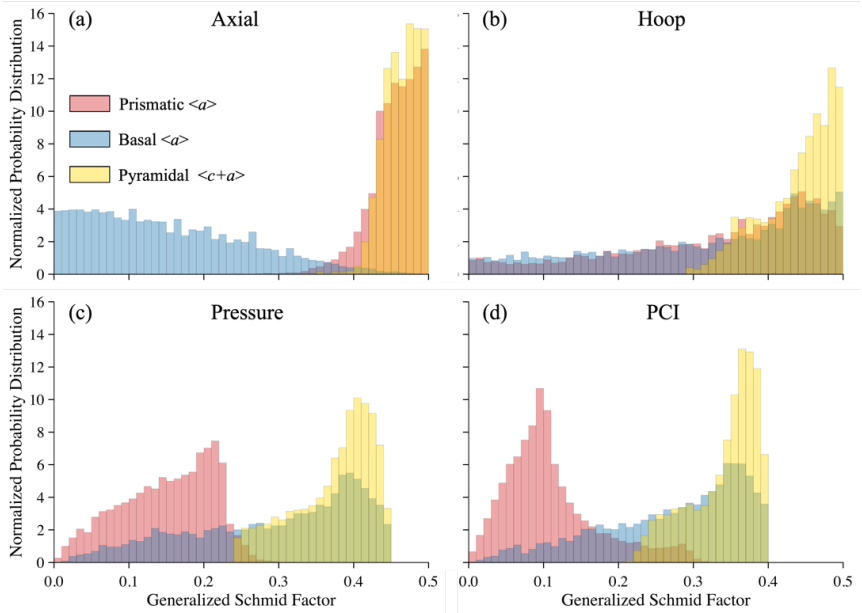

Figure 4-27: Normalized probability distribution of prismatic <a> (red), basal <a> (blue), and pyramidal <c+a> (gold) slip systems for each stress states applied to as-received cladding microstructure.

Figure 4-28 presents estimated active systems for each stress state at test temperatures with the same (00.2) pole figure format as Figure 4-26. Results reflect the GSF distributions in Figure 4-26 compounded with the temperature dependence of slip system CRSS included in Chapter 1 Section 3.2.2. At room temperature, the pyramidal slip system does not achieve CRSS in any stress state which is consistent with literature [39]. Also, the PCI case displays a band ± 50° in the TD and ± 25° in the RD where the stress state does not have sufficient RSS to activate prismatic slip. At 400 °C and particularly for biaxial stress states, more competitive activity is predicted between slip systems, but the axial case retains a band extending across the TD and ± 10° in the RD no basal slip is predicted.

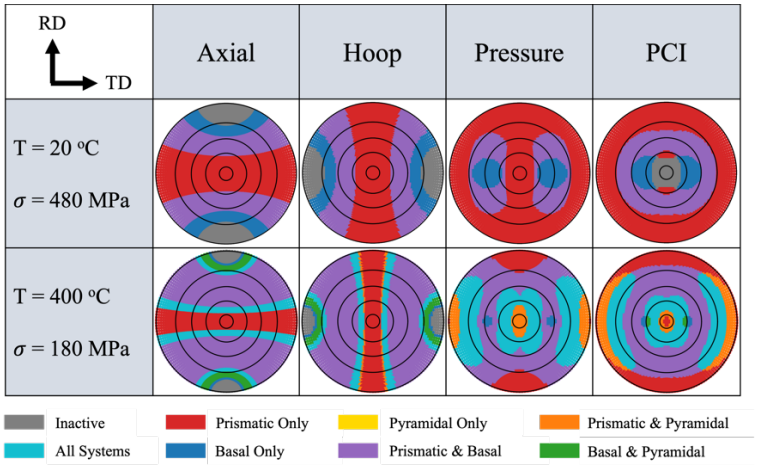

Figure 4-28: Slip systems estimated to be active at yield stress. The (00.2) pole figures are projected on a stereographic Wulff net with reference circles at 10°, 30°, 50°, 70°, 90° from normal.

4.4 Discussion

In this chapter, the effects of stress state and temperature on mechanical anisotropy and microstructure evolution in Zry-4 cladding is studied using axial tension and internal pressure experiments at room and elevated temperatures. The deformation mechanisms controlling the cladding mechanical behavior and microstructure evolution are investigated using the mechanical testing, microstructure characterization, VPSC simulations, and resolved stress analysis results. Results and hypotheses are evaluated with respect to the goals mentioned in Section 4.1 and the Thesis Statement presented in Chapter 2.

4.4.1 Mechanical Behavior

The mechanical testing system demonstrates good repeatability within the expected variance of material properties. The mechanical behavior is consistent with literature results for rolled texture CWSR Zry-4 cladding [21], [45], [51], [60], [61], [141]. The mechanical properties shown in Figure 4-6 - Figure 4-8 and Table 4-3 are also consistent with the results reported in the literature comparison. The decrease in Young's modulus is consistent with the expected 5% drop per 100 °C expected in HCP metals of the Group IV-B row in the periodic table [159]. The Young's modulus measurement at 525 °C from the internal pressure test is low and the cladding displayed

a yield drop softening behavior in which most of the plastic flow occurred below the maximum load. The power-law hardening behavior observed in the PR-RT and high temperature samples and the yield plateau displayed by the AX-RT samples are consistent with the behavior observed in literature [21], [36], [47]. Yield plateaus and especially yield drops indicate a lack of mobile dislocations at yield requiring dislocation production [55]. The AX-RT sample yield plateau is followed by high hardening rate which is also observed by [47] for RD tension.

Figure 4-29 shows the von Mises effective yield stress (σ_{YS}) normalized by the Young's Modulus (E) and plotted against homologous temperature, the fraction of the absolute test temperature (T) over the absolute melting temperature (T_m), to isolate the thermal effect on plastic deformation. There are two distinct regimes: a temperature-dependent (thermal) regime up to $0.25T_m$ and a temperature-independent (athermal) regime above $0.25T_m$. Similar behavior of the normalized YS was observed by [51] for RX Zry-4, with $0.3T_m$ as the transient point describing the shift from thermally activated dislocation behavior to the athermal stress regime. The athermal stress regime appearing in Figure 4-33 extends to lower temperatures compared with that published in [51] for the RX Zry-4. This can plausibly be attributed to higher dislocation density in the CWSR material examined in the current research, increasing yield stress without significantly affecting the Young's modulus, and/or the lower strain rate used in this work ($16.7*10^{-6}$ /s in this work compared to 10^{-3} /s in [51].

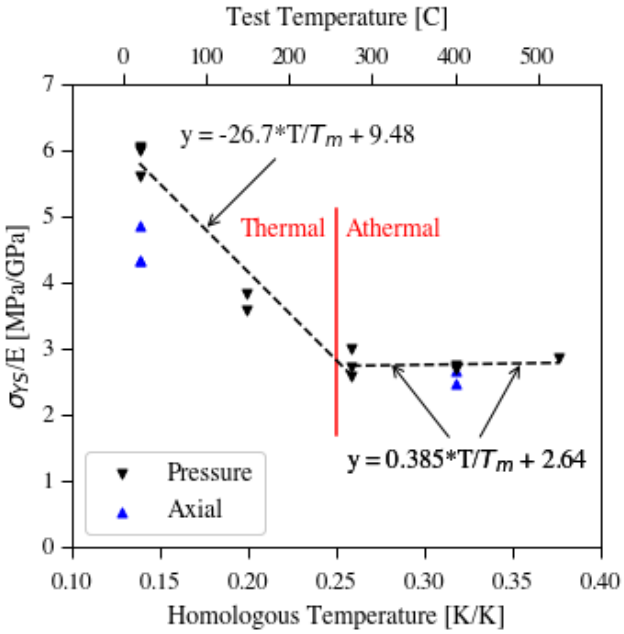

Figure 4-29: Normalized yield strength versus test temperature. T_m(Zry-4) = 1850 °C [32]. Trend lines are from pressure data only.

For the internal pressure stress state, the cladding mechanical behavior begins to change above 275 °C. Measurements of the Young's modulus decrease significantly, the yield stress anisotropy between stress states nearly disappears, plastic strain rates indicate reduced plastic flow anisotropy, and the cladding displays athermal plastic behavior. These provide clues that the deformation mechanisms are changing which are further examined using microstructure characterization and resolved stress analysis in the following sections.

4.4.2 Microstructure

Variables such as sample preparation, interaction volume, and residual strains are some of the important key-role factors affecting the index rate of both characterization methods. Both characterization techniques most successfully resolve RX microstructure where large grains and low misorientation provide the strongest diffraction conditions. The deformed samples retain some of the RX grains, but their area fraction is smaller, and the DAO, lattice strains, and KAM values are higher compared to the pristine sample. The single grain analysis highlights this, revealing significant differences between grains which first appear similar. The DAO measured in single RX grains using 3DXM and EBSD techniques are comparable, demonstrating that these methods are consistent and provide complementary datasets.

The EBSD results indicate that macroscopic plastic deformation is accommodated by microscopic strain gradients leading to grain fragmentation. The pristine sample grain size area fraction in Figure 4-20 slightly shifts towards smaller grains for the deformed samples, suggesting that larger grains fragment into multiple smaller sub-grains upon plastic deformation. The area fraction results of the microstructure categories listed in Table 4-5 support this finding, with a modest increase in sub-grain area indicating a much larger increase in the number of sub-grains. Figure 4-21 uses KAM to highlight misorientation indicative of strain which, at high magnification, display structures defining low misorientation domains.

Orientation gradients and grain fragmentation revealed in the deformation microstructure indicate that plastic spin may be an active deformation mode. Figure 4-30 shows the relationship between these schematically with pristine microstructure which is deformed by an imposed strain (ϵ). The material spin (β) and lattice spin (Ω) are similar in area A, which minimizes the difference between them: the plastic spin. Grains often rotate by a common lattice spin but may be constrained and develop intragranular cells where the lattice spin varies and the plastic spin is high, such as shown in Figure 4-30 (b) area B [90]. Boundaries where intragranular lattice spin is different are shown with dashed lines which are measured as KAM with EBSD characterization.

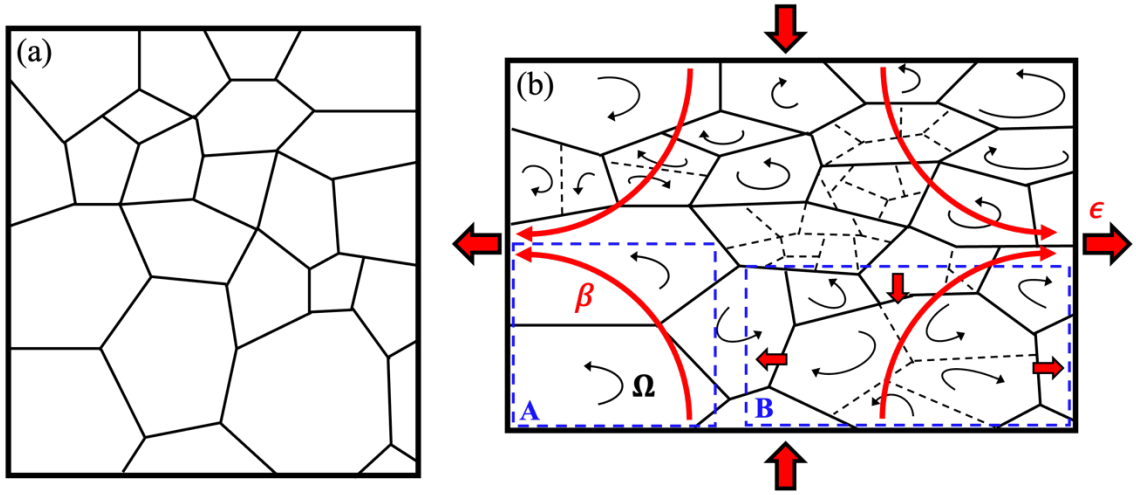

Figure 4-30: Schematic representation of (a) pristine microstructure which is (b) deformed by tension in the horizontal direction. Grain boundaries are shown as solid black lines, orientation gradients are shown with dashed black lines, material spin is shown as red arrows, and lattice spin is shown as black arrows.

The effect of plastic spin, shown in Figure 4-30 (b) area B, is captured experimentally and visualized in Figure 4-31. Figure 4-31 (a) uses KAM to display orientation gradients forming boundaries of varying intragranular lattice spin, (b) displays the disorientation axis from the

average grain orientation to show the relative lattice spin direction, and (c) overlays both to show their relationship. These structures are similar in size and shape to the dislocation cell structures observed with transmission electron microscopy in similarly deformed Zircaloys, which displayed dense dislocation walls surrounding low dislocation density domains [38], [61], [160].

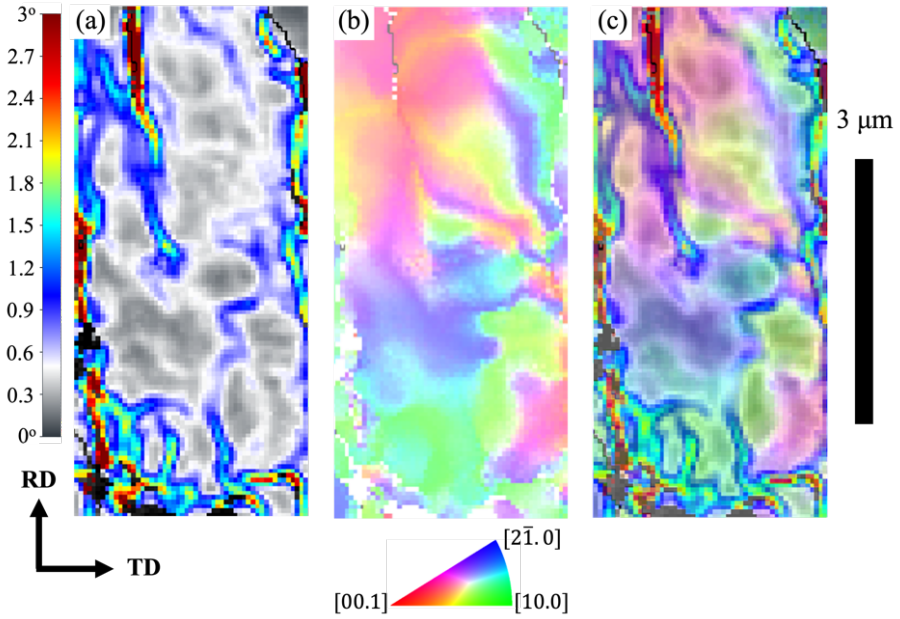

Figure 4-31: Micrographs of a grain from the biaxial-deformed sample at high magnification (7500x). (a) A KAM micrograph highlighting orientation gradients, (b) the disorientation axis from the average grain orientation defined using ND||IPF coloring, and (c) the disorientation axis micrograph superimposed with 66% transparency on the KAM micrograph to show their relationship.

The relationship between lattice spin and deformation-induced texture development shown in Figure 4-23 is clarified by experimental and VPSC simulation results of texture development from Xu et al. [161] for a similarly textured Zry-2 shown in Figure 4-32, so no texture evolution simulations are performed in the present study. Xu et al. [161] show that tensile strains in the RD and TD produce {10.0} fibers in the axis of high tensile stress and plastic strain. The plastic strain ratios in Table 4-3 show that axial tension loading produces a high plastic strain rate in the RD, whereas internal pressure loading produces a high plastic strain rate in the TD. Consequently, axial tension loading develops uRX microstructure with a {10.0} fiber in the RD, increasing the similar uRX texture from pilgering. Conversely, internal pressure loading develops uRX microstructure with {2$\bar{1}$. 0} fiber in the RD, which differs from the pilgering uRX texture and decreases the texture intensity. The differences in textures are small, but the trends agree with the results of [161]. An analysis of Schmid factors reveals no difference between {10.0} and {2$\bar{1}$. 0} RD fibers associated with the pilgered uRX and RX microstructures that might affect the differences in misorientation observed between the biaxial-deformed or uniaxial-deformed samples.

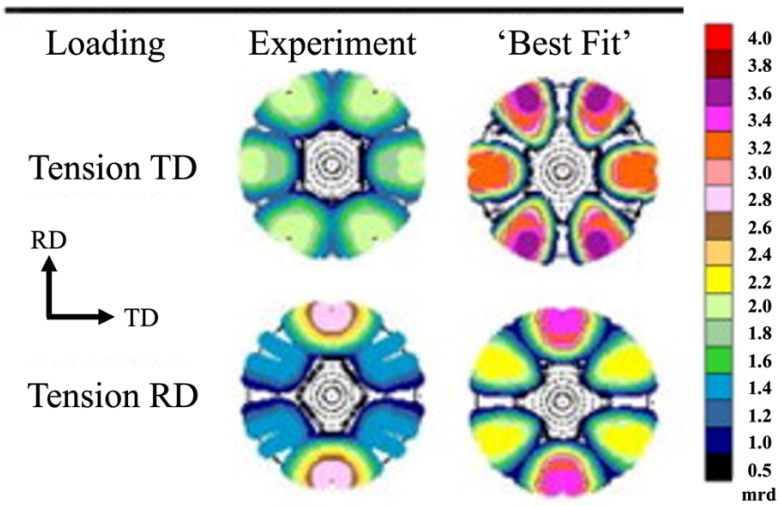

Figure 4-32: Comparison of experimental and VPSC simulated {10.0} pole figures. Modified from [161].

Plausibly, the dislocation cells present in uRX microstructure suggest that the dislocation density reaches the threshold required for dynamic recovery to balance dislocation nucleation and annihilation during deformation [160]. Considering this, dynamic recovery can account for the similarities between pristine and deformed uRX microstructure data in Figure 4-22 (c) and (f), suggesting a similar threshold for static recovery during the CWSR annealing. In contrast, dislocation nucleation exceeds annihilation in the RX microstructure, as shown by clear differences between the pristine and deformed samples in Figure 4-22 (b) and (e). Evidence of dynamic recovery with a similar threshold to static recovery suggests that, in samples deformed *via* internal pressurization, the increased uRX fraction does affect relaxation while the higher misorientation in the RX fraction could relaxation according to Hypothesis 2 from Chapter 2. To provide stronger confirmation that this effect results from the plastic strain ratios instead of increased hardening, samples with different strains are used in the present work. The results indicate that internal pressure loading accelerates the misorientation accumulated in RX microstructure, and differences in the RD, TD, and ND strain rates between loading modes are analyzed to better understand this phenomenon.

The VPSC simulations show that the plastic spin results of the internal pressure and axial tension velocity tensors are consistent with the increased misorientation observed in the biaxial-deformed sample microstructure. Bunge & Nielsen [90] performed extensive mechanical testing and texture analysis, revealing that the plastic spin is minimized when the symmetry of imposed deformation is parallel to the symmetry of the initial texture and is highest when deformation is imposed at the "most asymmetric" tensile directions. In this study, axial loading is colinear with the symmetric RD axis and simulations predict the least plastic spin. The uniaxial-TD simulations predict slightly higher plastic spin indicating that results are sensitive the loading orientation with respect to the texture symmetry independently of uniaxial versus biaxial loading. Internal pressure loading imposes biaxial loads in the RD and TD and the simulation predicts the highest plastic spin, indicating that biaxial loading is the least symmetric. The texture evolution discussed in the previous paragraph reflects the differences in plastic spin, and the resulting misorientation. Specifically, the material spin more closely matches the lattice spin for the axial tension mode compared to the internal pressure mode, thereby reducing the plastic spin.

4.4.3 Mechanical Anisotropy

The linear plastic strain rates, obtained in the current research and shown in Figure 4-4 and Table 4-3, suggest that deformation mechanisms remain consistent even at relatively high strains and the hardening effects do not alter the macroscopic plastic flow behavior. As noted in Section 4.3.1, mechanical anisotropy is observed in the plastic strain rates. To quantify this effect, Wang & Murty [58] defined mechanical anisotropy constants, R & P, as the unloaded strain ratios from uniaxial tensile tests along the RD and TD, respectively. The results of their uniaxial quasi-static tensile tests using CWSR rolled-texture Zry-4 plates are summarized in Figure 4-33. It was found that the temperature has no significant effects on the mechanical anisotropy if loading is along the RD direction. Conversely, a drastic decrease in the mechanical anisotropy is observed above 300 ºC (e.g., greater isotropic behavior at elevated temperatures), if loading is along the TD.

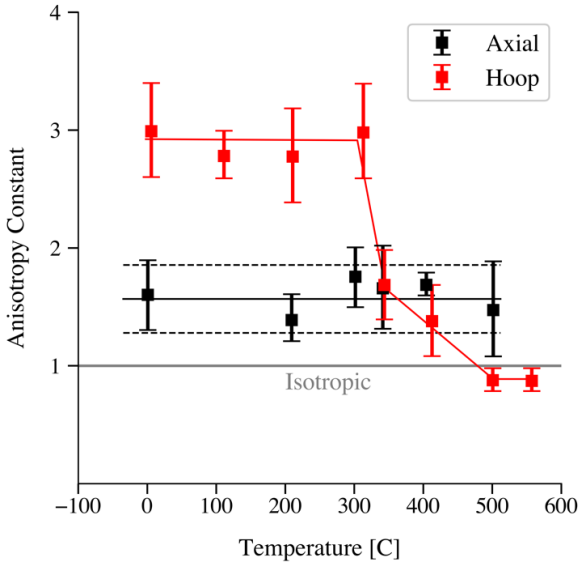

Figure 4-33: Thermal dependence of textured Zry-4 mechanical anisotropy from uniaxial testing. Modified with permission from [58]. R and P are the unloaded strain ratios from uniaxial tensile tests along the RD and TD, respectively, describing the anisotropy.

The R-factors calculated and used in [134] are 3.0 and 3.2 respectively. The pilgered CWSR Zry-4 cladding tube samples display notably higher anisotropy than that of the rolled Zry-4 plate samples shown in Figure 4-33, but R remains essentially constant at both temperatures indicating temperature independent anisotropy. The plastic strain data from internal pressure loading obtained in the current study cannot be used to quantify anisotropy through the anisotropy constants, R or P. However, [18] use the plastic strain rates and Hill yield coefficients to characterize anisotropy, revealing high anisotropy up to 275 ºC which is significantly reduced at 400 ºC. This suggests that the internal pressure stress state undergoes thermal activation that increases isotropic behavior similar to the hoop stress state.

The GSF analysis carried out in in Section 4.3.4 aids in understanding mechanical anisotropy behavior with temperature under various stress states. High RSS applied to a slip system characterized by low CRSS, such as the axial stress state applied to the prismatic <*a*> system in Zr shown in Figure 4-27, can cause the slip system to be the primary deformation mode. Overall, when a single slip system is dominant, the anisotropy remains relatively insensitive to temperature,

as the glide planes accommodating strain remain consistent over a wide temperature range. Conversely, temperature-dependent mechanical anisotropy is observed in cases of competitive slip system activity. This is attributed to the significant thermal effects changing the CRSS ratios discussed in Chapter 1 Section 3.2.2, resulting in changes to relative slip activity.

The slip system activities illustrated in Figure 4-28 indicate that pyramidal <*c*+*a*> slip is thermally activated. However, this slip system is required under most conditions to accommodate strain with a *c*-component, following the von Mises criterion for compatible deformation [36], [86]. Despite the consistently low but present activity of pyramidal <*c*+*a*> slip, it is primarily the competition between the prismatic and basal slip systems that influences the temperature dependence of mechanical anisotropy.

In the axial stress state, there is low RSS for basal <*a*> slip but high RSS on prismatic <*a*> slip systems throughout the microstructure. This results in dominant prismatic slip activity and a temperature independent anisotropy factor (R). In the hoop stress state, similar prismatic and basal <a> RSS is observed throughout the microstructure, indicating competitive slip system activity, particularly as the CRSS difference between the systems diminishes at higher temperatures. The basal slip system is activated above 300 ºC and close competition of multiple slip systems on perpendicular glide planes increases the isotropic mechanical behavior until the temperature surpasses 500 ºC and the Zry-4 becomes isotropic for the hoop stress state (P).

Recent findings from discrete dislocation dynamics (DDD) modeling, as reported by Li et al. [111], offer valuable insights into the intricate interdependence of prismatic and basal slip in Zr under various stress states and temperatures. At elevated temperatures, the basal-prismatic cross-slip plays a significant role in dislocation dynamics. The presence or absence of basal <*a*> dislocations nucleating during deformation has strong implications for dislocation-controlled deformation mechanisms [111]. The DDD results align with experimental findings that demonstrate the thermal activation of basal-prismatic cross-slip within the temperature range of 300-500 ºC [18], [58], [111], [162]. Additionally, the DDD model shows that basal <*a*> activity intensifies with temperature in stress states where the basal <*a*> Schmid factor surpasses that of the prismatic <*a*> systems [111]. Applied across a monocrystal in a simulation or a heavily textured polycrystal, these results support the hypothesis that mechanical anisotropy decreases between 300-500 ºC for the hoop stress state due to increasingly competitive prismatic <*a*> and basal <*a*> slip.

Figure 4-27 shows that the biaxial stress states produce higher GSF on basal <*a*> systems than prismatic <*a*> systems in the microstructure. However, in the biaxial stress states, the slip activity of these systems is more competitive than the axial stress state. This is attributed to the prismatic <*a*> slip system having a lower CRSS than the basal <*a*> slip system, thereby reducing the GSF required for prismatic slip activation. Consequently, the pressure and PCI stress states induce competitive slip activity between basal and prismatic systems, resulting in increased mechanical isotropy above 300 ºC, as documented in [18].

4.5 Conclusions

Conclusions from this chapter and how they relate to the goals and hypotheses of this dissertation are summarized below and discussed further in Chapter 6.

- Measured mechanical behavior and material constants are comparable with literature which validates the mechanical testing methods used in this dissertation.

- Higher yield stresses and stress accumulation are observed for internal pressure testing compared to axial tension testing at room temperature, but these effects disappear at 400 °C. This provides limited evidence supporting Hypothesis 1, but stress relaxation testing in Chapter 5 contributes a more direct and definitive evaluation of this hypothesis.
- Deformation increases intragranular misorientation in RX microstructure while dislocation production exceeds annihilation.
- High misorientation associated with uRX microstructure is limited by dynamic recovery which form structures that appear to be dislocation cells formed by plastic spin. Further deformation increases cell misorientation until they are classified as sub-grains.
- Residual uRX microstructure from pilgering and deformation induced uRX microstructure are similar, indicating that static recovery during annealing has a similar limit to dynamic recovery during deformation at 400 °C.
- Internal pressure loading produces high plastic spin compared to uniaxial loading along the RD. Under the current conditions, Consequently, the biaxial-deformed sample displays increased deformation microstructure at lower imposed strain compared to the uniaxial-deformed sample, providing evidence supporting Hypothesis 2.
- Strain from uniaxial tension in the RD produces a {10.0} texture fiber in the RD like uRX microstructure from pilgering, increasing the uRX fiber intensity. Strain from internal pressurize produces a $\{2\bar{1}.0\}$ texture fiber in the RD, reducing the uRX fiber intensity.
- The cladding texture produces significant differences in RSS distribution from varying stress states, producing dominant prismatic <*a*> slip from axial tension but more competitive slip activity for prismatic <*a*> and basal <*a*> systems from internal pressure loading. This helps explain the temperature and stress state dependence of mechanical anisotropy and confirms Hypothesis 3.

Chapter 5 Study of Viscoplastic Deformation

5.1 Introduction

The study of viscoplastic deformation is used to evaluate the Thesis Statement of this dissertation through experiments that support or disprove Hypothesis 4 made in Chapter 2. Time-dependent deformation mechanisms are more complex and less studied than time-independent mechanisms, and creep is the better characterized viscoplastic deformation mode. These factors limit the availability of context and validation from literature review but increase the novelty and impact of this work. The findings of Chapter 4 help narrow the scope of this chapter and provides required context to reveal the active anisotropic mechanisms affecting the stress relaxation behavior.

The effect of mechanical anisotropy on stress relaxation behavior is investigated by comparing the mechanical response of CWSR Zry-4 cladding to axial tension versus internal pressure loading. Three levels of equivalent strain are achieved during loading and held during relaxation at 300 oC. Relaxation behavior with comparable microstructures is measured by loading samples to 0.25% equivalent strain ensuring samples do not yield or produce significant defects. Relaxation behavior with plastic deformation at NRC limits for cladding strain during operation [3] is measured by loading samples to 1% uniform strain, resulting in comparable initial stress energies. The effect of increased stress and dislocation density is investigated by loading samples to 2% equivalent strain, providing an upper limit to stress relaxation behavior expected during operational PCI events. Samples are characterized using EBSD without deformation, after loading to 2% equivalent strain, and relaxed from 2% equivalent strain using both loading modes. A thermo-mechanical simulation of a PCI is performed and the Zry-4 viscoplastic material model is compared to experimental results.

First, the stress relaxation behavior of the cladding is measured to test Hypothesis 4, employing methodology capable of testing Hypotheses 1 and 3. Second, microstructure characterization of pristine, deformed, and deformed-then-relaxed samples is performed to investigate the microstructure evolution, evaluate Hypothesis 2, and relate results to Chapter 4. Third, a thermo-mechanical fuel performance simulation is performed to provide context between experimental results, reactor conditions, and the material model performance.

This chapter contains work from the following article:

- *'Enhanced Stress Relaxation Behavior via Basal <a> Activity from Internal Pressure Loading in Zircaloy-4 Cladding'* [163]

5.2 Methods

5.2.1 Experimental

Five full-tube axial tension tests and six internal pressure tests are conducted according to the procedures described in Chapter 3 Sections 1.2 and 2.1. The stress relaxation tests load samples with a monotonic strain rate to achieve the nominal strain which is held constant for the relaxation period as shown in Figure 5-1. For each loading mode, one test is terminated after reaching 2% equivalent strain to produce deformed samples for characterization. Three internal pressure stress relaxation tests imposing 2% equivalent strain are performed to verify experiment repeatability. All tests are performed at 300 °C during loading and relaxation. Sample names and testing parameters are included in Table 5-1.

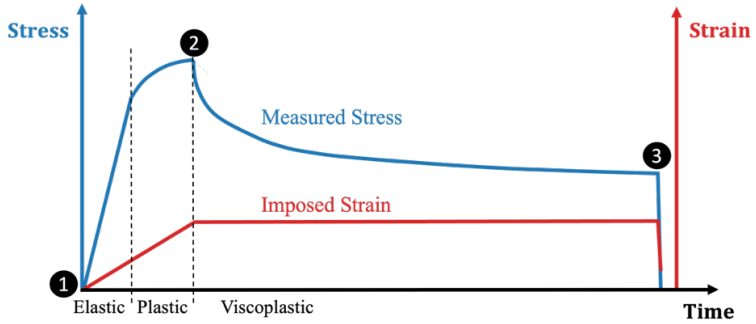

Figure 5-1: Schematic of stress relaxation test separated by dashed lines into periods where elastic, plastic, and viscoplastic deformation modes dictate the stress-strain relationship. Numbered dots indicate points throughout loading where samples are characterized.

An axial tension stress relaxation test imposing 1 % equivalent strain is performed to investigate whether the stress oscillations discussed in Chapter 3 Section 1.2.2 affect relaxation results. Stress oscillations during pressure relaxation tests are characterized as a sin wave function using Equation 5-1 where S is the average stress, A is the stress amplitude, f is the oscillation frequency, and t is time. Oscillation data are shown in Figure 5-2 and the oscillation amplitude is determined to be 5 MPa with a frequency of 1/20 s. However, relaxation tests are strain actuated, so the strain is oscillated around 1% average equivalent strain. The desired stress amplitude is divided by the Young's modulus resulting in 67×10^{-6} [mm/mm] strain oscillation amplitude.

$$\sigma = S + A \cdot sin(2\pi \cdot f \cdot t) \qquad \text{Equation 5-1}$$

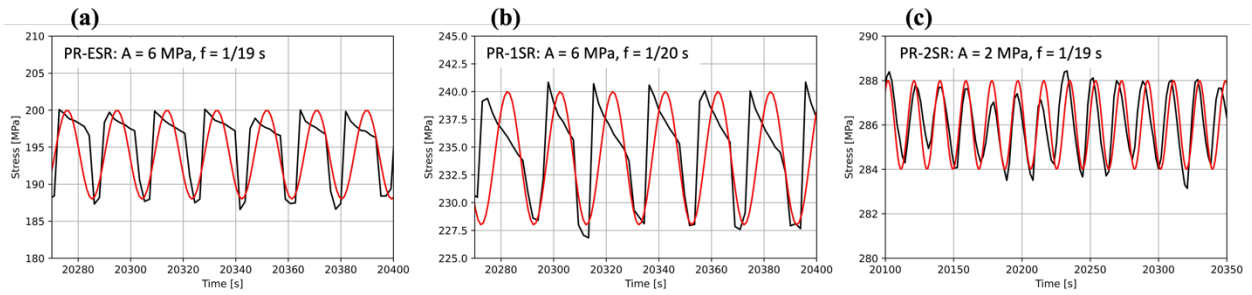

Figure 5-2: Characterization of pressure oscillations from three stress relaxation tests. (a) PR-ESR, (b) PR-1SR, (c) PR-2SR.

Microstructure characterization is performed on samples in the reference state (REF), deformed state (DF), and deformed and stress relaxed state (SR) corresponding to dots (1), (2), (3) in Figure 5-1 to measure the microstructure evolution. The samples deformed to 2% equivalent strain are chosen for characterization including both deformation states (DF and SR) and both loading modes (axial and pressure) which are quickly cooled and removed from the furnace after unloading to preserve microstructure. Characterization methods for each sample are shown in Table 5-1. Samples are characterized using SEM-EBSD according to the procedures described in Chapter 3 Sections 1.4 and 2.2.

Table 5-1: Experimental parameters for all samples loaded in the study of viscoplasticity

Sample ID	Loading Mode	Target Equiv. Strain [%]	Relaxation Period [hr]	EBSD Characterization
REF	None	0	n/a	Yes
AX-ESR	Axial Stress Relax.	0.25	8	No
AX-1SR	Axial Stress Relax.	1	8	No
AX-1SR-O	Axial Stress Relax. with Oscillations	1	8	No
AX-2DF	Axial Deformed-only	2	0	Yes
AX-2SR	Axial Stress Relax.	2	8	Yes
PR-ESR	Pressure Stress Relax.	0.25	8	No
PR-1SR	Pressure Stress Relax.	1	8	No
PR-2DF	Pressure Deformed-only	2	0	Yes
PR-2SR	Pressure Stress Relax.	2	8	Yes
PR-2SR-6	Pressure Stress Relax.	2	6	No
PR-2SR-10	Pressure Stress Relax.	2	10	No

5.2.2 Data Analysis

Results of stress relaxation mechanical testing are simplified to a representative effective stress versus time curve by appending the stress at the start of the relaxation period and then at regular intervals. Higher point density is used at the beginning when stress relaxation is more dynamic. Normalized relaxation curves are determined by dividing each value by the initial stress. The extent of stress relaxation over a consistent time period, here eight hours, is determined using stress relaxation ability (SRA), as defined in Equation 5-2 [117]. The viscoplastic strain rate is calculated according to Equation 1-7 using the relationships discussed in Chapter 1 Section 3.2.3. The average Young's modulus (E) of all axial and pressure stress relaxation tests is used to determine the viscoplastic strain rates. The relationship between stress and strain rate are defined using a power law relationship according to Equation 5-4 [99]. Here, A represents the equivalent global strain rate for unit stress, and σ_1 (1MPa) is the unit stress [99].

$$SRA = \frac{\sigma_{initial} - \sigma_{final}}{\sigma_{initial}}$$ Equation 5-2

$$\dot{\epsilon}_{vp} = -\frac{d\sigma}{E}\frac{1}{dt}$$ Equation 5-3

$$\dot{\epsilon}_{vp} = A\left(\frac{\sigma}{\sigma_1}\right)^n$$ Equation 5-4

An activation volume analysis is performed according to Equation 5-5 and Equation 5-6 [50], [98], [112]. Here, $\Delta\sigma$ is the change in applied effective stress, M is the Taylor factor, k is the Boltzmann constant, T is the absolute temperature, t is time, and t_o is the time constant which varies to provide the best fit parameters. V^* is the apparent activation volume, V is the true activation volume, and τ is the applied shear stress ($M = \sigma/\tau$) [50], [98], [112].

$$\Delta\sigma = \left(\frac{MkT}{V^*}\right)\ln\left(1 + \frac{t}{t_o}\right)$$ Equation 5-5

$$V = V^* - \frac{2kT}{\tau}$$ Equation 5-6

Resulting activation volumes are presented using the Burgers vector, $b = \frac{1}{3} < 11\bar{2}0 > = a$, as the length unit corresponding to basal <*a*> and prismatic type I <*a*> deformation mechanisms to remain consistent with literature [50], [51], [88], [104], [109], [110], [164], [165]. The Taylor factor for rolled texture Zry-4 is commonly simplified to 4 which is used for analysis results to remain consistent with literature results [50], [51], [104]. However, Taylor factors are also calculated for this cladding using the crystal plasticity function of the ATEX software package by [132], v. 4.12. The velocity tensor is defined independently for axial and pressure testing using measured plastic strain rates, the microstructure is defined using EBSD results of the pristine cladding, and Zry-4 CRSS values are calculated at 300 °C for prismatic type 1 <*a*> slip, basal <*a*> slip, and pyramidal type 1 <*c* + *a*> slip according to equations published by [34], [35] which are provided in Chapter 1 Section 3.2.2. The stress exponents and activation volume constants are calculated using least-mean-square error regression.

5.2.3 Thermo-Mechanical Simulation

The thermo-mechanical analysis is performed using finite element methods (FEM) in the BISON nuclear fuel performance code to quantify imposed strain and stress evolution and evaluate the stress state within the fuel cladding during a PCI resulting from a power ramp. A 2D-RZ axisymmetric analysis is performed using the discrete PWR fuel rod mesh shown in Figure 5-3 which simulates a fuel rod with 10 UO_2 pellets in He cover gas with typical PWR boundary conditions such as coolant pressure, temperature, and heat transfer coefficients. Nuclear heating, burnup, fission product accumulation, and swelling are simulated using the power history and peaking factors defined from a neutronics-coupled simulation which is shown in Chapter 8 Section

6. Fuel pellet thermal expansion is modelled using the coefficient from the MATPRO model [166]. Contact between the pellet and cladding is of particular interest so a Coulomb friction model is used with an augmented Lagrange convergence formulation. The friction coefficient is 0.2 and the normalized penetration penalty is 69 GPa, near the Young's modulus at elevated temperature.

The LHGR is ramped to 20 kW/m over one week and then held for 450 effective full-power days (EFPD) (18.8 GWd/MTU) to allow the FCG to close. Then the LHGR is increased to 60 kW/m over 10 minutes and held for one week to produce a PCI and evaluate the material response. The rod power generation rate increase from 20 to 60 kW/m is larger than expected in operation but helps provide context between a PCI event in reactor conditions and the materials characterization performed in the present work. Three material models provide the mechanical properties of the cladding for the simulation: elastic, plastic, and viscoplastic. The elastic model uses isotropic elastic constants from [167], the plastic model is from [140], and the viscoplastic model incorporates thermal and irradiation creep from [168] and [169], respectively. Input file blocks describing simulation parameters in more detail are included in Chapter 8 Section 6.

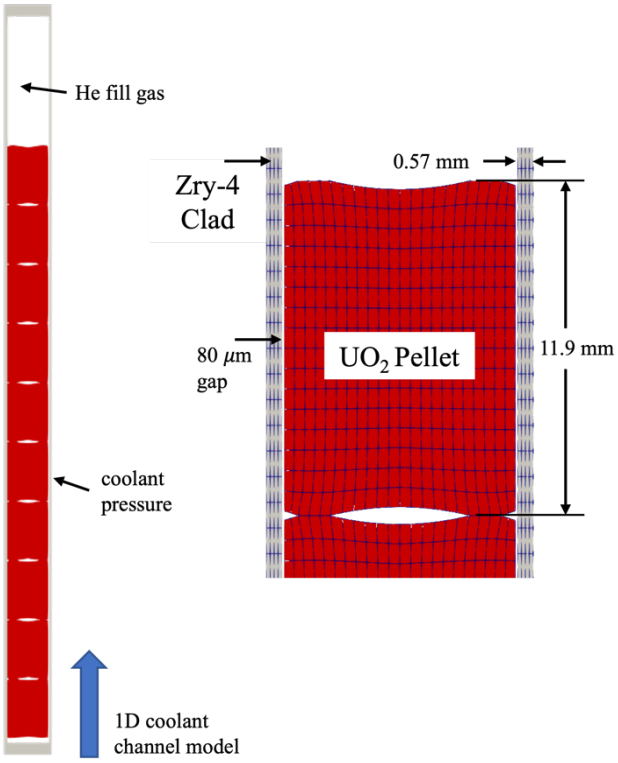

Figure 5-3: Fuel rod mesh used in FEM analysis.

The simulated results from the viscoplastic FEM material model, in this case the thermal creep model from [168], are compared to the results of stress relaxation testing to evaluate the model accuracy. The FEM viscoplastic model is exclusively a creep model that calculates a creep strain rate based on the applied effective stress and temperature. After the viscoplastic strain rate is calculated by the material model and multiplied by the time interval, the increase in viscoplastic strain determines the decrease in elastic strain and subsequently, stress. This calculation of stress relaxation from viscoplastic strain rates operates in the opposite order as the experimental results but according to the same Equation 1-7.

5.3 Results

5.3.1 Mechanical Testing

Recorded measurements including time, axial and transverse strain, and applied loads are presented in Figure 5-4 for both axial and pressure loading experiments. Figure 5-5 provides the engineering stress versus strain with the linear regression used to calculate the elastic constants for the AX-ESR and PR-ESR samples, showing these samples do not yield. The data are used to determine true stresses and strains from which the von Mises effective stress and equivalent plastic strains are calculated. This approach enables a direct comparison between the outcomes of uniaxial and multiaxial loading conditions [131]. The mechanical energy balance discussed in Chapter 2 Section 3.2.2 is shown in Figure 5-6, though defect energy cannot be decomposed from the dissipated energy.

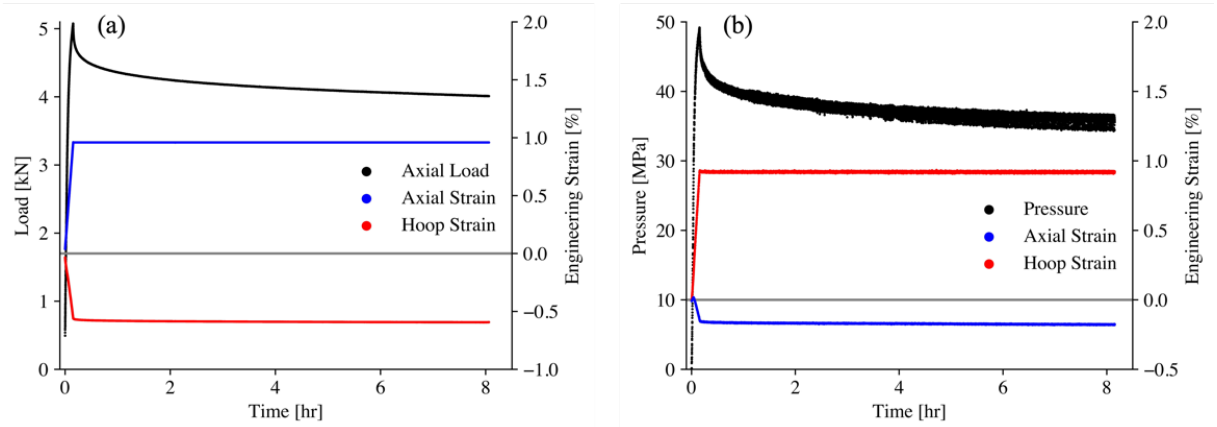

Figure 5-4: Representative experimental data measured during mechanical testing. Data shown for 1% equivalent strain samples tested at 300 °C using (a) axial tension and (b) internal pressure loading.

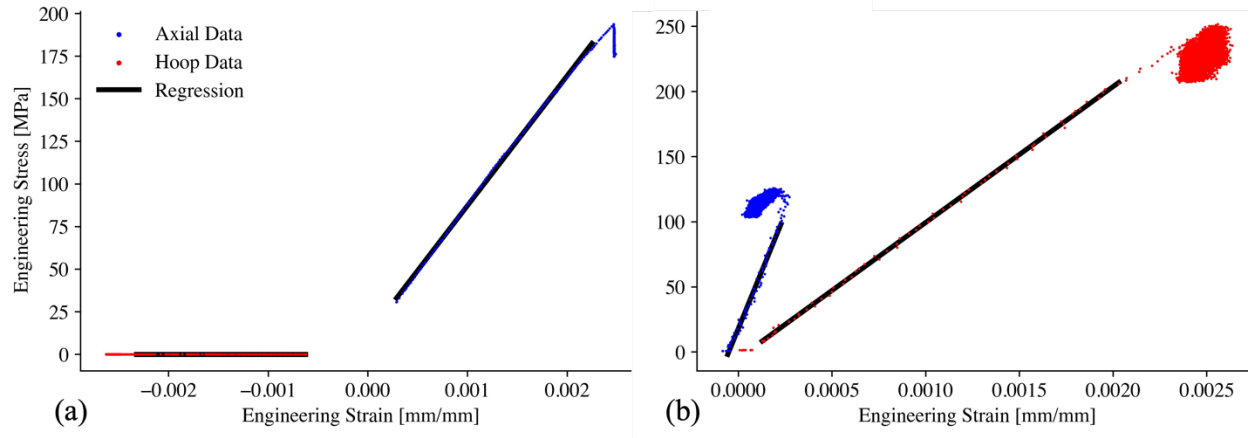

Figure 5-5: Linear regression of the engineering stresses and strains measured for (a) AX-ESR and (b) PR-ESR samples.

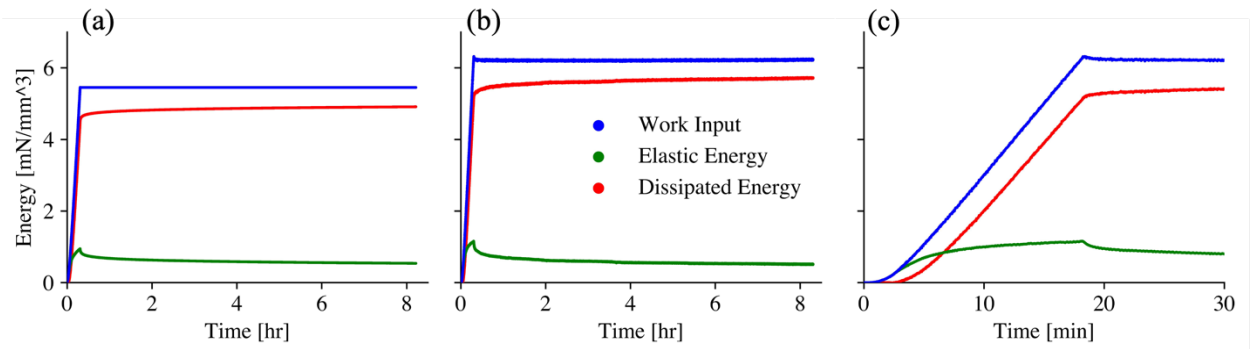

Figure 5-6: Energy balance for (a) AX-2SR, (b) PR-2SR, and (c) a 30 minute subset of PR-2SR showing the transient energy decomposition.

Simplified stress relaxation curves for three samples tested with the pressure loading mode to 2% strain are shown in Figure 5-7, each starting from distinct initial stresses upon loading to the same equivalent strain. Despite the different initial stresses at 2% strain, the normalized stress relaxation behavior across these tests displays remarkable consistency. The results of these mechanical tests including Young's modulus (E), effective yield stress (σ_{yield}), and initial effective stress before relaxation ($\sigma_{initial}$) are summarized in Table 5-2.

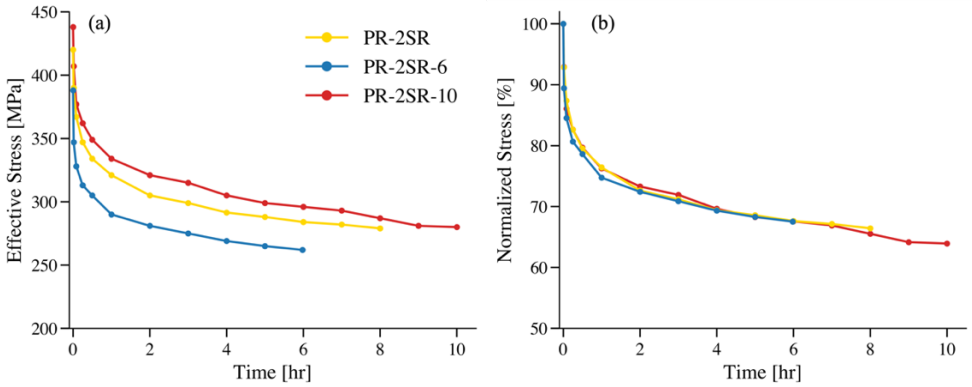

Figure 5-7: Stress relaxation responses of three cladding samples loaded using the same test parameters shown in Table 4-1. (a) Measured effective stress response and (b) normalized effective stress response.

Figure 5-8 illustrates the stress relaxation behavior under axial tension and internal pressure for different imposed strains. For each imposed equivalent strain, specimens loaded using internal pressure exhibit enhanced stress relaxation compared to those loaded using axial tension, an effect that amplifies with increasing strain levels. Mechanical anisotropy and variance are observed in yield and hardening behavior of the CWSR cladding, even between samples cut from the same piece of cladding and those shown in Figure 5-7 that are tested with the same loading parameters. In the elastic case, the relatively small relaxation is not enough to allow the PR-ESR sample to relax to a lower final stress than the AX-ESR sample in eight hours. However, the samples loaded to 1% and 2% strain (-1SR, -2SR) with initial stress differences of 1.3% and 13%, respectively, the enhanced relaxation behavior for internal pressure loading allows the PR-1SR and PR-2SR samples to achieve lower final effective stresses than the corresponding AX-1SR and AX-2SR samples. Viscoplastic strain rates for samples loaded below yield are approximately an order of magnitude lower than those loaded beyond yield as shown in Figure 5-8 (d).

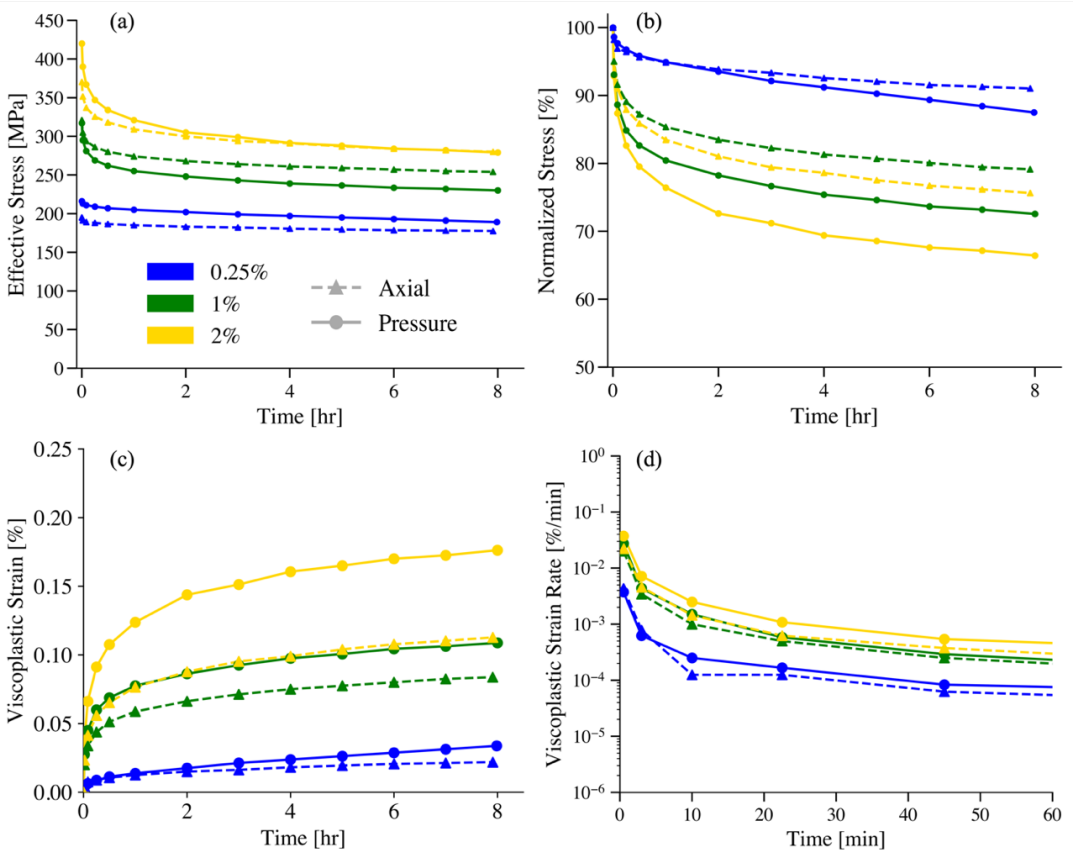

Figure 5-8: Relaxation behavior of samples relaxed at 300 °C for 8 hours. (a) Effective stress relaxation and (b) normalized stress relaxation. (c) Total viscoplastic strain and (d) viscoplastic strain rate in the first hour.

The samples loaded below yield at 0.25% equivalent strain (-ESR) display similar stress relaxation behavior below two hours but then diverge. The -1SR and -2SR samples display more distinct differences between axial and pressure relaxation behavior throughout the entire test period. The pressure samples relax faster than the corresponding axial samples and achieve higher 8-hour SRAs. This increased relaxation occurs independently of initial effective stresses which are similar for -1SR stress states. Further, repeated testing with PR-2SR parameters shown in Figure 5-7 result in up to 12% difference in initial stress without changing the stress relaxation behavior. These results indicate that the effective stress alone does not accurately predict the SRA and, while stress affects the stress relaxation rates, other differences between axial and pressure stress states are responsible for the differing stress relaxation behavior.

The SRA over eight hours increases with higher equivalent strains, demonstrating a correlation with the equivalent plastic strain through power-law relationships, as depicted in Figure 5-9 (a). Although the power law function exponents remain consistent for axial and pressure loading, the proportional coefficient for internal pressure loading is found to be more than 35% higher than that for axial tension loading. Figure 5-9 (b) displays the dependence of viscoplastic strain rate on stress, illustrating how the stress exponent (n) from Equation 5-4 determines the slope of the linear relationships on the log-log plot. As summarized in Table 5-2, these stress exponents decrease as the applied strain increases, and are slightly higher for samples subjected to axial loading.

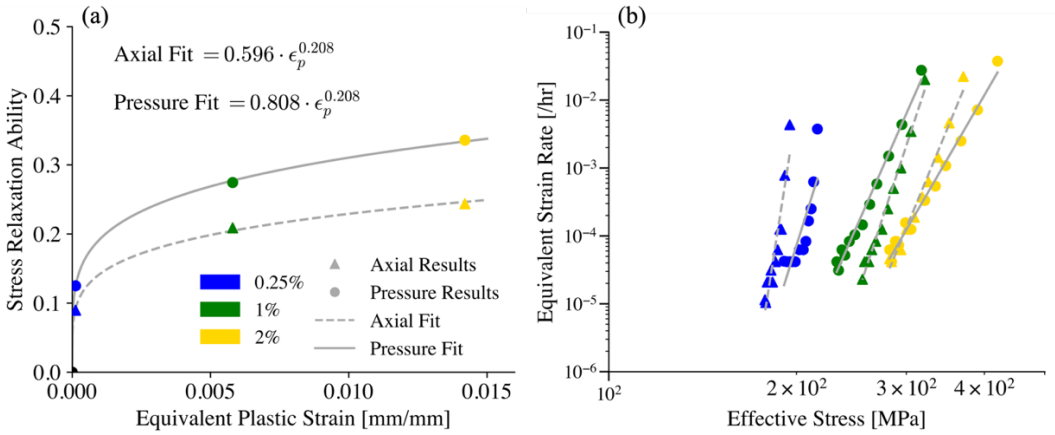

Figure 5-9: (a) SRA versus equivalent plastic strain for samples relaxed for 8 hours. (b) Viscoplastic strain rate versus effective stress using log-log axes.

Results of the axial oscillation stress relaxation test are shown in Figure 5-10 and Figure 5-11. The AX-1SR-O sample accumulated more stress during loading than the corresponding AX-1SR sample, but the normalized stress relaxation behavior, SRA, and activation volumes are similar. Thus, the oscillations applied to the AX-1SR-O sample did not meaningfully affect or increase the stress relaxation behavior.

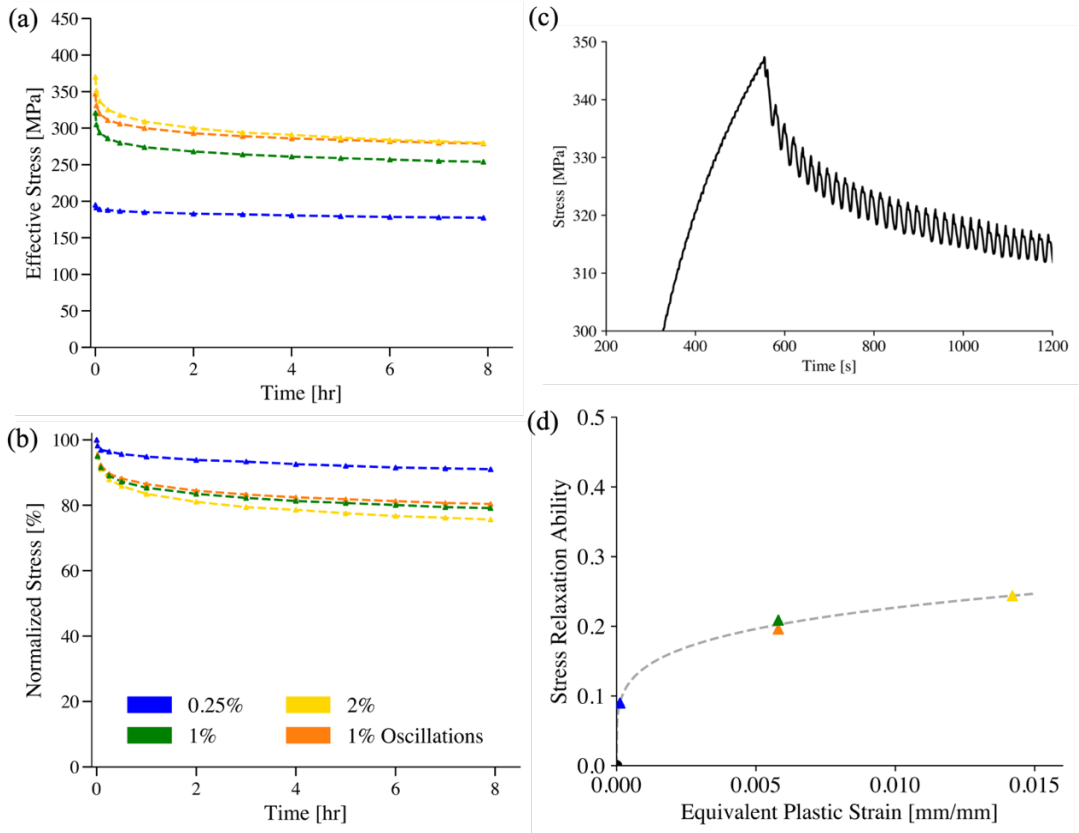

Figure 5-10: Axial oscillation stress relaxation test including other axial samples for comparison.

The activation volumes are plotted against initial stress in Figure 5-11 along with the best fit regression results using parameters listed in Table 5-2. Consistent with literature [50], [88], [105], activation volumes decrease with increasing initial stress. However, the PR1-SR sample displays an activation volume that is 21% lower than the AX1-SR sample with a stress that is 1.2% lower, while the AX1-SR-O displays an activation volume that is 1.0% lower than the AX1-SR sample with an initial stress that is 8.1% higher. This indicates that the activation volume is more sensitive to the stress state than the stress magnitude. The calculated Taylor factors for both loading methods are near 2.5 with similar distributions indicating that the Taylor factor does not cause the differences in activation volume between axial and pressure samples. Using M = 2.5 instead of the commonly accepted value of 4 results in a proportional decrease in activation volumes reported in Table 5-2 by 37.5%. Mechanical testing results of all samples are included in Table 5-2.

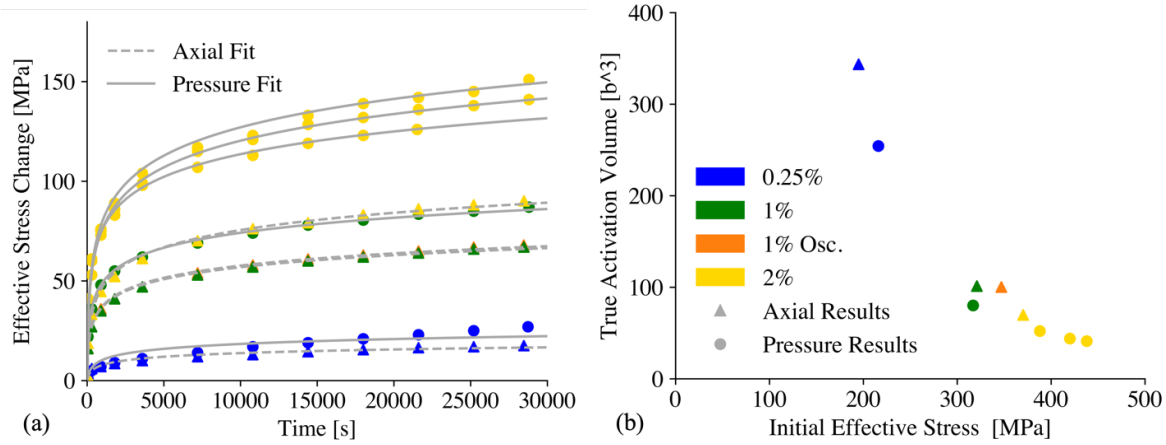

Figure 5-11: Results of activation volume analysis for all stress relaxation tests at 300 °C. (a) Activation volume versus initial stress and (b) best fit regression results shown with measured data.

Table 5-2: Mechanical testing results summary for all stress relaxation tests performed at 300 °C.

Sample ID	E [GPa]	σ_{yield} [MPa]	$\sigma_{initial}$ [MPa]	8-hr SRA [%]	n	t_o [s]	V [b^3]
AX-ESR	76.2	-	195	8.97	58.7	56	343
AX-1SR	72.8	197	321	20.9	28.0	15	101
AX-1SR-O	64.6	226	347	19.6	29.9	15	100.
AX-2SR	72.6	213	370.	24.4	22.2	24	69.8
PR-ESR	84.5	-	216	12.5	29.3	58	254
PR-1SR	85.7	213	317	27.4	20.9	11	80.1
PR-2SR	88.4	241	420.	33.6	15.8	20	43.9
PR-2SR-6	86.2	217	388	-	17.4	10	52.1
PR-2SR-10	85.1	319	438	34.5	14.7	21	41.2

5.3.2 Microstructure Characterization

The texture and microstructure of the characterized cladding samples are shown in Figure 5-12 displaying typical CWSR microstructure and basal texture that appears consistent with results reported in Chapter 4 Section 3.2.2. The cladding microstructure evolution from the pristine state, through loading to 2% equivalent strain, to the stress-relaxed state is presented in Figure 5-12 (b)-(f) using ND||IPFs. The maps are superimposed with grain boundaries which are marked with black lines ($10° < \theta < 93.8°$). The orientation maps display a bimodal microstructure, which includes a mixture of coarsened and fine-sized grains. Some grains distinctively show a color gradient, signifying local disorientation, indicative of plastic lattice strain gradients induced via pilgered fabrication process and the applied loading conditions.

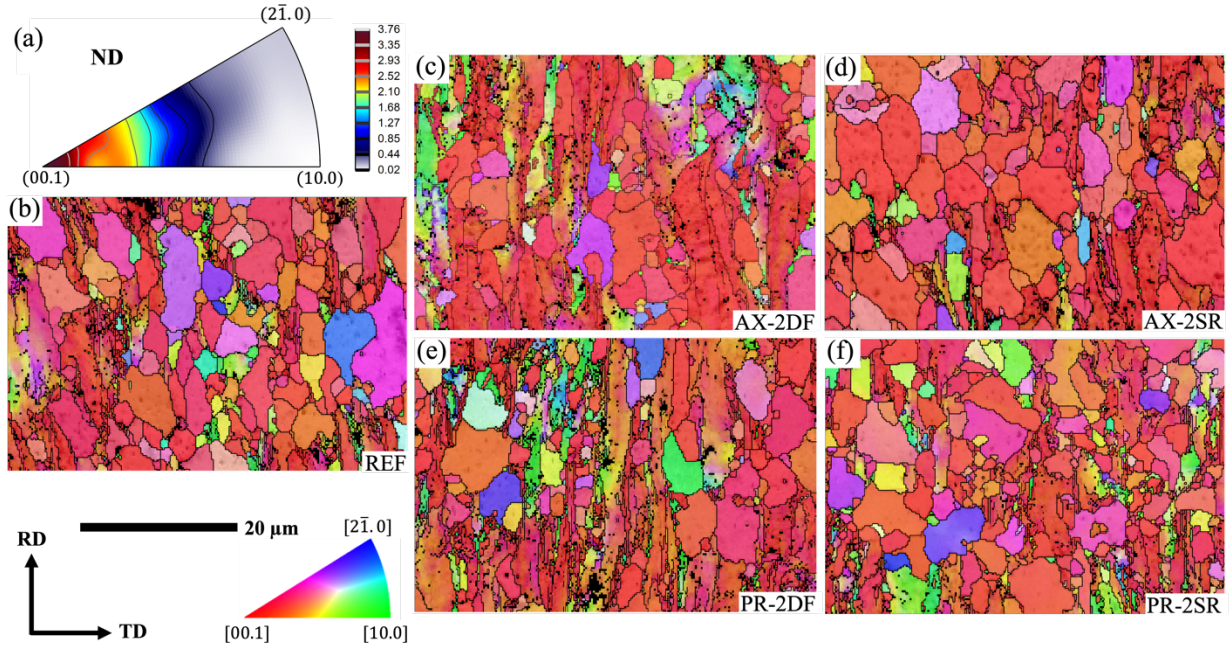

Figure 5-12: (a) ND||IPF showing the REF sample texture. (b-f) are ND||IPF micrographs for EBSD characterized samples at 2500x magnification. Unindexed pixels are shown in black and the ND||IPF color legend is shown in the bottom left corner using a stereographic triangle.

The strain gradients are visualized using KAM micrographs in Figure 5-13 and quantified using histograms in Figure 5-14. The RX fractions and KAM histograms indicate that the deformed samples accumulate misorientation which decreases in the deformed and stress relaxed samples. Additional micrographs are acquired at 2500x magnification and 500 nm step size at different locations improve the area statistics, and the KAM results of the pristine sample shown in Figure 5-15 to demonstrate microstructure variability. The pristine sample RX fraction varies by 41%, and the variation increases upon deformation up to 87%.

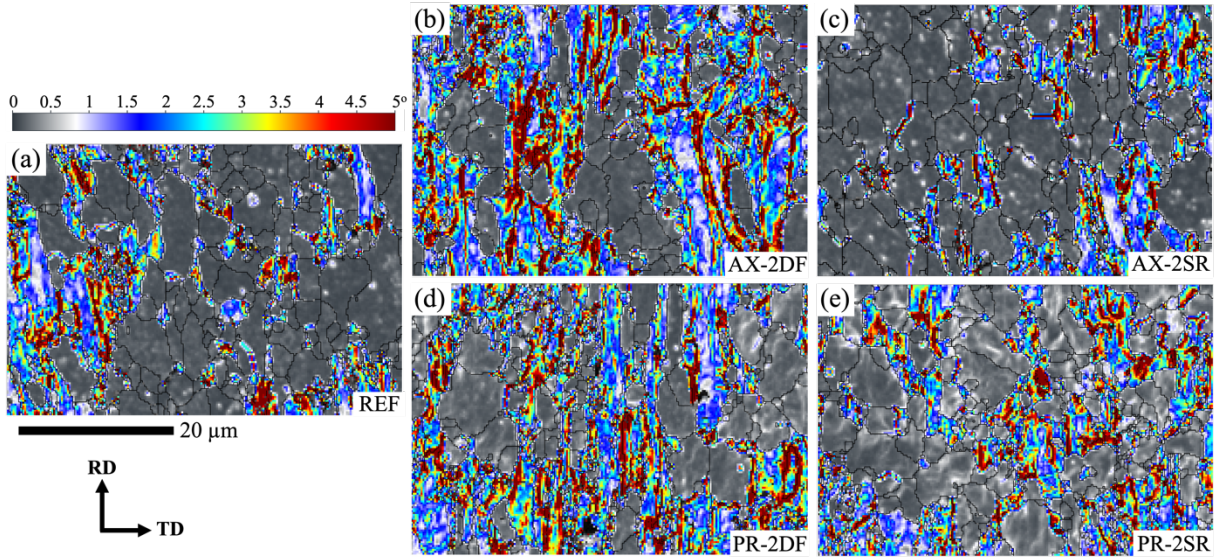

Figure 5-13: KAM micrographs for characterized samples at 2500x magnification and 250 nm step size.

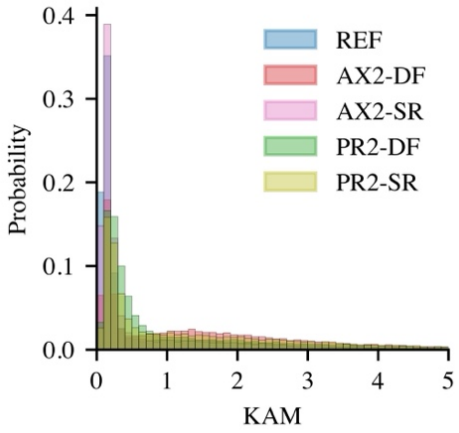

Figure 5-14: KAM histograms for EBSD characterized samples at 2500x magnification.

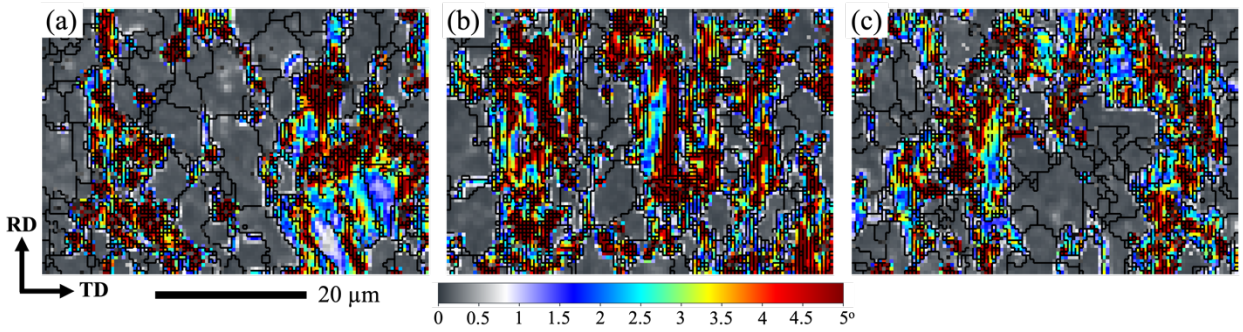

Figure 5-15: KAM micrographs for the REF sample in three different locations at 2500x magnification and 500 nm step size. The RX fraction for (a), (b), and (c) is 59.6%, 39.4%, and 50.0%, respectively.

5.3.3 Thermo-Mechanical Simulation

The BISON FEM thermo-mechanical simulation results shown in Figure 5-16 and Figure 5-17 present the behavior of a typical PWR fuel rod during a PCI due to a power ramp at high burnup. Figure 5-16 shows the entire power history and fuel-cladding gap for simulations with and without the viscoplastic creep models. The gap is initially 80 μm which decreases to 73 μm due to external reactor pressure, and quickly shrinks as the power is ramped and the fuel pellets grow due to thermal expansion. The gap increases slightly towards the beginning of the power history due to fuel densification but then decreases due to fuel swelling and cladding creep-down due to the external pressure of the PWR conditions. Simulations are run with and without the viscoplastic thermal creep model to show the fuel-cladding gap reduction effects from fuel swelling independent of cladding creep-down. The linear gap reduction rates modeling fuel swelling only and fuel swelling plus creep-down are 0.05 and 0.09 μm/day, respectively, so the creep-down rate is 0.04 μm/day.

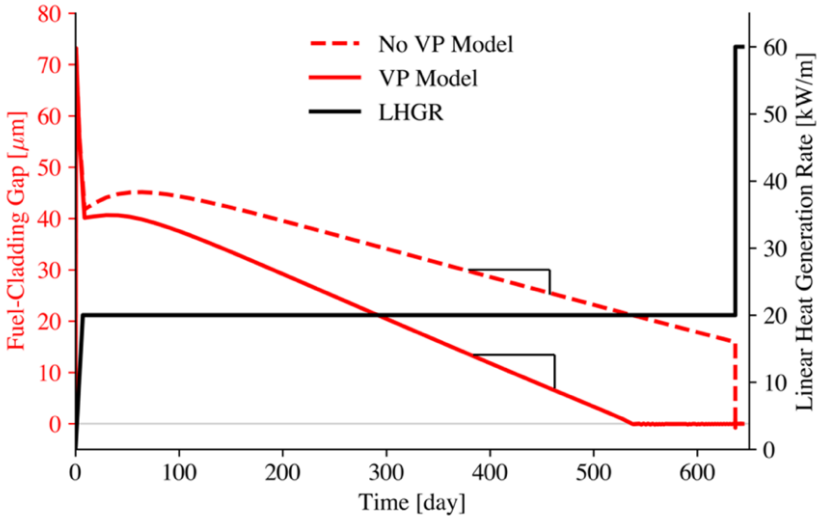

Figure 5-16: Simulated fuel-cladding gap response over the power history for models with and without the viscoplastic (VP) mechanical model.

Figure 5-17 displays the stress response from a PCI during loading and relaxation. The stresses (axial, hoop, radial) produced by the PCI upon reaching 60 kW/m are (266, 383, -40.8) MPa, achieving an axial to hoop ratio of 0.7 and radial to hoop ratio of 0.1 which is near the 0.75 stress state used for the stress analysis in Chapter 4. The stress relaxation behavior shows the axial and hoop stresses relaxing to similar levels and predicts that the effective SRA over the first eight hours is 16.4% and that over the entire week-long stress relaxation period the SRA is 43.6%. The power ramp from 20kW/m to 30, 40, 50, and 60 kW/m impose absolute hoop strain increases of 5.3E-4, 0.325, 1.07, and 1.97 %, respectively. Respective to these power levels, the simulated average cladding temperature increases from 310 °C to 330, 350, 365, and 380 °C where it remains for the relaxation period.

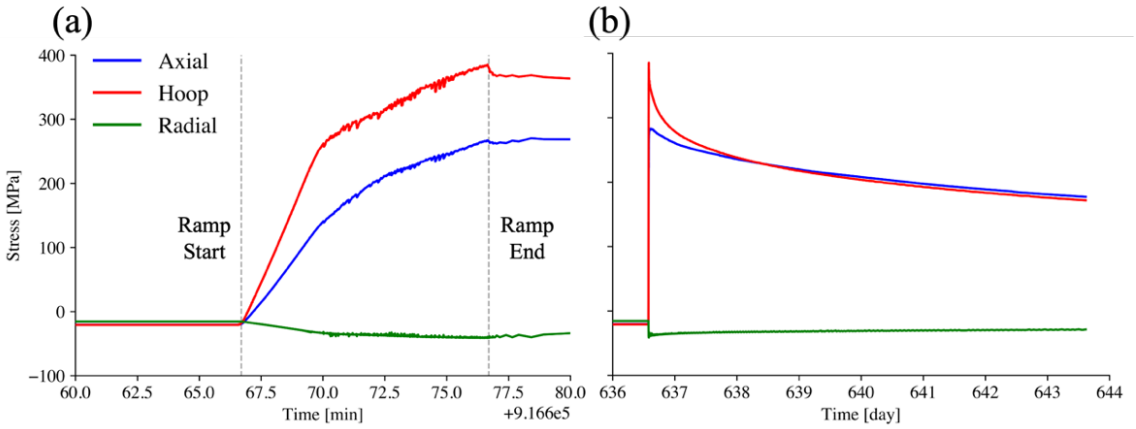

Figure 5-17: Stress response versus time for the ten-minute PCI power ramp (a) and one week relaxation period (b).

The simulated stress relaxation results of the Zry-4 thermal creep material model used by BISON are compared to the measured relaxation behavior in Figure 5-18 (a) and (b). The material models do not calculate the experimentally measured stress accumulation during loading, so the measured effective stresses at the beginning of the relaxation period listed in Table 5-2 are used to evaluate the viscoplastic material model. The material model calculates the viscoplastic strain rates shown in Figure 5-18 (c) and (d) using the appropriate temperature, initial stress, and material properties provided by the model [168]. The high initial stress of the PR2-SR sample in Figure 5-18 (d) causes the primary creep component of the model to saturate around hour-6, causing the viscoplastic strain rate to decrease to the secondary creep rate. Figure 5-18 (e) and (f) show the model error from experimental stress relaxation results. The creep material model most accurately predicts the stress relaxation behavior below yield and for axial tension behavior, remaining below 3% error for both SRTs below yield and below 10% error for all uniaxial SRTs within the 8-hour test period. Compared to predicted results, the experimental samples relax much faster within the first hour but by the second hour the relaxation rate is lower than the model prediction until primary creep is saturated. The former occurs because the creep model does not permit plasticity during the VRR period which can occur during stress relaxation tests loaded beyond yield [54], [120]. The latter appears to occur because the creep model does not limit the work applied to the material.

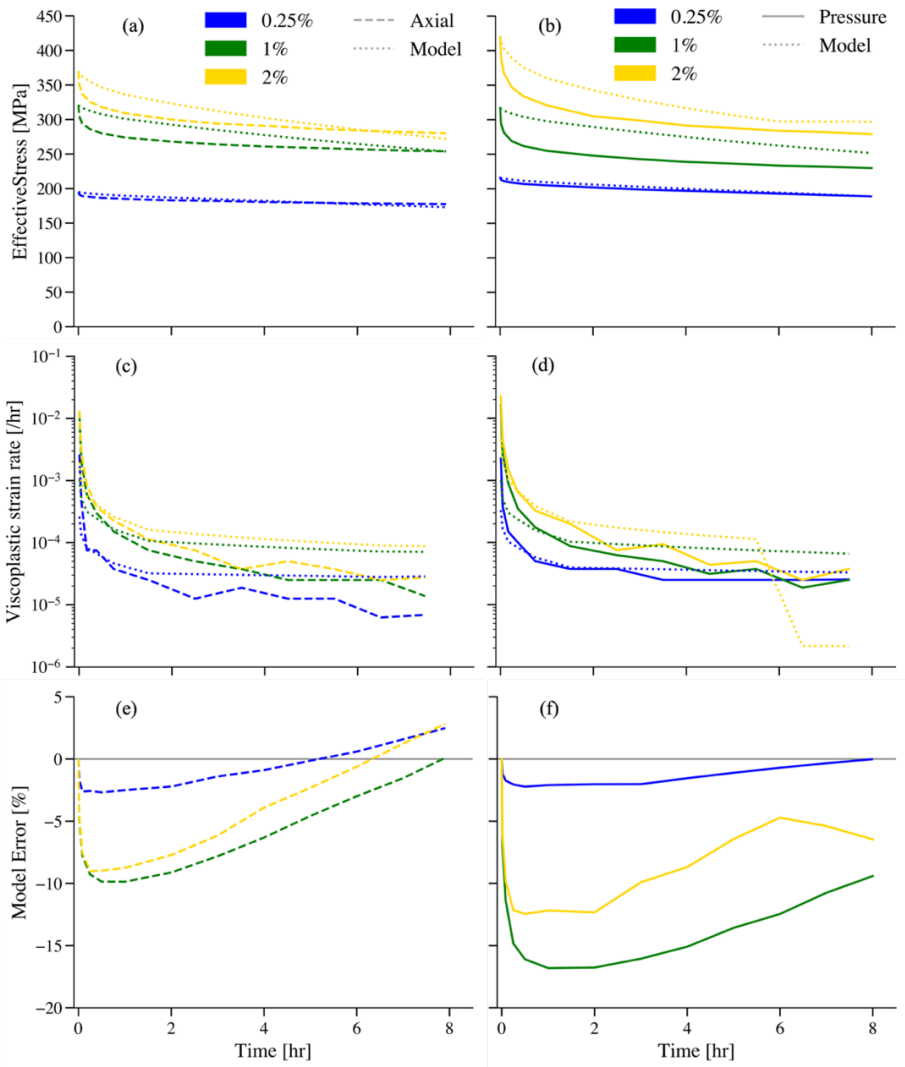

Figure 5-18: Comparison of stress relaxation behavior between experimental results and material model predictions. Axial tension results are compared to model predictions in (a), (c), and (e) and internal pressure results are compared in (b), (d), and (f).

5.4 Discussion

In this chapter, the effects of stress conditions and imposed strain on the stress relaxation behavior of Zry-4 cladding at high stresses are studied through axial tension and internal pressure experiments. The mechanical tests reveal that, under similar experimental conditions, internal pressure loading allows for greater stress relaxation compared to the axial tension loading. Mechanical testing and microstructure analysis results indicate that varying stress conditions may lead to discrepancies in stress generation, dislocation formation, and dislocation activity during loading and relaxation. These factors – stress generation, dislocation formation, and dislocation activity – are identified in Hypotheses 1-3 from Chapter 2 as key influencers on the stress relaxation behavior postulated in the Thesis Statement when thermal conditions and pristine microstructure are uniform.

The initial stresses listed in Table 5-2 are generally higher for internal pressure loading than axial tension, though the -1SR samples are a notable exception. However, Figure 5-7 shows that consistent loading conditions resulting in different initial stresses display similar relaxation behavior, while Figure 5-8 (a) shows that the PR-1SR sample displays enhanced relaxation behavior compared to the AX-1SR when the initial stresses are comparable. These results suggest that small variations in initial stress levels are insufficient to explain the superior stress relaxation observed under biaxial conditions. Therefore, dislocation production and activity are discussed to elucidate the mechanisms of enhanced relaxation behavior of samples loaded *via* internal pressurization.

The microstructure analysis presents results indicating that the defect energy increases upon deformation and decreases during relaxation. However, lower imposed strain and characterization at only one length scale in the present study produces results that are not as clear as those presented in Chapter 4. The background misorientation from pilgering obscures the effects of deformation and relaxation, and the microstructure varies significantly depending on the characterized area. Samples loaded below yield do not change the initial microstructures, but the PR-ESR sample exceeds the AX-ESR relaxation during the SRR. Figure 5-9 (a) shows that the defect energy produced by plastic strain is an important variable affecting the SRA, but the identical power law exponents relating them indicates that there is not a disproportionate effect on SRA from microstructure produced by internal pressure loading. Instead, the proportional offset in the power-law relationships indicates that a variable unrelated to plastic deformation, such as RSS distributions, accounts for the enhanced relaxation behavior. Therefore, this investigation turns to differences in dislocation activity to account for the enhanced stress relaxation behavior in pressurized samples.

At high stresses, Zircaloys display an athermal deformation regime, typically spanning temperatures between 275°C and 600°C depending on the alloy, which corresponds with an activation volume peak [51], [104], [105], [106], [134]. In the case of Zry-4, the apparent activation volume increases from approximately 160 b^3 at 300 °C to exceed 400 b^3 within the temperature range of 350 °C to 450 °C, subsequently decreasing back to ~160 b^3 at 500 °C [104]. There is good agreement that below this athermal regime, the deformation mechanism is predominantly governed by dislocation-solute interactions, which act as the rate-limiting deformation mechanism [51], [104], [105], [106], [123]. Above the athermal regime, dislocation cross-slip is considered the principal rate-limiting deformation mechanism [50], [102], [104], [111]. High stresses within the athermal regime, stress exponents beyond the power-law breakdown regime, and decreasing activation volumes with increasing strain, are phenomena attributed to non-conservative jog and dipole dragging [88], [102], [103], [105], [106], [109], [111]. Additionally, oxygen diffusion kinetics may induce DSA effects, further impeding deformation within this temperature range [51], [54], [104].

The stress relaxation behavior measured in the current study is consistent with screw dislocation motion on prismatic planes limited by non-conservative edge dislocation jog and dipole motion on basal planes [50], [88], [97], [98], [102], [103], [104], [105], [106], [108], [109], [110], [111], [170]. An investigation on stress relaxation in CWSR Zry-4 from Povolo & Rubio [54] and supporting results from others [115], [117], [118], [119], [171] indicate that, during the VRR period, existing dislocations may glide at high stresses near the plastic flow stress, quickly propagating deformation and homogenizing stress. As stress decreases and dislocation velocities slow, screw dislocations and dislocation loops on parallel prismatic planes can form edge dislocation jogs and dipoles on basal planes to achieve more stable configuration [102], [103],

[104], [111], [172], [173]. These jogs and dipoles cannot glide with the screw dislocations, drastically reducing screw dislocation mobility [97], [103], [111], [172]. Instead, the edge dislocations are forced to climb or are bypassed and ultimately become stationary sources of Frank-Reed dislocations [20], [88], [97], [102], [103], [104], [106], [108], [111]. In this context, Moon et al. [102] and Morrow et al. [103] used transmission electron microscopy (TEM) to directly observe dislocations in Zry-4 creep samples. These samples were subjected to temperatures, stresses, and strains comparable to those in the current study and found screw dislocations on parallel prismatic planes with edge dislocation jogs and dipoles on basal planes. Therefore, the active mechanisms of deformation during stress relaxation can be traced to the glide of screw dislocations on prismatic planes during the VRR period which become increasingly limited by edge dislocation jogs and dipole mobility on basal planes in the SRR period.

The enhanced relaxation in the pressure loading mode is attributed to differing RSS distributions produced within the textured Zry-4 cladding alongside potential differences in the deformation microstructure. This relationship is shown in Figure 5-19 (a) and (b) showing the GSF results of the prismatic <*a*> and basal <*a*> systems for the axial tension and internal pressure loading modes from Chapter 4 Section 3.3. The mobility of the edge dislocations on basal planes is enhanced by high Schmid factors for basal <*a*> slip, particularly when the basal <*a*> Schmid factor is higher than prismatic <*a*> Schmid factor [111]. Higher Schmid factors for basal <*a*> slip in the pressure loading mode increases the jog and dipole mobility [110], which can explain the enhanced stress relaxation and decreased activation volume of this loading mode compared to the axial mode. Increased basal <*a*> activity above 300 °C is supported by reduced mechanical anisotropy for stress states that produce high Schmid factors on this system [58], [111], [134].

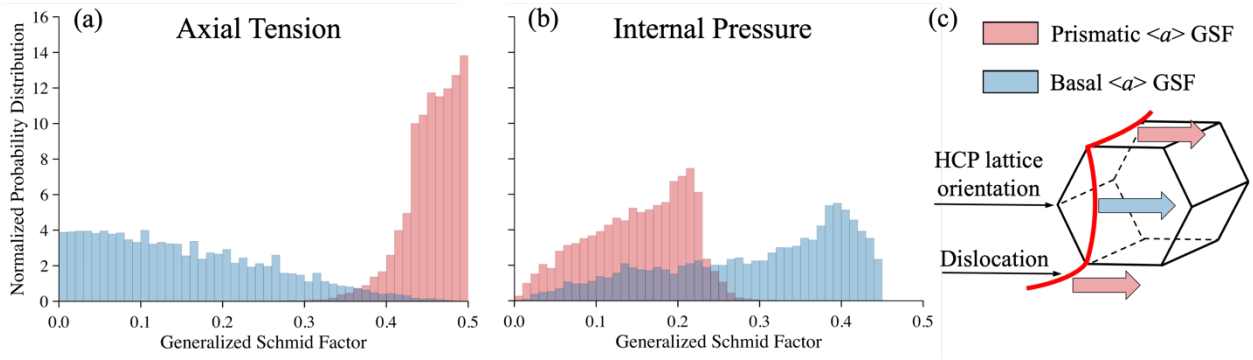

Figure 5-19: Prismatic <a> and basal <a> GSF results from Chapter 4 for the (a) axial tension and (b) internal pressure loading modes. (c) Schematic representation of screw dislocations on parallel prismatic planes with an edge jog on the basal plane; arrows show the relationship of the dislocations with their corresponding GSF.

5.5 Conclusions

Conclusions from this study of viscoplastic deformation behavior and how they relate to the goals and hypotheses of this dissertation are summarized below and discussed further in Chapter 6.

- The internal pressure stress state enhances stress relaxation compared to the axial tension stress state at all strains tested, confirming Hypothesis 4 and its contribution to the Thesis Statement.

- The initial stresses measured at the beginning of the stress relaxation period are similar or slightly higher for the internal pressure loading mode compared to the axial tension mode, supporting Hypothesis 1. However, stress has an insignificant effect on the stress relaxation behavior compared to the stress state, invalidating its contribution to the Thesis Statement.
- The microstructure evolution results display variation within a single sample exceeding variation between samples, and the uncertain results provide limited evidence against Hypothesis 2. Mechanical testing results provide more definite evidence invalidating its contribution to the Thesis Statement.
- The rate-limiting deformation mechanism during stress relaxation is attributed to glide of screw dislocations on prismatic planes during the VRR period which become increasingly limited by edge dislocation jogs and dipole mobility on basal planes in the SRR period.
- Enhanced stress relaxation from internal pressure is caused by the relatively high basal <*a*> RSS distribution it imposes on the textured cladding, accelerating the rate-limiting basal jog and dipole mobility, confirming Hypothesis 3 and its contribution to the Thesis Statement.
- Themo-mechanical material models employed by current fuel performance codes better simulate uniaxial stress results used to create the models than the multiaxial stresses typical of reactor conditions.

Chapter 6 Conclusions

This dissertation investigates the anisotropic deformation mechanisms of stress relaxation in CWSR Zry-4 cladding by comparing the mechanical behavior of axial tension testing commonly used to measure cladding properties and internal pressure testing which is more prototypic of PCI conditions. Experiments varying the stress states and test temperatures are used to reveal differences in mechanical behavior, RSS distribution, microstructure evolution, and temperature dependence which are interpreted through fundamental deformation mechanisms and published as peer-reviewed journal manuscripts. These methods are developed to test the Hypotheses postulated in Chapter 2 individually and their contribution to the Thesis Statement, which is discussed in this chapter.

The mechanical behavior measured in this dissertation such as yield, hardening, and plastic strain rates are consistent with literature which helps validate the experimental methods used. Mechanical anisotropy, primarily the cladding resistance to thinning, is observed as the relatively low radial plastic strain rate during uniaxial testing and the high yield stress measured for internal pressure testing at room temperature. Internal pressure and PCI loading induce positive axial stress that competes with the Poisson effect from high hoop stress, reducing axial strain and increasing radial thinning, which the cladding texture resists. This additional strength for internal pressure loading is significant up to 300 ^{o}C but disappears at 400 ^{o}C, confirming Hypothesis 1 for the relaxation conditions tested.

The temperature-dependent mechanical anisotropy observed for internal pressure testing is not observed for axial tension. Cladding mechanical anisotropy is greatly reduced where prismatic and basal systems permit deformation on orthogonal slip planes simultaneously, but relative slip system activity is dependent on the temperature and the Schmid factor distributions produced by the stress state. It is well-known that HCP lattice asymmetry favors prismatic slip (low CRSS), but this anisotropy decreases at elevated temperature allowing the basal system to operate simultaneously when the Schmid factor distributions efficiently load the basal systems. The internal pressure and PCI stress states produce Schmid factor distributions that favor basal slip while the distribution from the axial tension stress state favors prismatic slip. This dissertation reveals that these biaxial stress states, as well as TD-tension, permit competitive basal-prismatic slip activity and reduced mechanical anisotropy when the temperature reduces the basal-prismatic CRSS ratio sufficiently, near 300 ^{o}C. In contrast, the axial tension stress state does not load basal systems efficiently producing dominant prismatic slip activity at all temperatures and, thus, temperature-independent mechanical anisotropy. These findings confirm Hypothesis 3.

The CWSR Zry-4 cladding microstructure is successfully characterized showing clear differences between pristine and deformed microstructure, fulfilling the primary goal of this component of the dissertation. Further, Chapter 4 provides evidence at multiple length scales that biaxial loading relevant to PCI conditions produces increased deformation microstructure compared to samples tested with uniaxial loading along the RD at relatively high strains (4-5%). These results are supported by VPSC simulations indicating that the deformation microstructure is sensitive to the anisotropy observed in textured Zircaloy and that the uniaxial-deformed microstructure may not be representative of the PCI conditions for sensitive analysis. Analysis suggests that internal pressure loading is a relatively low symmetry loading mode compared to loading parallel to the RD which develops relatively high plastic spin that is observed as increased misorientation in the microstructure. However, characterization results in Chapter 5 struggled to

resolve differences in microstructure between loading mode, temperature, and loading history at relatively low strain (2%) that could definitively evaluate Hypothesis 2. Pristine CWSR microstructure includes significant uRX microstructure obscuring deformation induced uRX microstructure in the natural variation background, and the significant resources required to characterize this challenging material limited the characterization scope. Therefore, there is limiting evidence supporting Hypothesis 2, but these results are not conclusive.

Mechanical testing finds that the internal stress state displays enhanced stress relaxation compared to axial tension under equivalent conditions, confirming Hypothesis 4. Multiple imposed strains are used to show that this effect amplifies with increasing strain levels, particularly above yield, according to a power law. The mechanical data are analyzed, and results are compared to literature with the thermal and stress conditions, finding that the rate-limiting deformation mechanism is screw dislocation glide on prismatic planes limited by edge dislocation jog and dipole climbing on basal planes. High Schmid factors on basal systems for the internal pressure stress state accelerate the jog and dipole climb which can account for the enhanced relaxation rates observed for samples tested with that loading mode.

Elastic energy, defect energy, and slip system activity are identified in Hypotheses 1-3, respectively, as key variables contributing the stress relaxation behavior identified in Hypothesis 4 as described in the Thesis Statement. Variable yield is common in CWSR Zry-4 which cladding helps evaluate the contribution of Hypothesis 1 by comparing different initial stresses under similar loading conditions and similar stresses with different stress states. While high stress does increase the relaxation rates, the variation in initial stresses between loading modes in the present work is insignificant, dismissing the contribution of Hypothesis 1 to the Thesis Statement. The relationship between plastic strain and stress relaxation indicates that defect energy affects the relaxation behavior and there is limited evidence that there is increased defect energy from internal pressure loading. However, unclear differences between microstructures produced by the loading modes and the mechanical data comparisons discussed in Chapter 5 Section 4 indicate that differences in defect energy have an insignificant effect, dismissing the contribution of Hypothesis 2 to the Thesis Statement. Identifying the rate-limiting deformation mechanism and the Schmid factor analysis provide strong evidence that competitive slip system activity, particularly that of the basal slip system, is the primary variable contributing to the enhanced stress relaxation identified in Hypothesis 4, confirming the contributions of Hypotheses 3 and 4 to the Thesis Statement. Summarizing these findings, the Thesis Statement is amended to the following form.

For the same applied equivalent strain, internal pressure loading displays enhanced stress relaxation compared to axial tension loading because there is more competition between active deformation systems which accelerates the rate-limiting deformation mechanism.

Macroscopic mechanical behavior of Zry cladding in reactor conditions is the result of many compounded mechanisms that have complex interdependency at various length scales. Experiments must simplify the nuclear environment for feasibility, but understanding the simplifications made and the resulting effects on deformation behavior is critical to ensure representative data for modeling, design, and qualification. This dissertation highlights the importance of basal slip and the need for biaxial testing methods such as compressed pellet and internal pressurize loading to emulate PCI events for anisotropic cladding. This is particularly consequential when introducing additional physics such as hydride, viscoplastic, or irradiation behavior where mechanism interdependencies are unclear, as demonstrated by the enhanced stress

relaxation behavior observed in this dissertation. For experiments requiring uniaxial loading, the RSS distribution of the PCI stress state is better simulated by uniaxial tension along the TD than along the RD.

Chapter 7 References

[1] IPCC, "Mitigation of Climate Change," *Clim. Change 2022*, 2022, doi: 10.1201/9781003264705-7.

[2] S. AAS, "Mechanical interaction between fuel and cladding," *Nucl. Eng. Des.*, vol. 21, no. 2, pp. 237–253, 1972, doi: 10.1016/0029-5493(72)90075-1.

[3] IAEA, "Progress on Pellet–Cladding Interaction and Stress Corrosion Cracking," in *Experimentation, Modelling and Methodologies Applied to Support the Flexible Operation of Nuclear Power Plants*, Vienna, Austria, 2021.

[4] IAEA, "Non-baseload Operation in Nuclear Power Plants: Load Following and Frequency Control Modes of Flexible Operation," *IAEA Nucl. Energy Ser.*, pp. 1–190, 2018.

[5] NRC, "Standard Review Plan: Fuel System Design," 2007.

[6] NEA, "Technical and Economic Aspects of Load Following with Nuclear Power Plants," no. Nuclear Development, 2011.

[7] NEI, "The Economic Benefits and Challenges with Utilizing Increased Enrichment and Fuel Burnup for Light-Water Reactors Prepared by the Nuclear Energy Institute," 2019.

[8] M. Suzuki, T. Fuketa, and H. Saitou, "Analysis of pellet-clad mechanical interaction process of high-burnup PWR fuel rods by RANNS code in reactivity-initiated accident conditions," *Nucl. Technol.*, vol. 155, no. 3, pp. 282–292, 2006, doi: 10.13182/NT06-A3762.

[9] Y. Udagawa, T. Sugiyama, M. Suzuki, and F. Nagase, "Stress biaxiality in high-burnup PWR fuel cladding under reactivity-initiated accident conditions," *J. Nucl. Sci. Technol.*, vol. 50, no. 6, pp. 645–653, Jun. 2013, doi: 10.1080/00223131.2013.787030.

[10] K. J. Geelhood, "Fuel Performance Considerations and Data Needs for Burnup above 62 GWd/MTU In-Reactor Performance, Storage, and Transportation of Spent Nuclear Fuel," Pacific Northwest National Laboratory, Richland, Washington 99352, PNNL-29368, 2019.

[11] A. Kareer, J. C. Waite, B. Li, A. Couet, D. E. J. Armstrong, and A. J. Wilkinson, "Short communication: 'Low activation, refractory, high entropy alloys for nuclear applications,'" *J. Nucl. Mater.*, vol. 526, p. 151744, Dec. 2019, doi: 10.1016/j.jnucmat.2019.151744.

[12] E. Tenckhoff, *DEFORMATION MECHANISMS, TEXTURE, AND ANISOTROPY IN ZIRCONIUM AND ZIRCALOY*. ASTM Int., 1988.

[13] G. Jiang, D. Xu, W. Yang, L. Liu, Y. Zhi, and J. Yang, "High-temperature corrosion of Zr–Nb alloy for nuclear structural materials," *Prog. Nucl. Energy*, vol. 154, p. 104490, Dec. 2022, doi: 10.1016/j.pnucene.2022.104490.

[14] C. Lemaignan, *Zirconium alloys: Properties and characteristics*, vol. 2. Elsevier Inc., 2012, p. 232. doi: 10.1016/B978-0-08-056033-5.00015-X.

[15] K. L. Murty and I. Charit, "Texture development and anisotropic deformation of zircaloys," *Prog. Nucl. Energy*, vol. 48, no. 4, pp. 325–359, 2006, doi: 10.1016/j.pnucene.2005.09.011.

[16] G. M. O'Donnell, H. H. Scott, and R. O. Meyer, "A New Comparative Analysis of LWR Fuel Designs." U.S. Nuclear Regulatory Commission, 2001. [Online]. Available: https://www.nrc.gov/docs/ML0136/ML013650469.pdf

[17] D. Kamerman, "The deformation and burst behavior of Zircaloy-4 cladding tubes with hydride rim features subject to internal pressure loads," *Eng. Fail. Anal.*, vol. 153, p. 107547, Nov. 2023, doi: 10.1016/j.engfailanal.2023.107547.

[18] D. Kamerman and M. Nelson, “Multiaxial Plastic Deformation of Zircaloy-4 Nuclear Fuel Cladding Tubes,” *Nucl. Technol.*, pp. 1–15, Feb. 2023, doi: 10.1080/00295450.2022.2160174.
[19] H. Kim, Y. Lee, I. Kim, H. Kim, and D. Kim, “On the method to obtain the elastic properties using a pressurized thin tube,” *Eng. Fail. Anal.*, vol. 111, no. August 2019, pp. 104438–104438, 2020, doi: 10.1016/j.engfailanal.2020.104438.
[20] B. Kombaiah and K. L. Murty, “Coble, Orowan Strengthening, and Dislocation Climb Mechanisms in a Nb-Modified Zircaloy Cladding,” *Metall. Mater. Trans. A*, vol. 46, no. 10, pp. 4646–4660, Oct. 2015, doi: 10.1007/s11661-015-3060-8.
[21] T. Mihara, Y. Udagawa, and M. Amaya, “Deformation behavior of recrystallized and stress-relieved Zircaloy-4 fuel cladding under biaxial stress conditions,” *J. Nucl. Sci. Technol.*, vol. 55, no. 2, pp. 151–159, Feb. 2018, doi: 10.1080/00223131.2017.1383213.
[22] Y. Miyamoto, Y. Komatsu, T. Kakuma, and N. Nagai, “Mechanical behavior of Zircaloy-2 tubing under biaxial stresses,” *J. Nucl. Mater.*, vol. 61, no. 1, pp. 53–65, Jul. 1976, doi: 10.1016/0022-3115(76)90097-0.
[23] K. L. Murty, “Creep studies for zircaloy life prediction in water reactors,” *JOM*, vol. 51, no. 10, pp. 32–39, Oct. 1999, doi: 10.1007/s11837-999-0184-6.
[24] C. S. Seok, B. Marple, Y. J. Song, S. Gollapudi, I. Charit, and K. L. Murty, “High temperature deformation characteristics of Zirlo™ tubing via ring-creep and burst tests,” *Int. Conf. Struct. Mech. React. Technol. SMiRT19 Spec. Sect.*, vol. 241, no. 3, pp. 599–602, Mar. 2011, doi: 10.1016/j.nucengdes.2010.04.017.
[25] DOE, “Quadrennial Technology Review 2015 Chapter 4M: Light Water Reactors.” U.S. Department of Energy, 2015.
[26] IAEA, “Advanced Reactors Information System.” Accessed: Mar. 03, 2024. [Online]. Available: https://aris.iaea.org/
[27] J. McKinley, W. Bamford, A. Ruminski, T. Meikle, and J. McFadden, “Comparison of Boiling Water Reactor and Pressurized Water Reactor Experience with Cracking of Austenitic Stainless Steel.” Westinghouse Electric Company, 2018.
[28] NRC, “Fuel Behavior under Abnormal Conditions,” 2013.
[29] J. Ni, Y. Zhao, L. Wang, Z. Zhang, and J. Xie, “Microstructure of Zircaloy-4 alloy during β phase quenching and determination of critical quenching diameter of its rods,” *Nucl. Mater. Energy*, vol. 17, pp. 158–163, Dec. 2018, doi: 10.1016/j.nme.2018.10.014.
[30] A. I. Kolesnikov, A. M. Balagurov, I. O. Bashkin, A. V. Belushkin, E. G. Ponyatovsky, and M. Prager, “Neutron scattering studies of ordered gamma -ZrD,” *J. Phys. Condens. Matter*, vol. 6, no. 43, pp. 8977–8977, 1994, doi: 10.1088/0953-8984/6/43/004.
[31] J. G. Couterne and G. Cizeron, “Determination des coefficients principaux d’expansion thermique du Zr α,” *J. Nucl. Mater.*, vol. 20, no. 1, pp. 75–82, Jul. 1966, doi: 10.1016/0022-3115(66)90023-7.
[32] C. L. Whitmarsh, “Review of Zircaloy-2 and Zircaloy-4 Properties Relevant to N.S. Savannah Reactor Design,” 1962.
[33] A. Akhtar, “BASAL SLIP IN ZIRCONIUM,” *Acta Metall.*, vol. 21, 1973.
[34] G. Bharat Reddy, A. Sarkar, R. Kapoor, and A. K. Kanjarla, “Effect of temperature on the selection of deformation modes in Zircaloy-4,” *Mater. Sci. Eng. A*, vol. 734, pp. 210–223, Sep. 2018, doi: 10.1016/j.msea.2018.07.094.

[35] S. Wang, F. Giuliani, and T. Ben Britton, “Variable temperature micropillar compression to reveal <a> basal slip properties of Zircaloy-4,” *Scr. Mater.*, vol. 162, pp. 451–455, Mar. 2019, doi: 10.1016/j.scriptamat.2018.12.014.
[36] S. Deng, H. Song, C. Zheng, T. Zhao, S. Zhang, and K. B. Nielsen, “Selection of deformation modes and related texture evolution in Zircaloy-4 during one pass cold pilgering,” *Mater. Sci. Eng. A*, vol. 764, Sep. 2019, doi: 10.1016/j.msea.2019.138280.
[37] Z. C. Ma, X. Z. Tang, Y. Mao, and Y. F. Guo, “The plastic deformation mechanisms of hcp single crystals with different orientations: Molecular dynamics simulations,” *Materials*, vol. 14, no. 4, pp. 1–16, 2021, doi: 10.3390/ma14040733.
[38] R. J. McCabe, E. K. Cerreta, A. Misra, G. C. Kaschner, and C. N. Tomé, “Effects of texture, temperature and strain on the deformation modes of zirconium,” *Philos. Mag.*, vol. 86, no. 23, pp. 3595–3611, 2007, doi: 10.1080/14786430600684500.
[39] G. Monnet, B. Devincre, and L. P. Kubin, “Dislocation study of prismatic slip systems and their interactions in hexagonal close packed metals: Application to zirconium,” *Acta Mater.*, vol. 52, no. 14, pp. 4317–4328, 2004, doi: 10.1016/j.actamat.2004.05.048.
[40] C. Liu *et al.*, “Texture and yielding anisotropy of Zircaloy-4 alloy cladding tube produced by cold Pilger rolling and annealing,” *Mater. Sci. Eng. A*, vol. 719, pp. 147–154, Mar. 2018, doi: 10.1016/j.msea.2018.02.043.
[41] C. Lemaignan and A. Motta, “Zirconium alloys in nuclear applications,” *Mater. Sci. Technol.*, 2006.
[42] G. C. Kaschner, C. N. Tomé, I. J. Beyerlein, S. C. Vogel, D. W. Brown, and R. J. McCabe, “Role of twinning in the hardening response of zirconium during temperature reloads,” *Acta Mater.*, vol. 54, no. 11, pp. 2887–2896, 2006, doi: 10.1016/j.actamat.2006.02.036.
[43] A. Staroselsky and L. Anand, “A constitutive model for hcp materials deforming by slip and twinning: Application to magnesium alloy AZ31B,” *Int. J. Plast.*, vol. 19, no. 10, pp. 1843–1864, 2003, doi: 10.1016/S0749-6419(03)00039-1.
[44] K. V. M. Krishna *et al.*, “Microstructural and textural developments during Zircaloy-4 fuel tube fabrication,” *Adv. Nucl. Mater. Process. Perform. Phenom.*, vol. 383, no. 1, pp. 78–85, Dec. 2008, doi: 10.1016/j.jnucmat.2008.08.050.
[45] S. Deng, H. Song, H. Liu, and S. H. Zhang, “Effect of uniaxial loading direction on mechanical responses and texture evolution in cold pilgered Zircaloy-4 tube: Experiments and modeling,” *Int. J. Solids Struct.*, vol. 213, pp. 63–76, 2021, doi: 10.1016/j.ijsolstr.2020.12.015.
[46] C. Evans, N. G. Jones, D. Rugg, T. C. Lindley, and D. Dye, “The effect of deformation mechanisms on the high temperature plasticity of Zircaloy-4,” *J. Nucl. Mater.*, vol. 424, no. 1–3, pp. 123–131, May 2012, doi: 10.1016/j.jnucmat.2012.02.013.
[47] W. Guo *et al.*, “Texture development and mechanical behavior of Zircaloy-4 alloy plates fabricated by cold rolling and annealing,” *Mater. Sci. Eng. A*, vol. 807, no. September 2020, pp. 140846–140846, 2021, doi: 10.1016/j.msea.2021.140846.
[48] P. D. Honniball, M. Preuss, D. Rugg, and J. Quinta da Fonseca, “Grain Breakup During Elevated Temperature Deformation of an HCP Metal,” *Metall. Mater. Trans. A*, vol. 46, no. 5, pp. 2143–2156, 2015, doi: 10.1007/s11661-015-2812-9.
[49] T. Kim, J. Kim, H. Kim, and Y. Kim, “The Prediction of Creep behaviors of Zircaloy-4 Using Uniaxial Stress Relaxation,” in *Transactions of the Korean Nuclear Society Autumn Meeting*, 2014.

[50] B. Kombaiah and K. L. Murty, “Dislocation cross-slip controlled creep in Zircaloy-4 at high stresses,” *Mater. Sci. Eng. A*, vol. 623, pp. 114–123, Jan. 2015, doi: 10.1016/j.msea.2014.11.040.
[51] N. Kumar, A. Alomari, and K. L. Murty, “Understanding thermally activated plastic deformation behavior of Zircaloy-4,” *J. Nucl. Mater.*, vol. 504, pp. 41–49, Jun. 2018, doi: 10.1016/j.jnucmat.2018.03.031.
[52] C. Li *et al.*, “Cyclic stress-strain response of textured Zircaloy-4,” *J. Nucl. Mater.*, vol. 321, no. 1, pp. 60–69, 2003, doi: 10.1016/S0022-3115(03)00200-9.
[53] C. Nam, K.-H. Kim, M.-H. Lee, and Y.-H. Jeong, “Effect of Alloying Elements on the Thermal Creep of Zirconium Alloys,” *J. Korean Nucl. Soc.*, vol. 32, no. 4, pp. 372–378, 2000.
[54] F. Povolo and G. H. Rubiolo, “Load relaxation of cold-worked and stress-relieved Zircaloy-4 near 673 K,” *Philos. Mag. A*, vol. 56, no. 2, pp. 231–250, Aug. 1987, doi: 10.1080/01418618708205163.
[55] H. Shi, J. Li, J. Mao, and W. Lu, “The elimination of the yield point phenomenon in a new zirconium alloy: Influence of degree of recrystallization on the tensile properties,” *Scr. Mater.*, vol. 169, pp. 28–32, Aug. 2019, doi: 10.1016/j.scriptamat.2019.05.008.
[56] J. Singh *et al.*, “Temperature dependence of work hardening in sparsely twinning zirconium,” *Acta Mater.*, vol. 123, pp. 337–349, Jan. 2017, doi: 10.1016/j.actamat.2016.10.049.
[57] S. G. Song and G. T. Gray, “Influence of temperature and strain rate on slip and twinning behavior of zr,” *Metall. Mater. Trans. A*, vol. 26, no. 10, pp. 2665–2675, Oct. 1995, doi: 10.1007/BF02669423.
[58] Y. Wang and K. L. Murty, “Effect of Temperature on Mechanical Anisotropy of Zircaloy-4 Sheet,” *Met. Mater.*, vol. 4, no. 4, pp. 723–726, 1998, doi: 10.1007/BF03026387.
[59] F. Xu, R. A. Holt, and M. R. Daymond, “Modeling lattice strain evolution during uniaxial deformation of textured Zircaloy-2,” *Acta Mater.*, vol. 56, no. 14, pp. 3672–3687, Aug. 2008, doi: 10.1016/j.actamat.2008.04.019.
[60] Y. Zhang *et al.*, “The effect of three-dimensional loading and texture on deformation mechanism of Zircaloy-4 alloy: Using space Schmid factor model,” *Mater. Sci. Eng. A*, vol. 761, Jul. 2019, doi: 10.1016/j.msea.2019.06.002.
[61] H. Shi *et al.*, “The progressive intensification and attenuation of yield point phenomenon in a new polycrystalline zirconium alloy : Anisotropic response of work hardening-softening transition,” *Mater. Sci. Eng. A*, vol. 848, no. June, pp. 143385–143385, 2022, doi: 10.1016/j.msea.2022.143385.
[62] S. Kim, J.-H. Kang, and Y. Lee, “Hydride embrittlement resistance of Zircaloy-4 and Zr-Nb alloy cladding tubes and its implications on spent fuel management,” *J. Nucl. Mater.*, vol. 559, p. 153393, Feb. 2022, doi: 10.1016/j.jnucmat.2021.153393.
[63] K.-C. Lan *et al.*, “A study on texture stability and the biaxial creep behavior of as-hydrided CWSR Zircaloy-4 cladding at the effective stresses from 55 MPa to 65 MPa and temperatures from 300 °C to 400 °C,” *J. Nucl. Mater.*, vol. 564, p. 153688, Jun. 2022, doi: 10.1016/j.jnucmat.2022.153688.
[64] S. K. Sahoo *et al.*, “Heterogeneous deformation in single-phase Zircaloy 2,” *Scr. Mater.*, vol. 56, no. 11, pp. 963–966, Jun. 2007, doi: 10.1016/j.scriptamat.2007.02.008.
[65] A. B. Gokhale and S. BanerJee, *Sample Preparation For Metallography*. in Major Reference Works. John Wiley & Sons, 2012.

[66] K.-C. Lan *et al.*, “The challenge of acquiring a satisfactory EBSD result of CWSR Zircaloy-4 cladding tube,” *J. Microsc.*, vol. 272, no. 1, pp. 25–34, 2018, doi: 10.1111/jmi.12729.
[67] S. Deng, S. Wang, S. Chen, C. Zheng, H. Song, and S. Zhang, “Texture evolution of Zircaloy-4 tube during cold pilgering: Operating mechanism of Q factor,” *J. Nucl. Mater.*, vol. 589, p. 154846, Feb. 2024, doi: 10.1016/j.jnucmat.2023.154846.
[68] D. Fuloria, N. Kumar, R. Jayaganthan, S. K. Jha, and D. Srivastava, “Microstructural and textural characterization of Zircaloy-4 processed by rolling at different temperatures,” *Mater. Charact.*, vol. 127, pp. 296–310, May 2017, doi: 10.1016/j.matchar.2017.02.020.
[69] L. Anand and S. Govindjee, *Continuum Mechanics of Solids*, First Edit. Oxford University Press, 2020. doi: 10.1093/oso/9780198864721.001.0001.
[70] P. Anderson, J. Hirth, and J. Lothe, *Theory of Dislocations*, Third. Cambridge University Press, 2017.
[71] O. Hoffman and G. Sachs, *Introduction to the Theory of Plasticity for Engineers*. McGraw-Hill Book Company, Inc., 1953.
[72] P. Hosemann, “Nuclear Materials,” presented at the Nuclear Engineering 120: Nuclear Materials, University of California, Berkeley, 2020.
[73] W. F. Hosford, *Fundamentals of Engineering Plasticity*. Cambridge: Cambridge University Press, 2013. doi: 10.1017/CBO9781139775373.
[74] D. Hull and D. J. Bacon, *Introduction to Dislocations*, 5th ed. 2011. [Online]. Available: https://doi.org/10.1016/C2009-0-64358-0
[75] S. Wiederhorn *et al.*, “Mechanical Properties,” in *Springer Handbook of Materials Measurement Methods*, H. Czichos, T. Saito, and L. Smith, Eds., Berlin, Heidelberg: Springer Berlin Heidelberg, 2006, pp. 283–397. doi: 10.1007/978-3-540-30300-8_7.
[76] N. V. Kamyshanchenko, I. S. Nikulin, E. S. Kungurtsev, and M. S. Kungurtsev, “Experimental determination of preferential mechanisms of stress relaxation during deformation of HCP metals,” *Tech. Phys. Lett.*, vol. 39, no. 5, pp. 469–471, 2013, doi: 10.1134/S1063785013050210.
[77] Y. Liu, W. Wan, and F. P. E. Dunne, “Characterisation and modelling of micro- and macroscale creep and strain rate sensitivity in Zircaloy-4,” *Mater. Sci. Eng. A*, vol. 840, p. 142981, Apr. 2022, doi: 10.1016/j.msea.2022.142981.
[78] H. Yu, Y. Xin, M. Wang, and Q. Liu, “Hall-Petch relationship in Mg alloys: A review,” *J. Mater. Sci. Technol.*, vol. 34, no. 2, pp. 248–256, Feb. 2018, doi: 10.1016/j.jmst.2017.07.022.
[79] P. Tejland and H.-O. Andrén, “Oxidation induced localized creep deformation in Zircaloy-2,” *J. Nucl. Mater.*, vol. 444, no. 1, pp. 30–34, Jan. 2014, doi: 10.1016/j.jnucmat.2013.09.020.
[80] T. A. Hayes and M. E. Kassner, “Creep of zirconium and zirconium alloys,” *Metall. Mater. Trans. Phys. Metall. Mater. Sci.*, vol. 37, no. 8, pp. 2389–2396, 2006, doi: 10.1007/BF02586213.
[81] S. S. Vagarali and T. G. Langdon, “Deformation mechanisms in h.c.p. metals at elevated temperatures—II. Creep behavior of a Mg-0.8% Al solid solution alloy,” *Acta Metall.*, vol. 30, no. 6, pp. 1157–1170, 1982, doi: 10.1016/0001-6160(82)90009-8.
[82] B. Garrison, Y. Yan, and S. TerMaath, “Determining failure properties of as-received and hydrided unirradiated Zircaloy-4 from ring compression tests,” *Eng. Fail. Anal.*, vol. 125, no. February, pp. 105362–105362, 2021, doi: 10.1016/j.engfailanal.2021.105362.

[83] F. Nagase, T. Sugiyama, and T. Fuketa, “Optimized Ring Tensile Test Method and Hydrogen Effect on Mechanical Properties of Zircaloy Cladding in Hoop Direction Optimized Ring Tensile Test Method and Hydrogen Effect,” *J. Nucl. Sci. Technol.*, vol. 46, no. 6, pp. 545–552, 2009, doi: https://doi.org/10.1080/18811248.2007.9711560.

[84] J. Gong, T. B. Britton, M. A. Cuddihy, F. P. E. Dunne, and A. J. Wilkinson, “<a> Prismatic, <a> basal, and <c + a> slip strengths of commercially pure Zr by micro-cantilever tests,” vol. 96, pp. 249–257, 2015, doi: 10.1016/j.actamat.2015.06.020.

[85] N. Christodoulou, P. A. Turner, E. T. C. Ho, C. K. Chow, and M. R. Levi, “Anisotropy of Yielding in a Zr-2.5Nb Pressure Tube Material,” *Metall. Mater. Trans. A*, vol. 31A, 2000.

[86] H. Li *et al.*, “Tensile deformation behaviors of Zircaloy-4 alloy at ambient and elevated temperatures: In situ neutron diffraction and simulation study,” *J. Nucl. Mater.*, vol. 446, no. 1–3, pp. 134–141, Mar. 2014, doi: 10.1016/j.jnucmat.2013.12.006.

[87] F. Xu, R. A. Holt, and M. R. Daymond, “Evidence for basal 〈a〉-slip in Zircaloy-2 at room temperature from polycrystalline modeling,” *J. Nucl. Mater.*, vol. 373, no. 1–3, pp. 217–225, Feb. 2008, doi: 10.1016/j.jnucmat.2007.05.052.

[88] P. Soo and G. T. Higgins, “THE DEFORMATION OF ZIRCONIUM-OXYGEN SINGLE CRYSTALS,” *Acta Metall.*, vol. 16, 1968, doi: 10.1016/0001-6160(68)90113-2.

[89] B. Beausir, L. S. Tóth, and K. W. Neale, “Role of strain-rate sensitivity in the crystal plasticity of hexagonal structures,” *Int. J. Plast.*, vol. 23, no. 2, pp. 227–243, Feb. 2007, doi: 10.1016/j.ijplas.2006.02.013.

[90] H. J. Bunge and I. Nielsen, “Experimental determination of plastic spin in polycrystalline materials,” *Int. J. Plast.*, vol. 13, no. 5, pp. 435–446, Jan. 1997, doi: 10.1016/S0749-6419(97)00018-1.

[91] Y. F. Dafalias and M. M. Rashid, “The effect of plastic spin on anisotropic material behavior,” *Int. J. Plast.*, vol. 5, no. 3, pp. 227–246, Jan. 1989, doi: 10.1016/0749-6419(89)90014-4.

[92] C. R. Song and G. Z. Voyiadjis, “Microstructure consideration with plastic spin and multiple back-stresses for large strain problems in soils,” *Int. J. Plast.*, vol. 18, no. 10, pp. 1271–1289, Oct. 2002, doi: 10.1016/S0749-6419(01)00069-9.

[93] H. M. Zbib and E. C. Aifantis, “On the concept of relative and plastic spins and its implications to large deformation theories. Part II: Anisotropic hardening plasticity,” *Acta Mech.*, vol. 75, no. 1, pp. 35–56, Dec. 1988, doi: 10.1007/BF01174626.

[94] H. Fan, Q. Wang, J. A. El-Awady, D. Raabe, and M. Zaiser, “Strain rate dependency of dislocation plasticity,” *Nat. Commun.*, vol. 12, no. 1, pp. 1–11, 2021, doi: 10.1038/s41467-021-21939-1.

[95] B. A. Chin, M. A. Khan, and C. L. Tarn, “Deformation and Fracture Map Methodology for Predicting Cladding Behavior During Dry Storage,” 1986. [Online]. Available: PNL-5998

[96] T. G. Langdon, “Grain boundary sliding revisited: Developments in sliding over four decades,” *J. Mater. Sci.*, vol. 41, no. 3, pp. 597–609, Feb. 2006, doi: 10.1007/s10853-006-6476-0.

[97] W. Wen, L. Capolungo, and C. N. Tomé, “Mechanism-based modeling of solute strengthening: Application to thermal creep in Zr alloy,” *Int. J. Plast.*, vol. 106, pp. 88–106, 2018, doi: https://doi.org/10.1016/j.ijplas.2018.03.003.

[98] S. S. Vagarali and T. G. Langdon, “Deformation mechanisms in h.c.p. metals at elevated temperatures—I. Creep behavior of magnesium,” *Acta Metall.*, vol. 29, no. 12, pp. 1969–1982, Dec. 1981, doi: 10.1016/0001-6160(81)90034-1.

[99] N. K. Sinha, “Limitations of stress relaxation tests for determining stress dependence of strain rate at high temperatures,” *Scr. Mater.*, vol. 48, no. 6, pp. 731–736, 2003, doi: 10.1016/S1359-6462(02)00535-3.
[100] K. Kamimura, N. Kohno, K. Ito, and Y. Tsukada, “Thermal creep tests of BWR and PWR spent fuel cladding,” in *Storage of Spent Fuel from Power Reactors*, 2003, pp. 375–385.
[101] A. Zubelewicz, “Mechanisms-based transitional viscoplasticity,” *Crystals*, vol. 10, no. 3, 2020, doi: 10.3390/cryst10030212.
[102] J. H. Moon, P. E. Cantonwine, K. R. Anderson, S. Karthikeyan, and M. J. Mills, “Characterization and modeling of creep mechanisms in Zircaloy-4,” *J. Nucl. Mater.*, vol. 353, no. 3, pp. 177–189, Jul. 2006, doi: 10.1016/j.jnucmat.2006.01.023.
[103] B. M. Morrow, R. W. Kozar, K. R. Anderson, and M. J. Mills, “An examination of the use of the Modified Jogged-Screw model for predicting creep behavior in Zircaloy-4,” *Acta Mater.*, vol. 61, no. 12, pp. 4452–4460, Jul. 2013, doi: 10.1016/j.actamat.2013.04.014.
[104] J. L. Derep, S. Ibrahim, R. Rouby, and G. Fantozzi, “Deformation behaviour of zircaloy-4 between 77 and 900 K,” *Acta Metall.*, vol. 28, no. 5, pp. 607–619, May 1980, doi: 10.1016/0001-6160(80)90127-3.
[105] E. R. Gilbert, S. A. Duran, and A. L. Bemen, “Creep of Zirconium from 50 to 850 C,” presented at the ASTM Special Technical Publication, 1969, pp. 210–225. doi: 10.1520/STP43829S.
[106] B. Ramaswami and G. B. Craig, “Thermally Activated Deformation of Alpha Zirconium,” *Metall. Soc. Am. Inst. Min. Metall. Pet. Eng.*, vol. 239, pp. 1226–1231, 1967.
[107] A. Sarkar and J. K. Chakravartty, “Activation Volume and Density of Mobile Dislocations in Plastically Deforming Zr-1pctSn-1pctNb-0.1pctFe Alloy,” *Metall. Mater. Trans. A*, vol. 46, no. 12, pp. 5638–5643, Dec. 2015, doi: 10.1007/s11661-015-3153-4.
[108] N. Balasubramanian and J. C. M. Li, “The activation areas for creep deformation,” *J. Mater. Sci.*, vol. 5, no. 5, pp. 434–444, May 1970, doi: 10.1007/BF00550006.
[109] A. G. Evans and R. D. Rawlings, “The thermally activated deformation of crystalline materials,” *Phys. Status Solidi*, vol. 34, no. 1, pp. 9–31, 1969.
[110] D. Caillard and J. L. Martin, Eds., “Chapter 5 - Dislocation Cross-slip,” in *Pergamon Materials Series*, vol. 8, Pergamon, 2003, pp. 127–156. doi: 10.1016/S1470-1804(03)80035-4.
[111] Y. Li, G. Po, Y. Cui, and N. Ghoniem, “Prismatic-to-basal plastic slip transition in zirconium,” *Acta Mater.*, vol. 242, Jan. 2023, doi: 10.1016/j.actamat.2022.118451.
[112] A. Sarkar, A. H. Alsabbagh, and K. L. Murty, “Investigation of microstructure and mechanical properties of low dose neutron irradiated HT-9 steel,” *Ann. Nucl. Energy*, vol. 65, pp. 91–96, Mar. 2014, doi: 10.1016/j.anucene.2013.11.008.
[113] C. Nam, B.-K. Choi, M.-H. Lee, and Y.-H. Jeong, “Creep strength of Zircaloy-4 cladding depending on applied stress and annealing temperature,” *J. Nucl. Mater.*, vol. 305, no. 1, pp. 70–76, Sep. 2002, doi: 10.1016/S0022-3115(02)00917-0.
[114] I. Eipert, G. Sivaswamy, R. Bhattacharya, M. Amir, and P. Blackwell, “Improvement in ductility in commercially pure titanium alloys by stress relaxation at room temperature,” *Key Eng. Mater.*, vol. 611–612, pp. 92–98, 2014, doi: 10.4028/www.scientific.net/KEM.611-612.92.
[115] A. Varma, A. Gokhale, J. Jain, K. Hariharan, P. Cizek, and M. Barnett, “Investigation of stress relaxation mechanisms for ductility improvement in SS316L,” *Philos. Mag.*, vol. 98, no. 3, pp. 165–181, 2018, doi: 10.1080/14786435.2017.1398422.

[116] A. Varma, A. Gokhale, H. Krishnaswamy, D. K. Banerjee, and J. Jain, "Grain boundary sliding and non-constancy strain during stress relaxation of pure Mg," *Mater. Sci. Eng. A*, vol. 817, no. May, pp. 141349–141349, 2021, doi: 10.1016/j.msea.2021.141349.
[117] Y. Yang *et al.*, "Stress-relaxation ageing behavior and microstructural evolution under varying initial stresses in an Al–Cu alloy: Experiments and modeling," *Int. J. Plast.*, vol. 127, p. 102646, Apr. 2020, doi: 10.1016/j.ijplas.2019.102646.
[118] K. Hariharan, P. Dubey, and J. Jain, "Time dependent ductility improvement of stainless steel SS 316 using stress relaxation," *Mater. Sci. Eng. A*, vol. 673, pp. 250–256, 2016, doi: 10.1016/j.msea.2016.07.074.
[119] K. Okazaki, Y. Aono, and M. Kagawa, "Mobile dislocations during stress relaxation in an Fe-0.056 at. % Ti alloy," *Acta Metall.*, vol. 24, no. 12, pp. 1121–1130, Dec. 1976, doi: 10.1016/0001-6160(76)90029-8.
[120] R. M. Mach, "An Accelerated Creep Testing Program For Nickel Based Superalloys," 2020.
[121] Y.-I. Jung, Y.-N. Seol, B.-K. Choi, and J.-Y. Park, "Behavior of stress–relaxation and the estimation of creep in Zr–1.1Nb–0.05Cu alloy," *Mater. Des.*, vol. 42, pp. 118–123, Dec. 2012, doi: 10.1016/j.matdes.2012.05.045.
[122] R. E. Medrano, "On stress relaxation of zirconium tubing," *J. Nucl. Mater.*, vol. 60, no. 3, pp. 306–312, Jun. 1976, doi: 10.1016/0022-3115(76)90144-6.
[123] K. S. Rheem, C. B. Choi, and W. K. Park, "Stress Relaxation Behavior of Cold-worked and Annealed Zircaloy-4 Tubing," *Nucl. Eng. Technol.*, vol. 8, no. 4, pp. 203–207, 1976.
[124] A. R. Causey, F. J. Butcher, and S. A. Donohue, "Measurement of irradiation creep of zirconium alloys using stress relaxation," *J. Nucl. Mater.*, vol. 159, pp. 101–113, Oct. 1988, doi: 10.1016/0022-3115(88)90088-8.
[125] D. E. Fraser, "STRESS RELAXATION TESTING OF SMALL BENT BEAMS: AN EVALUATION OF SOME OUT OF-PILE TESTS." Atomic Energy of Canada Limited, 1971. [Online]. Available: https://inis.iaea.org/collection/NCLCollectionStore/_Public/02/008/2008191.pdf
[126] ASTM, *Standard Specification for Wrought Zirconium and Zirconium Alloy Seamless and Welded Tubes for Nuclear Service (Except Nuclear Fuel Cladding)*, 2022.
[127] APS, "X-ray Laue Diffraction Microscopy in 3D at 34-ID-E." [Online]. Available: https://www.aps.anl.gov/Sectors-33-34/34-ID-E
[128] J. D. Budai *et al.*, "Polychromatic X-ray micro- and nanodiffraction for spatially-resolved structural studies," *Proc. EMRS 2007 Fall Meet. Symp. H Curr. Trends Opt. X-Ray Metrol. Adv. Mater. Devices II Wars. Pol.*, vol. 516, no. 22, pp. 8013–8021, Sep. 2008, doi: 10.1016/j.tsf.2008.04.045.
[129] W. Liu, G. E. Ice, B. C. Larson, W. Yang, J. Z. Tischler, and J. D. Budai, "The Three-Dimensional X-ray Crystal Microscope: A New Tool for Materials Characterization," 2004.
[130] R. Barabash, *Strain and Dislocation Gradients from Diffraction*. IMPERIAL COLLEGE PRESS, 2014. doi: 10.1142/p897.
[131] F. Dunne and N. Petrinic, *Introduction to Computational Plasticity*. Oxford University Press, 2005.
[132] B. Beausir and J. J. Fundenberger, "Analysis Tools for Electron and X-ray diffraction," *ATEX-Softw.*, 2017, [Online]. Available: www.atex-software.eu
[133] J.-Y. Kang, S.-J. Park, and M.-B. Moon, "Phase Analysis on Dual-Phase Steel Using Band Slope of Electron Backscatter Diffraction Pattern," *Microsc. Microanal.*, vol. 19, no. S5, pp. 13–16, Aug. 2013, doi: 10.1017/S1431927613012233.

[134] M. Nelson, S. Samuha, D. Kamerman, and P. Hosemann, “Temperature-Dependent Mechanical Anisotropy in Textured Zircaloy Cladding,” *J. Nucl. Mater.*, vol. 595, p. 155045, Jul. 2024, doi: 10.1016/j.jnucmat.2024.155045.
[135] M. Nelson *et al.*, “Deformation Microstructure in Stress Relieved Zircaloy-4 Cladding,” *Mater. Des.*, vol. Unpublished Work, Submitted, 2024, doi: https://ssrn.com/abstract=4909725.
[136] S.-F. Chen, H.-W. Song, S.-H. Zhang, M. Cheng, C. Zheng, and M.-G. Lee, “An effective Schmid factor in consideration of combined normal and shear stresses for slip/twin variant selection of Mg-3Al-1Zn alloy,” *Scr. Mater.*, vol. 167, pp. 51–55, 2019, doi: 10.1016/j.scriptamat.2019.03.026.
[137] C. Guo, Y. Xiao, and R. Xin, “Evaluation of Twinning Behavior in Rolling of Mg Alloys with Three Kinds of Textures by a Generalized Schmid Factor,” *Met. Mater. Int.*, vol. 26, no. 9, pp. 1366–1372, 2020, doi: 10.1007/s12540-019-00378-0.
[138] B. Wu, L. Song, G. Wan, X. Du, J. Muller, and C. Esling, “Distribution of Generalized Schmid Factor in Euler Orientation Space and Rollability of AZ31B Alloy with Basal Texture,” *J. Mater. Eng. Perform.*, vol. 29, no. 12, pp. 8145–8155, 2020, doi: 10.1007/s11665-020-05279-7.
[139] P. Bouffioux and N. Rupa, “Impact of Hydrogen on Plasticity and Creep of Unirradiated Zircaloy-4 Cladding Tubes,” in *Zirconium in the Nuclear Industry: Twelfth International Symposium*, ASTM International, 2000, pp. 399–420.
[140] K. J. Geelhood, C. E. Beyer, and W. G. Luscher, “PNNL Stress/Strain correlation for Zircaloy,” Pacific Northwest National Laboratory, PNNL-17700, 2008.
[141] M. Le Saux, J. Besson, S. Carassou, C. Poussard, and X. Averty, “A model to describe the anisotropic viscoplastic mechanical behavior of fresh and irradiated Zircaloy-4 fuel claddings under RIA loading conditions,” *J. Nucl. Mater.*, vol. 378, no. 1, pp. 60–69, 2008, doi: 10.1016/j.jnucmat.2008.04.017.
[142] MatWeb, “Zircaloy-4 Zirconium Alloy,” 2022. [Online]. Available: https://www.matweb.com/search/DataSheet.aspx?MatGUID=e36a9590eb5945de94d89a35097b7faa
[143] R. K. McGeary and B. Lustman, “Preferred Orientation in Zirconium,” *Trans AIMME*, vol. 191, 1959, [Online]. Available: 994-1002
[144] R. L. Mehan, “Modulus of Elasticity of Zircaloy-2 Between Room Temperature and 1000°F,” 1958. [Online]. Available: KAPL-M-RLM-16
[145] Z. Pan, N. Wang, and Z. He, “MEASUREMENTS OF ELASTIC MODULUS IN ZR ALLOYS FOR CANDU APPLICATIONS,” in *11th International Conference on CANDU Fuel,* 2010.
[146] M. Paredes and T. Wierzbicki, “On mechanical response of Zircaloy-4 under a wider range of stress states: From uniaxial tension to uniaxial compression,” *Int. J. Solids Struct.*, vol. 206, pp. 198–223, 2020, doi: 10.1016/j.ijsolstr.2020.09.007.
[147] H. Rosinger, I. Ritchie, and A. Shillinglaw, “Young’s Modulus of Crystal Bar Zirconium and Zirconium Alloys [Zircaloy-2, Zircaloy-4, Zirconium-2.5wt% Niobium] to 1000K,” 1975.
[148] H. A. Saller, R. F. Dickerson, and E. L. Foster, “Induction-Melted Zirconium and Zirconium Alloys,” 1954. [Online]. Available: BMI-908
[149] P. B. Scott, “Physical and Mechanical Properties of Zircaloy -2 and -4,” 1965.

[150] F. R. Shober, Et. Al, and E. Al., “The Mechanical Properties of Zirconium and Zircaloy-2,” 1957. [Online]. Available: BMI-1168
[151] G. E. Zima, “A REVIEW OF THE PROPERTIES OF ZIRCALOY-2,” 1959.
[152] E. B. Schwenk, K. R. Wheeler, G. D. Shearer, and R. T. Webster, “Poisson’s ratio in zircaloy-4 between 24° and 316°C,” *J. Nucl. Mater.*, vol. 73, no. 1, pp. 129–131, 1978, doi: 10.1016/0022-3115(78)90491-9.
[153] AZOMaterials, “Zircaloy-4(Alloy Zr4) (UNS R60804),” 2022. [Online]. Available: https://www.azom.com/article.aspx?ArticleID=7644
[154] M. Balourdet and C. Bernaudat, “Tensile Properties of Irradiated Zircatoy 4 Cladding Submitted to Fast Transient Loading,” *Proc. CSNI Spec. Meet.*, no. 96, 1995, [Online]. Available: http://www.iaea.org/inis/collection/NCLCollectionStore/_Public/29/016/29016519.pdf?r=1
[155] R. S. Daum *et al.*, “Mechanical Property Testing of Irradiated Zircaloy Cladding Under Reactor Transient Conditions,” *ASTM Spec. Tech. Publ.*, vol. Small Spec, 2002, doi: 10.1520/stp1418-eb.
[156] J. H. Huang and S. P. Huang, “Effect of hydrogen contents on the mechanical properties of Zircaloy-4,” *J. Nucl. Mater.*, vol. 208, no. 1–2, pp. 166–179, 1994, doi: 10.1016/0022-3115(94)90208-9.
[157] N. Mozzani *et al.*, “Mechanical behavior of recrystallized Zircaloy-4 under monotonic loading at room temperature: Tests and simplified anisotropic modeling,” *J. Nucl. Mater.*, vol. 447, no. 1–3, pp. 94–106, 2014, doi: 10.1016/j.jnucmat.2014.01.003.
[158] H. M. Tung, T. C. Chen, and C. C. Tseng, “Effects of hydrogen contents on the mechanical properties of Zircaloy-4 sheets,” *Mater. Sci. Eng. A*, vol. 659, pp. 172–178, 2016, doi: 10.1016/j.msea.2016.02.051.
[159] E. S. Fisher and C. J. Renken, “Single-Crystal Elastic Moduli and the hcp \ensuremath{\rightarrow} bcc Transformation in Ti, Zr, and Hf,” *Phys. Rev.*, vol. 135, no. 2A, pp. A482–A494, Jul. 1964, doi: 10.1103/PhysRev.135.A482.
[160] Z. N. Yang, F. C. Zhang, Y. Y. Xiao, and Z. G. Yan, “Dynamic recovery: The explanation for strain-softening behaviour in Zr–2.3Nb alloy,” *Scr. Mater.*, vol. 67, no. 12, pp. 959–962, Dec. 2012, doi: 10.1016/j.scriptamat.2012.08.026.
[161] F. Xu, R. A. Holt, and M. R. Daymond, “Modeling texture evolution during uni-axial deformation of Zircaloy-2,” *J. Nucl. Mater.*, vol. 394, no. 1, pp. 9–19, Oct. 2009, doi: 10.1016/j.jnucmat.2009.07.006.
[162] A. J. de O. Zimmermann and A. F. Padilha, “Rolling and recrystallization behavior of pure zirconium and zircaloy-4,” *Rev. Mater.*, vol. 24, no. 3, 2019, doi: 10.1590/S1517-707620190003.0767.
[163] M. Nelson, S. Samuha, B. Kombaiah, D. Kamerman, and P. Hosemann, “Enhanced Stress Relaxation Behavior via Basal <a> Activity from Internal Pressure Loading in Zircaloy-4 Cladding,” *J. Nucl. Mater.*, vol. Unpublished Work, Submitted, 2024, doi: http://dx.doi.org/10.2139/ssrn.4838638.
[164] C. Albrecht, A. Hunter, A. Kumar, and I. J. Beyerlein, “A phase field model for dislocations in hexagonal close packed crystals,” *J. Mech. Phys. Solids*, vol. 137, p. 103823, Apr. 2020, doi: 10.1016/j.jmps.2019.103823.

[165] S. Aubry, M. Rhee, G. Hommes, V. V. Bulatov, and A. Arsenlis, “Dislocation dynamics in hexagonal close-packed crystals,” *J. Mech. Phys. Solids*, vol. 94, pp. 105–126, Sep. 2016, doi: 10.1016/j.jmps.2016.04.019.
[166] C. M. Allison *et al.*, “SCDAP/RELAP5/MOD3.1 Code Manual, Volume IV: MATPRO-A Library of Materials Properties for Light-Water-Reactor Accident Analysis,” Idaho National Engineering Laboratory, NUREG/CR-6150, EGG-2720, 1993.
[167] L. Siefken, E. Coryell, E. Harvego, and J. Hohorst, “SCDAP/RELAP5/MOD3.3 Code Manual: MATPRO-A Library of Materials Properties for Light-Water-Reactor Accident Analysis,” U.S. Nuclear Regulatory Commission, NUREG/CR-6150, Vol.4, Rev.2, 2001.
[168] Y. Matsuo, “Thermal Creep of Zircaloy-4 Cladding under Internal Pressure,” *J. Nucl. Sci. Technol.*, vol. 24, no. 2, pp. 111–119, Feb. 1987.
[169] N. E. Hoppe, “Engineering model for zircaloy creep and growth,” in *Proceedings of the ANS-ENS International Topical Meeting on LWR Fuel Performance*, Avignon, France, Apr. 1991, pp. 157–172.
[170] E. Clouet, “Screw dislocation in zirconium: An ab initio study,” *Phys Rev B*, vol. 86, no. 14, p. 144104, Oct. 2012, doi: 10.1103/PhysRevB.86.144104.
[171] N. K. Sinha, “Stress exponent and primary creep parameters using single specimen and strain relaxation and recovery test,” *11th Int. Conf. Creep Fract. Eng. Mater. Struct. CREEP 2008*, vol. 510–511, pp. 450–456, Jun. 2009, doi: 10.1016/j.msea.2008.06.058.
[172] F. Kroupa, “DISLOCATION DIPOLES AND DISLOCATION LOOPS,” *J. Phys. Colloq.*, vol. 27, no. C3, pp. 154–167, 1966, doi: 10.1051/jphyscol:1966320.
[173] F. Onimus, L. Dupuy, and F. Mompiou, “In situ TEM observation of interactions between gliding dislocations and prismatic loops in Zr-ion irradiated zirconium alloys,” *Nucl. Mater. Sel. Artic. E-MRS 2011 Spring Meet.*, vol. 57, pp. 77–85, May 2012, doi: 10.1016/j.pnucene.2011.10.005.
[174] J. LaRoche, “Personal Communication,” 2022.
[175] G. M. Masters, *Renewable and Efficient Electric Power Systems, Ch6: Wind Power Systems*. 2004, p. 379.

Chapter 8 Appendices

8.1 Nuclear Energy in a Decarbonized Energy Market

Meeting variable renewable supply and consumer electricity demands without a large fraction of load following from natural gas production requires a large amount of storage to achieve an acceptably low probability of insufficient supply and blackouts. This has become increasingly feasible with advances in energy storage technologies, but the total storage capacity can be drastically reduced if nuclear power constitutes a significant fraction of the decarbonized energy market which is further reduced if reactors are capable of load following. This author and others [6], [174] highlight the additional benefit of frequency stabilization that nuclear power generation brings to the current electricity production and distribution system.

The current U.S. electrical grid primarily distributes electricity using three-phase alternating current (AC) which requires a consistent frequency within each of the several major regions. Stable electrical frequencies and voltages are important for safe and effective electricity distribution but are sensitive to any difference between supply and demand. Excess electricity production increases the frequency while insufficient production reduces frequency which both can result in phase error and power fluctuations that can damage equipment and cause blackouts [4], [174].

Electricity demand changes significantly in predictable and unpredictable ways which requires variable generation with timescales varying from the millisecond scale of power frequencies to daily or even annual trends. Generation methods vary in operational strengths and weaknesses including capitol and operational expenses, availability, response time, pollution, and environmental justice impacts. Methods that are well suited to consistent operational parameters are assigned to produce electrical “base load” while generation methods that can quickly change production with little penalty produce the “load following” portion required to meet varying demand.

Current electricity production technologies primarily use turbines to convert thermal or potential energy from sources such as coal, natural gas, nuclear reactions, or hydroelectric dams into mechanical energy provided to generators. Synchronous generators are paired with these centralized generation methods to produce most of the electricity in our current electrical grid which gives operators control over the frequency of the alternating current output [175]. This allows the generators to match the frequency of the grid and the mechanical inertia of the synchronized generators is translated to an electrical frequency inertia [174], [175]. This inertia is essential for operational stability because it helps synchronize frequencies over large distances and provides a few milliseconds for the utility to react to destabilizing events [174]. The ability to vary electricity production to match demand is called primary frequency control while the ability to match and control the grid frequency is called secondary frequency control [6].

Four energy sources exist with technologies that have demonstrated significant energy production without the harmful effects of carbon emissions: wind, solar, hydro, and nuclear. Wind turbines produce an immense amount of rotational inertia, but it cannot be converted to a frequency stabilizing inertia because most wind turbines use asynchronous generators [175]. Asynchronous generators are used in wind turbines because they are simpler, stronger, and require less maintenance than synchronous generators which are important factors for decentralized and

difficult to access wind turbines [175]. Photovoltaic cells produce direct current and cannot contribute to grid frequency stability. Hydroelectric power uses synchronous generatours and does contribute to grid frequency stabilization, but hydro resources are nearly saturated and cannot be increased to meet the growing demand of decarbonized electricity. Thus, it is imperative to increase nuclear energy production to maintain stable grid frequencies until the AC electrical grid can be replaced with decentralized electrical grids connected by high voltage direct current transmission lines.

8.2 Zry-4 Elemental Analysis

LABORATORY TESTING INC.

2331 Topaz Drive, Hatfield, PA 19440
TEL: 800-219-9095 • FAX: 800-219-9096

Certified Test Report

INE001-20-12-40476-1

Accredited Nadcap
Materials Testing Laboratory
Nondestructive Testing

SOLD TO
Idaho National Lab
P. O. Box 1625
MS 2218
Idaho Falls, ID 83415

SHIP TO
Idaho National Lab
1765 North Yellowstone Hwy.
MS 3710, Room 266
Idaho Falls, ID 83415
ATTN: Connor Woolum

CUSTOMER P.O.
PC5294889

CERTIFICATION DATE
2/5/2021

SHIP VIA
EMAIL

DESCRIPTION
Quantity: 2
Heat #: 252045
Lot #: 291437
Identified As: A, B

CHEMICAL ANALYSIS:
APPLICABLE SPECIFICATIONS: ASTM B353-12, UNS R60804
KEY: C - Conforms NC - Non-Conformance R-Report for Information

	REQUIREMENTS		- - - SAMPLE ID - - -	
ELEMENT	**MIN**	**MAX**	**A**	**B**
Al		0.0075%	0.0029%	0.0030%
B		0.00005%	<0.00001%	<0.00001%
C		0.027%	0.022%	0.018%
Ca		0.0030%	0.0015%	0.0023%
Cd		0.00005%	0.00003%	0.00004%
Co		0.0020%	<0.0001%	<0.0001%
Cr	0.07%	0.13%	0.11%	0.10%
Cu		0.0050%	<0.0001%	<0.0001%
Fe	0.18%	0.24%	0.19%	0.18%
Fe+Cr	0.28%	0.37%	0.30%	0.28%
H		0.0025%	0.0017%	0.0016%
Hf		0.010%	0.001%	0.001%
Mg		0.0020%	<0.0001%	0.0009%
Mn		0.0050%	0.0019%	0.0022%
Mo		0.0050%	0.0002%	0.0016%
N		0.0080%	0.0027%	0.0042%
Nb		0.0100%	0.0020%	0.0015%
Ni		0.0070%	<0.0001%	<0.0001%
O			0.13%	0.13%
Si		0.0120%	0.0087%	0.0082%
Sn	1.20%	1.70%	1.22%	1.21%
Ti		0.0050%	0.0018%	0.0014%
U		0.00035%	<0.00001%	<0.00001%
W		0.010%	0.004%	0.002%
KEY (C/NC/R):			C	C

Procedures/Methods: MAS-ICP, Rev. 25, Analysis of Metals & Their Alloys by ICP; MAS-NOH, Rev. 2, Nitrogen, Oxygen & Hydrogen Analysis; MAS-ICPMS, Rev. 12, Trace Elements by ICP Mass Spectroscopy; MAS-CS, Rev. 7, Carbon and Sulfur Analysis
Date Completed: 1/22/2021, 2/5/2021

The services performed above were done in accordance with LTI's Quality System Program Manual Revision 21 dated 5/1/2019 and ISO/IEC 17025:2017. These results relate only to the items tested and this report shall not be reproduced, except in full, without the written approval of Laboratory Testing, Inc. The services provided on this certificate have been performed in conformance with the customer's purchase order requirements. L.T.I. is accredited by Nadcap for NDT and Materials Testing for the test methods and specific services as listed in the Scopes of Accreditation available at www.labtesting.com and www.eAuditNet.com. The results reported on this test report represent the actual attributes of the material tested and indicate full compliance with all applicable specification and contract requirements. This is a shared risk decision rule which the customer also has responsibility for determining acceptance of the results.

MERCURY CONTAMINATION: During the testing and inspection, the product did not come in direct contact with mercury or any of its compounds nor with any mercury containing devices employing a single boundary of containment.

NOTE: The recording of false, fictitious or fraudulent statements or entries on this document may be punishable as a felony under Federal Statutes.

Sherri L. Scheifele
QA Specialist

Sherri L Scheifele

Authorized Signature

Page 1 of 1

Figure 8-1: Elemental analysis of Zry-4 cladding used in this dissertation characterized by inductively coupled plasma mass spectrometry.

8.3 Furnace Thermal Condition and Calibration

To prevent oxidation of the cladding test sample during the high temperature tests, an argon purge of 0.1 standard liters per minute is continually supplied during the furnace heat up and throughout the pressurization test. Argon was chosen as the purge gas as it best prevented the built up of oxide layers, as seen in Figure 8-2. This shows the results of heating three test samples to 650°C and exposes them to argon, nitrogen, and air for ~24 hours. The argon purge was found to affect the sample temperature, so the argon purge was used in the temperature calibration experiment described below as well.

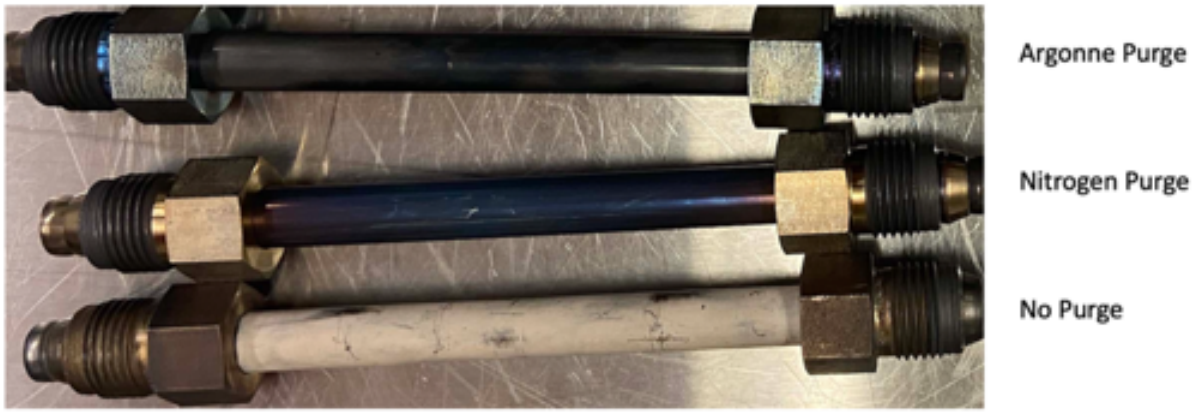

Figure 8-2: Effect of furnace atmosphere on test sample oxidation.

The thermal condition of the furnace has been characterized through a series of calibration tests. A thermal calibration sample was prepared by attaching calibrated K-type thermocouples at different axial heights to a sample as shown in Figure 8-3. The thermal axial profile was characterized at several temperatures with the 0.1 slpm argon purge as shown in Figure 8-4. These tests show a linear relationship between furnace setpoint and desired temperature in the sample test region as seen in Figure 8-5. The desired test temperature is defined as the average temperature in the test region shown in Figure 8-3. Furnace setpoints are determined by interpolating the equation in Figure 8-5 to achieve the desired testing temperature.

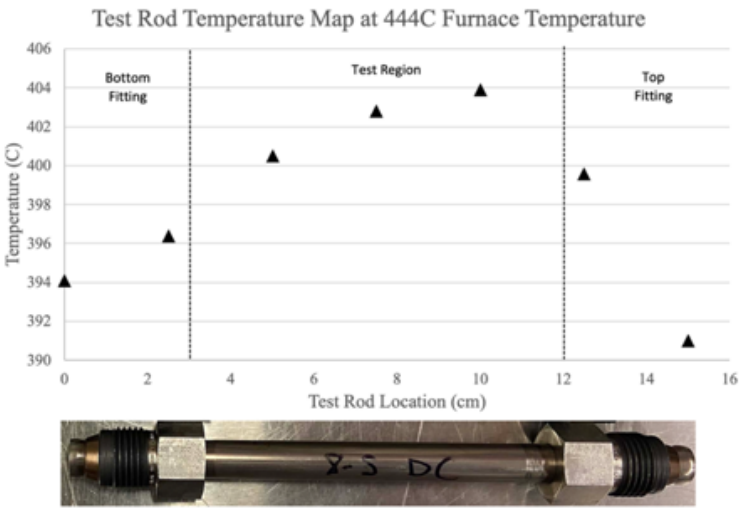

Figure 8-3: Furnace temperature map.

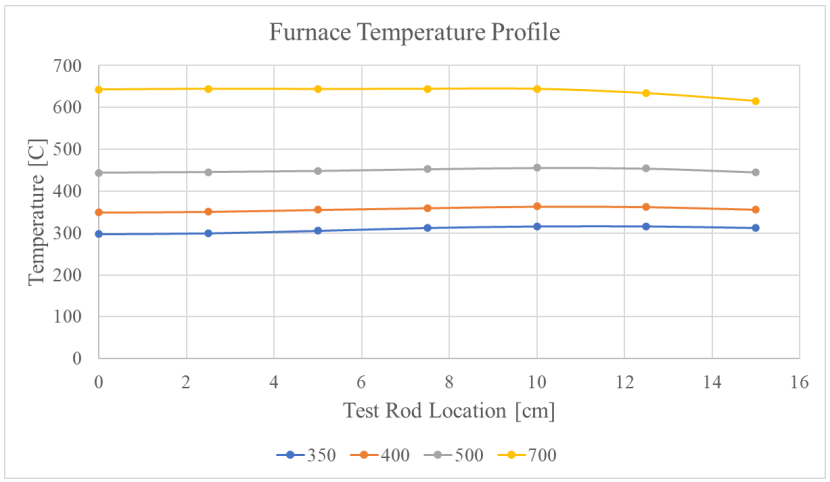

Figure 8-4: Furnace temperature profiles of tested temperature setpoints.

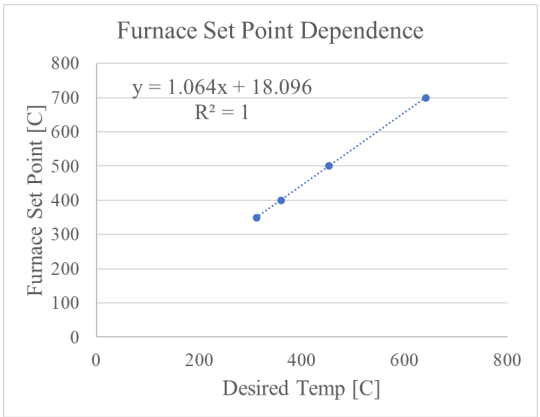

Figure 8-5: Furnace setpoint temperature dependence.

8.4 Mechanical Test Data Processing Equations

```
# True strain: gives true strain from engineering strain
    def tru_strain(eng_strain):
        tru_e = np.log(1+eng_strain)
        return(tru_e)

# Positions: gives position from initial position and true strain
    def position(init_dim, truth_strain):
        stretch = init_dim*math.exp(truth_strain)
        return(stretch)

# thin wall tube equation for capped but unconstrained cylinder
    def p_stress(p, ro, ri):
        s_z = p*ri/((ro-ri)*2)
        s_hoop = s_z*2
        s_rad = 0
        return(s_z, s_hoop, s_rad)

# Uniaxial axial tension stress equations
    def a_stress(l, ro, ri):
        xarea = np.pi*((ro**2)-(ri**2))
        s_z = l/(10**6*xarea)   #N to MPa
        s_hoop = 0
        s_rad = 0
        return(s_z, s_hoop, s_rad)


# Elastic constants from 2D stress/strain
#!!!!!!!!!!must   use   pressure   only   test   data   for   this
#relationship!!!!!!!!!!!!!!!
    def elasticity_pr(Czz, Chh):
        PR = (Chh-Czz)/(0.5*Chh-2*Czz)
        YM = Chh - PR*Chh/2
        return(PR, YM)

# axial elastic constants found using linear regression slopes of
# E = slope of sz/ez
# Elastic constants from 2D stress/strain
#!!!!!!!!!!must   use   load   only   test   data   for   this
#relationship!!!!!!!!!!!!!!!
#     def elasticity_ax(sz, ez, eh, C_int, v_int):
#         YM = (sz - C_int)/ez
#         PR = -(eh - v_int)/ez
#         return(PR, YM)
```

```
# Elastic strain calculation for any principal stresses (no imposed
#shear)
    def elas_strain(PR, YM, zs, hs, rs):
        zee = (zs - PR*hs - PR*rs)/YM
        hee = (hs - PR*zs - PR*rs)/YM
        ree = (rs - PR*hs - PR*zs)/YM
        return(zee, hee, ree)

# Mises effective Stress calculation
    def eff_stress(zs, hs, rs):
        eff_s    =    math.sqrt((((zs-hs)**2)+((hs-rs)**2)+((rs-
zs)**2))/2)
        return(eff_s)

# Equivalent Strain calculation (primarily for plastic)
    def eq_strain(ze, he, re):
        eq_e  =  math.sqrt((2/9)*(((ze-he)**2)+((he-re)**2)+((re-
ze)**2)))
        return(eq_e)
```

8.5 Additional EBSD Characterization Data from Chapter 4

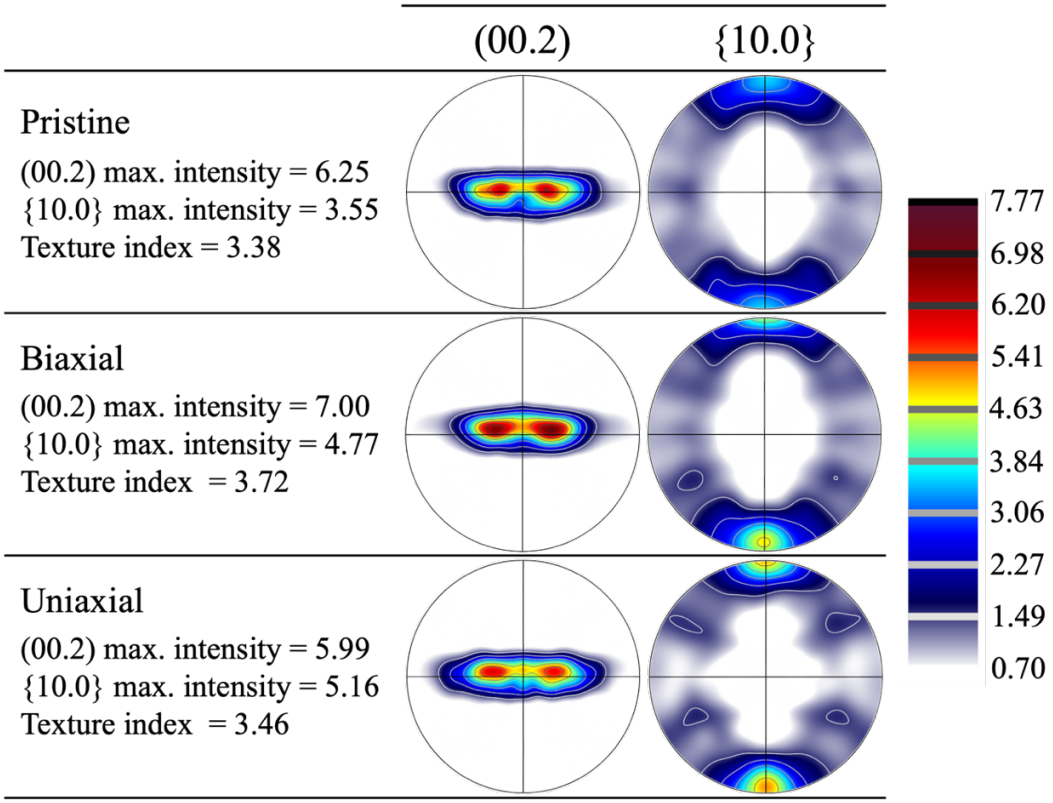

Figure 8-6: Basal (00.2) and Prismatic {10.0} pole figures of each sample characterized at 600x magnification.

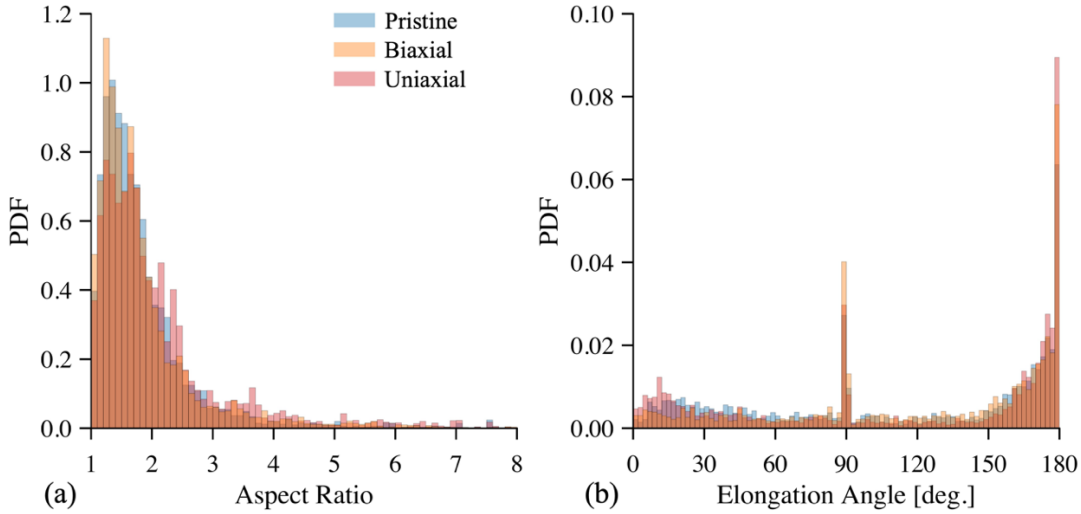

Figure 8-7: (a) Aspect ratio and (b) angle of elongated axis distributions from 600x magnification EBSD micrographs for each sample. The distributions mostly overlap displaying equivalent properties.

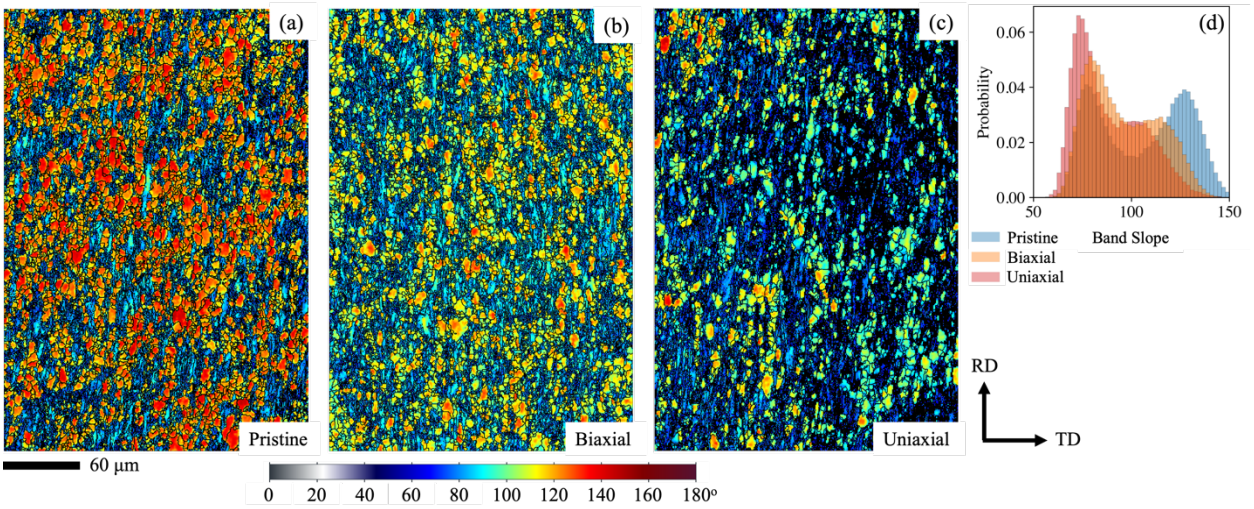

Figure 8-8: Band slope data for EBSD characterization at 600x for the (a) pristine, (b) biaxial-deformed, (c) uniaxial-deformed, and (d) histogram summary of all samples. Grain boundaries and unindexed points are shown in black.

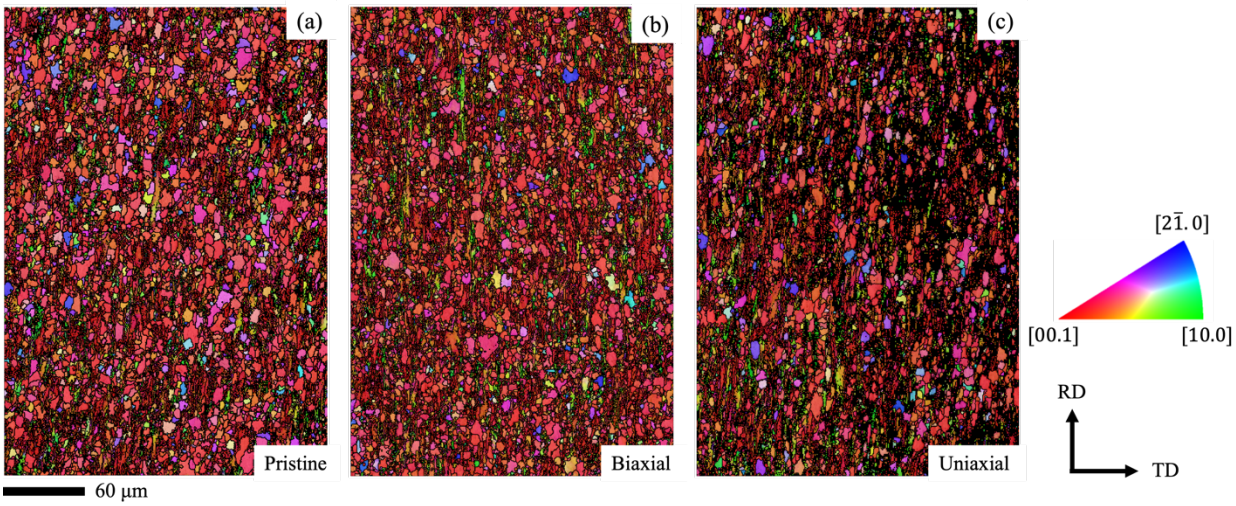

Figure 8-9: ND||IPF data for EBSD characterization at 600x for the (a) pristine, (b) biaxial-deformed, (c) uniaxial-deformed, and (d) histogram summary of all samples. Grain boundaries and unindexed points are shown in black. Color representation of this figure is available in the digital version of this paper.

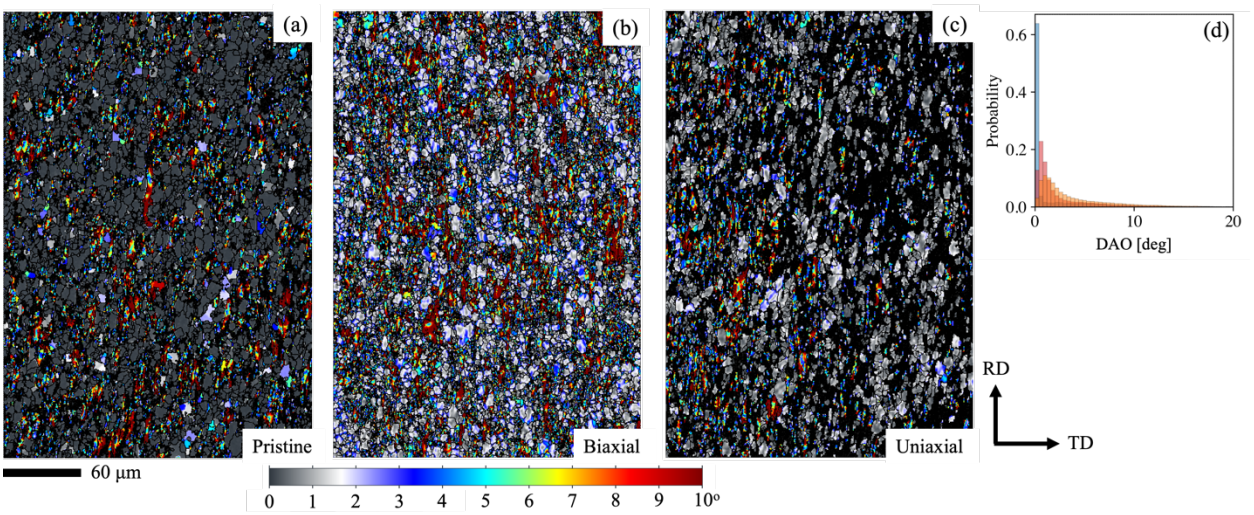

Figure 8-10: DAO data for EBSD characterization at 600x for the (a) pristine, (b) biaxial-deformed, (c) uniaxial-deformed, and (d) histogram summary of all samples. Grain boundaries and unindexed points are shown in black.

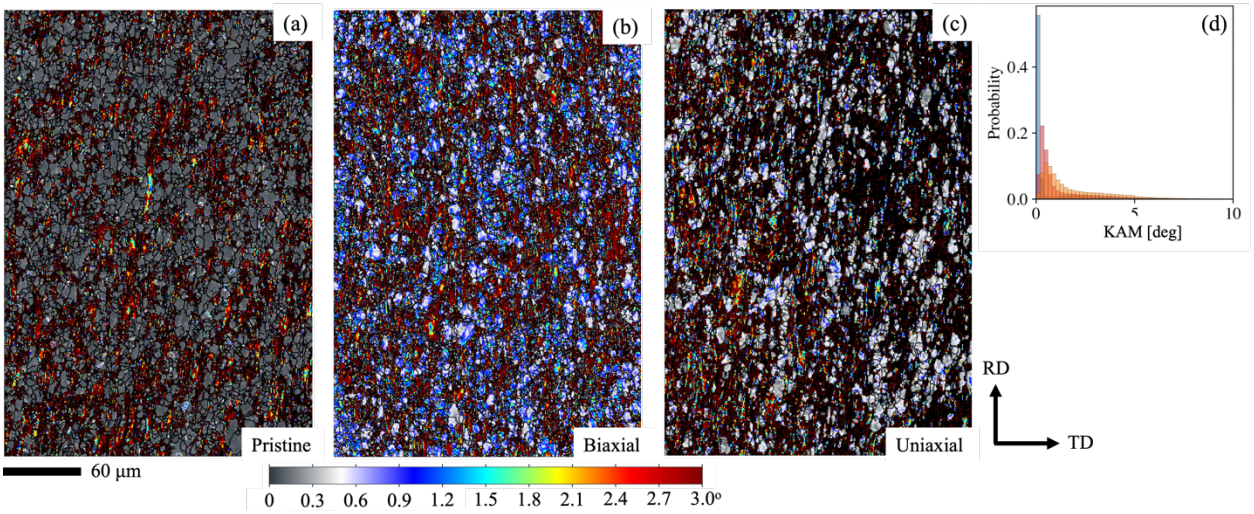

Figure 8-11: KAM data for EBSD characterization at 600x for the (a) pristine, (b) biaxial-deformed, (c) uniaxial-deformed, and (d) histogram summary of all samples. Grain boundaries and unindexed points are shown in black.

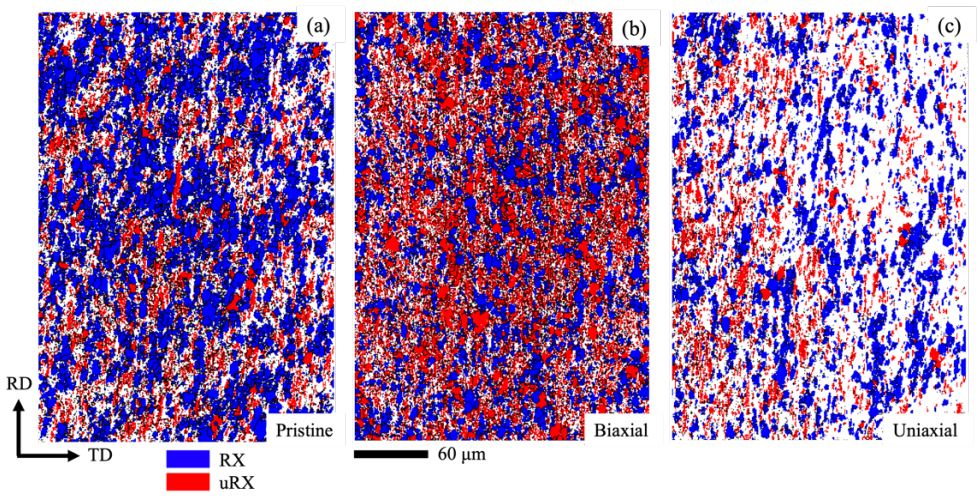

Figure 8-12: KAM based RX-uRX partitioning results for EBSD characterization at 600x for the (a) pristine, (b) biaxial-deformed, (c) uniaxial-deformed, and (d) histogram summary of all samples. Grain boundaries are shown in black and unindexed points are shown in white

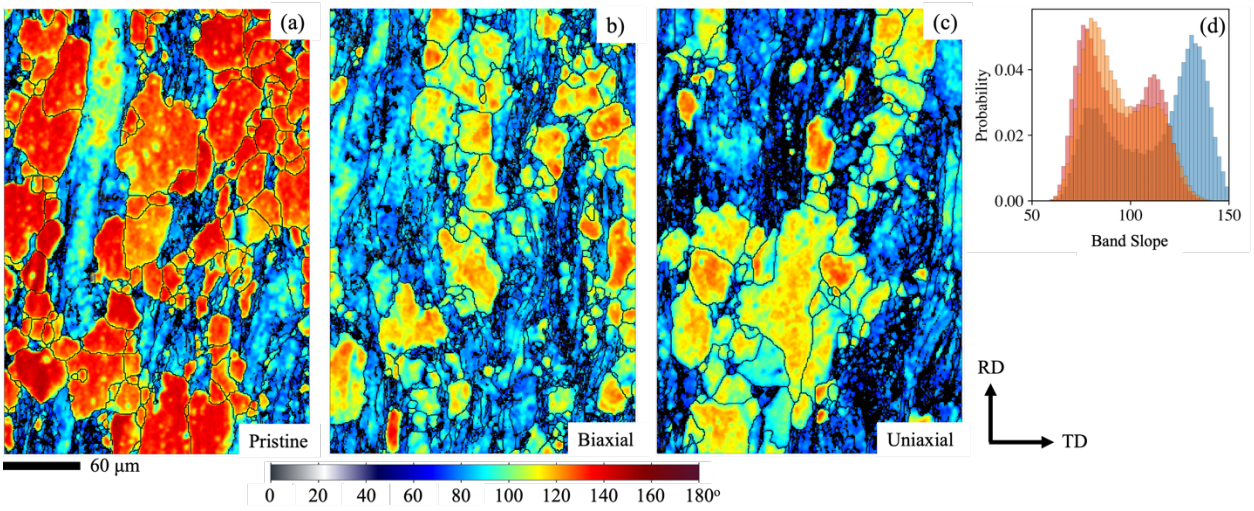

Figure 8-13: Band slope data for EBSD characterization at 4000x for the (a) pristine, (b) biaxial-deformed, (c) uniaxial-deformed, and (d) histogram summary of all samples. Grain boundaries and unindexed points are shown in black.

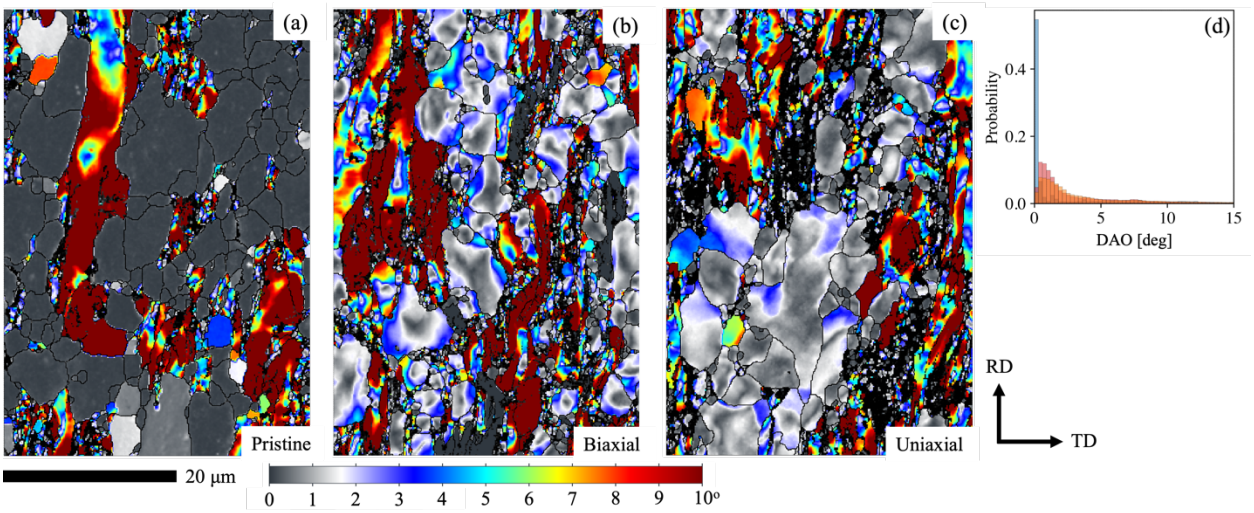

Figure 8-14: DAO data for EBSD characterization at 4000x for the (a) pristine, (b) biaxial-deformed, (c) uniaxial-deformed, and (d) histogram summary of all samples. Grain boundaries and unindexed points are shown in black.

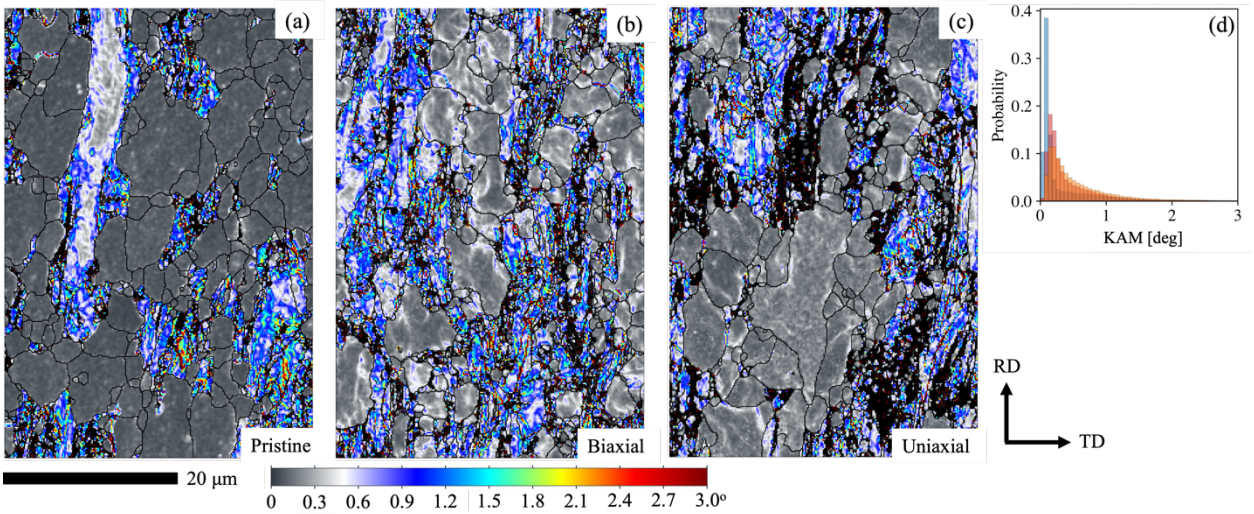

Figure 8-15: KAM data for EBSD characterization at 4000x for the (a) pristine, (b) biaxial-deformed, (c) uniaxial-deformed, and (d) histogram summary of all samples. Grain boundaries and unindexed points are shown in black.

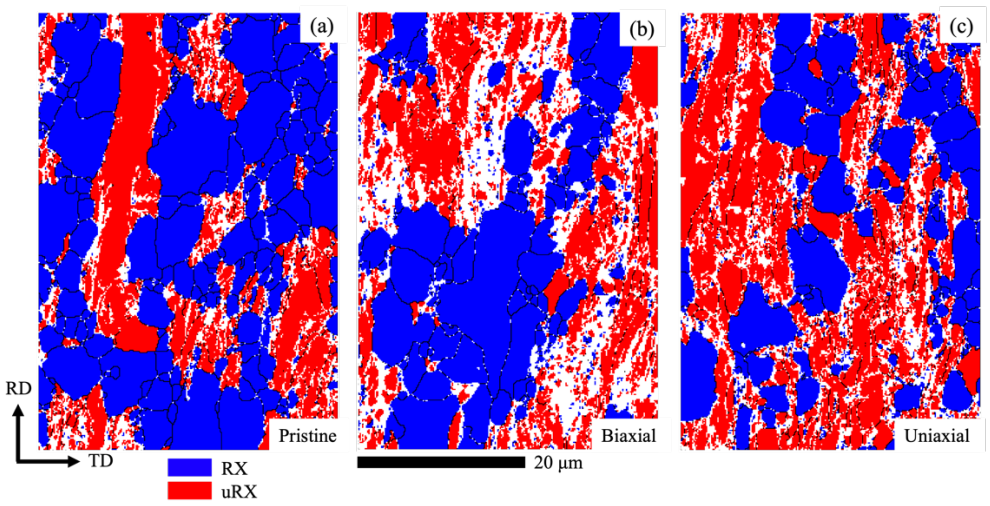

Figure 8-16: KAM based RX-uRX partitioning results for EBSD characterization at 4000x for the (a) pristine, (b) biaxial-deformed, (c) uniaxial-deformed, and (d) histogram summary of all samples. Grain boundaries are shown in black and unindexed points are shown in white.

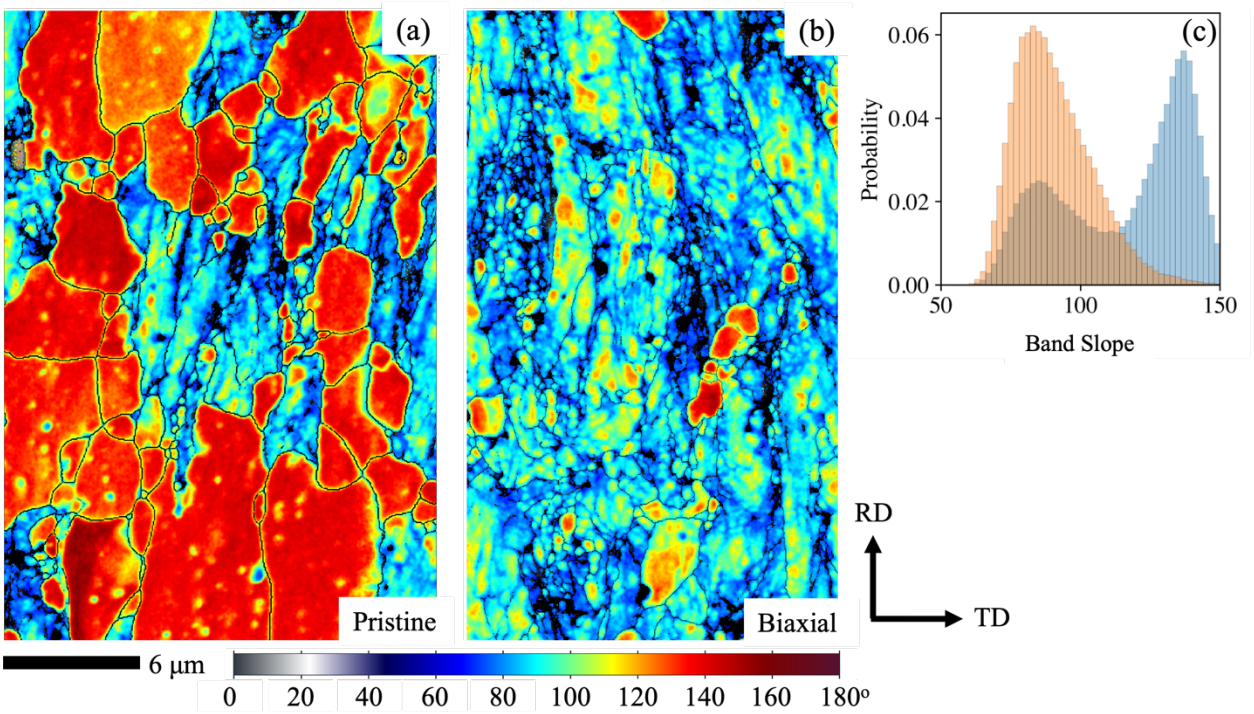

Figure 8-17: Band slope data for EBSD characterization at 7500x for the (a) pristine, (b) biaxial-deformed, (c) uniaxial-deformed, and (d) histogram summary of all samples. Grain boundaries and unindexed points are shown in black.

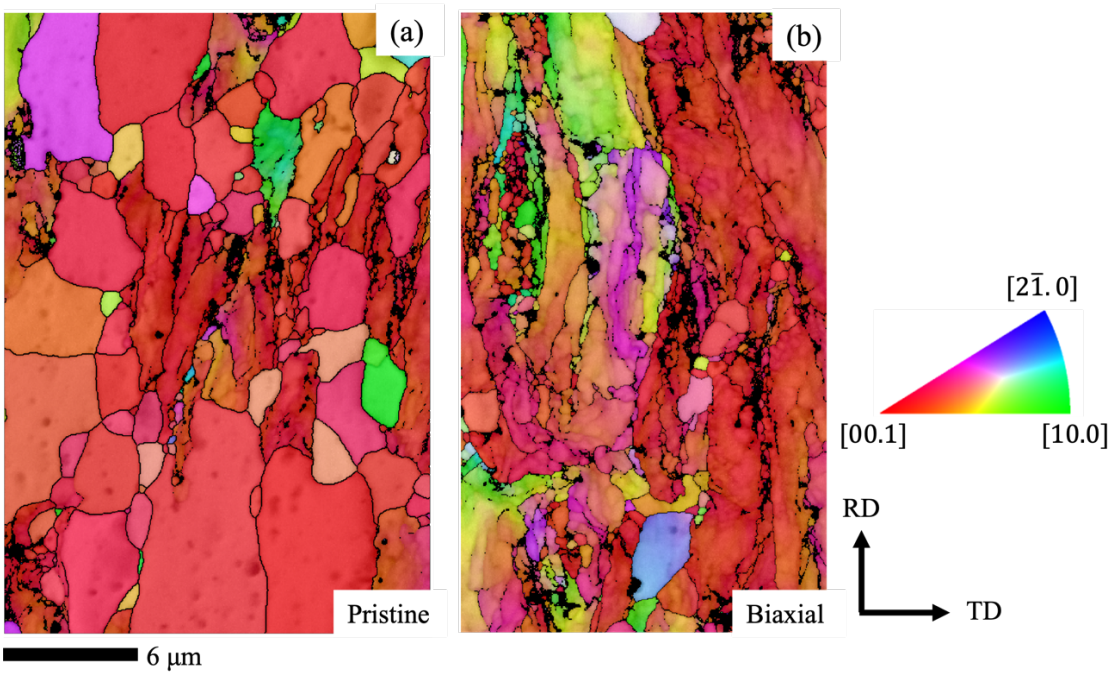

Figure 8-18: ND||IPF data for EBSD characterization at 7500x for the (a) pristine, (b) biaxial-deformed, (c) uniaxial-deformed, and (d) histogram summary of all samples. Grain boundaries and unindexed points are shown in black.

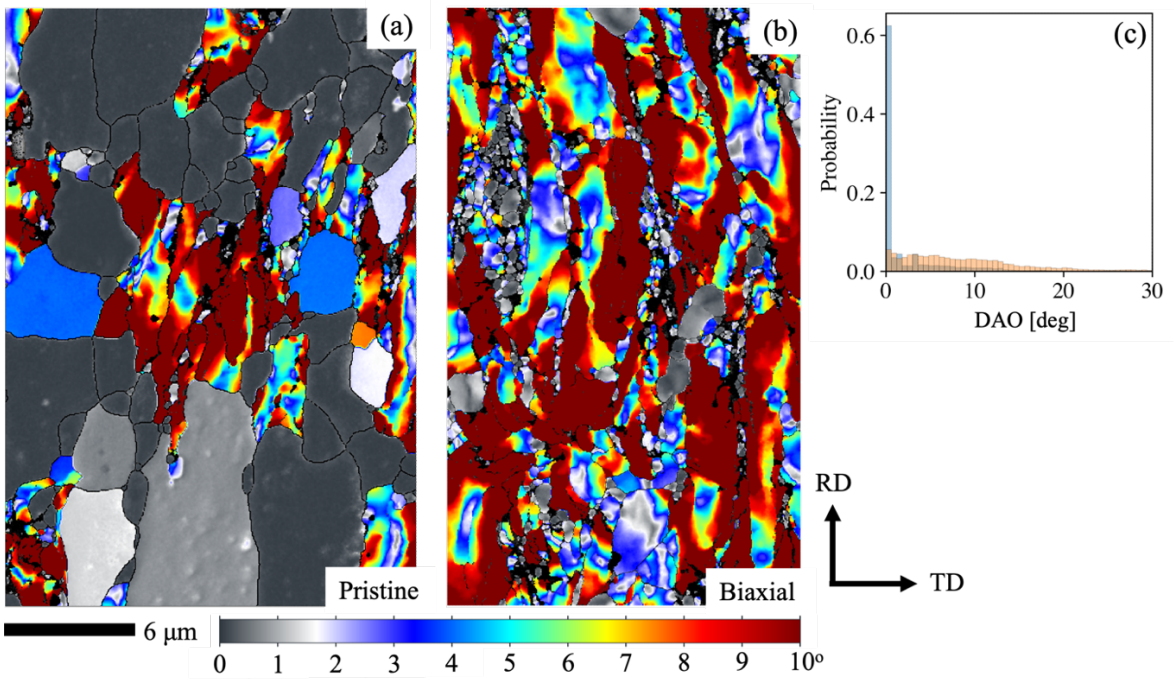

Figure 8-19: DAO data for EBSD characterization at 7500x for the (a) pristine, (b) biaxial-deformed, (c) uniaxial-deformed, and (d) histogram summary of all samples. Grain boundaries and unindexed points are shown in black.

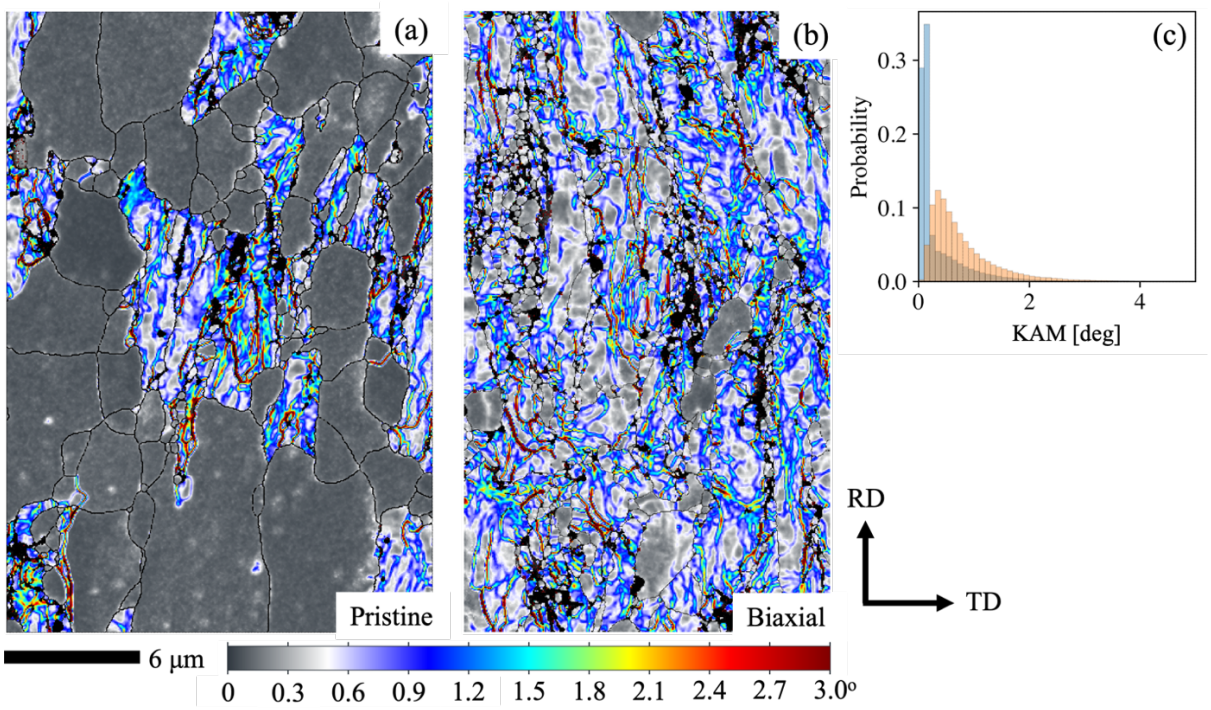

Figure 8-20: KAM data for EBSD characterization at 7500x for the (a) pristine, (b) biaxial-deformed, (c) uniaxial-deformed, and (d) histogram summary of all samples. Grain boundaries and unindexed points are shown in black.

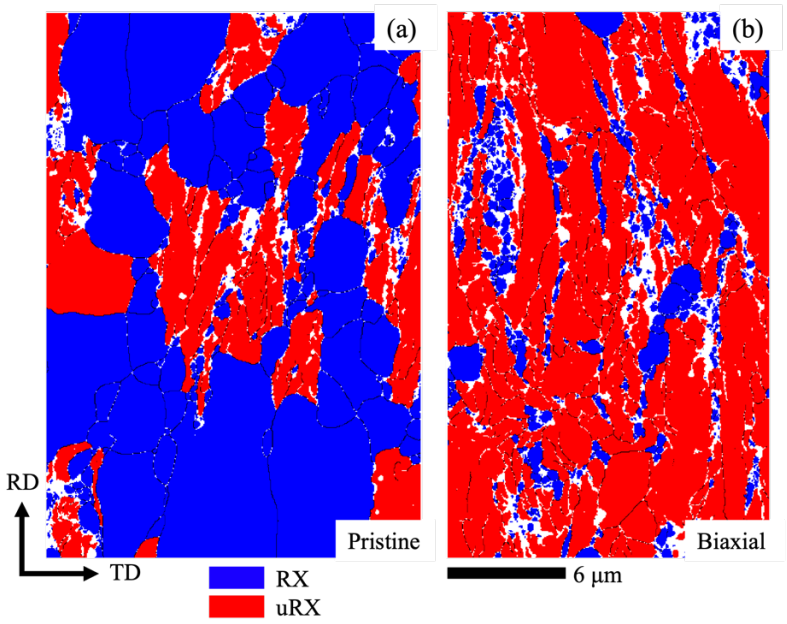

Figure 8-21: KAM based RX-uRX partitioning results for EBSD characterization at 7500x for the (a) pristine, (b) biaxial-deformed, (c) uniaxial-deformed, and (d) histogram summary of all samples. Grain boundaries are shown in black and unindexed points are shown in white.

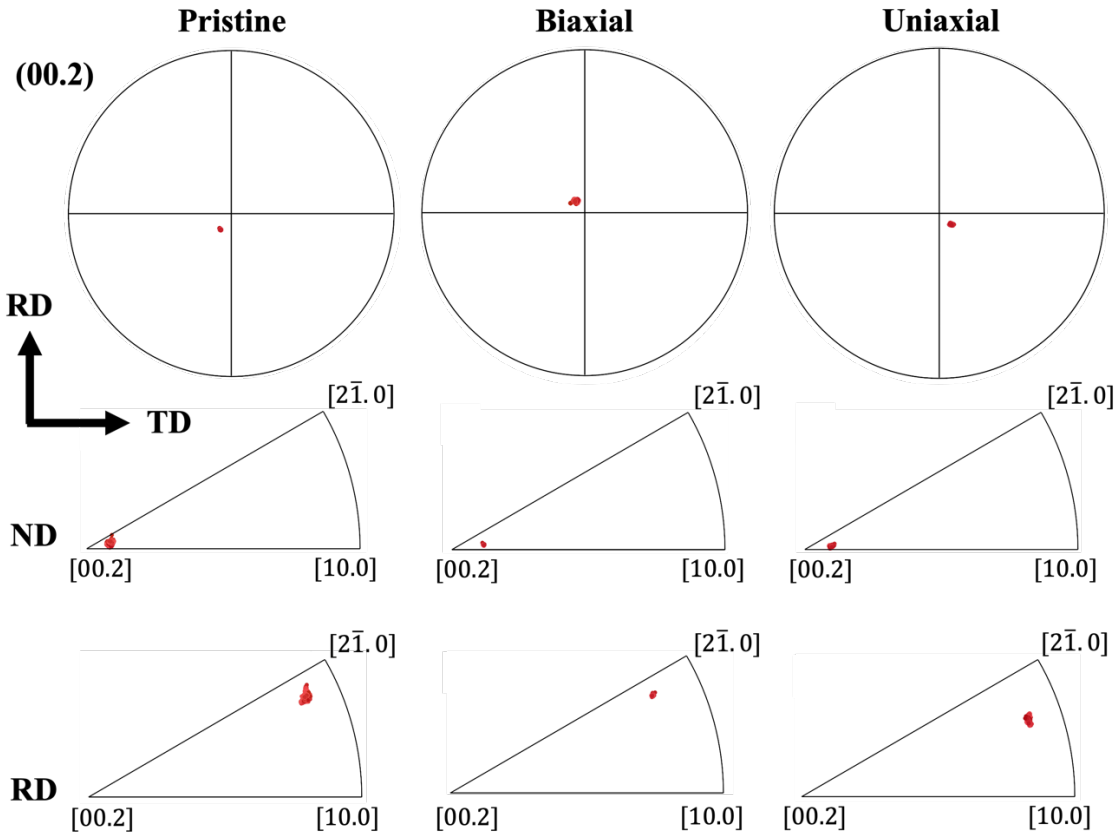

Figure 8-22: Orientations of single grains selected for EBSD analysis.

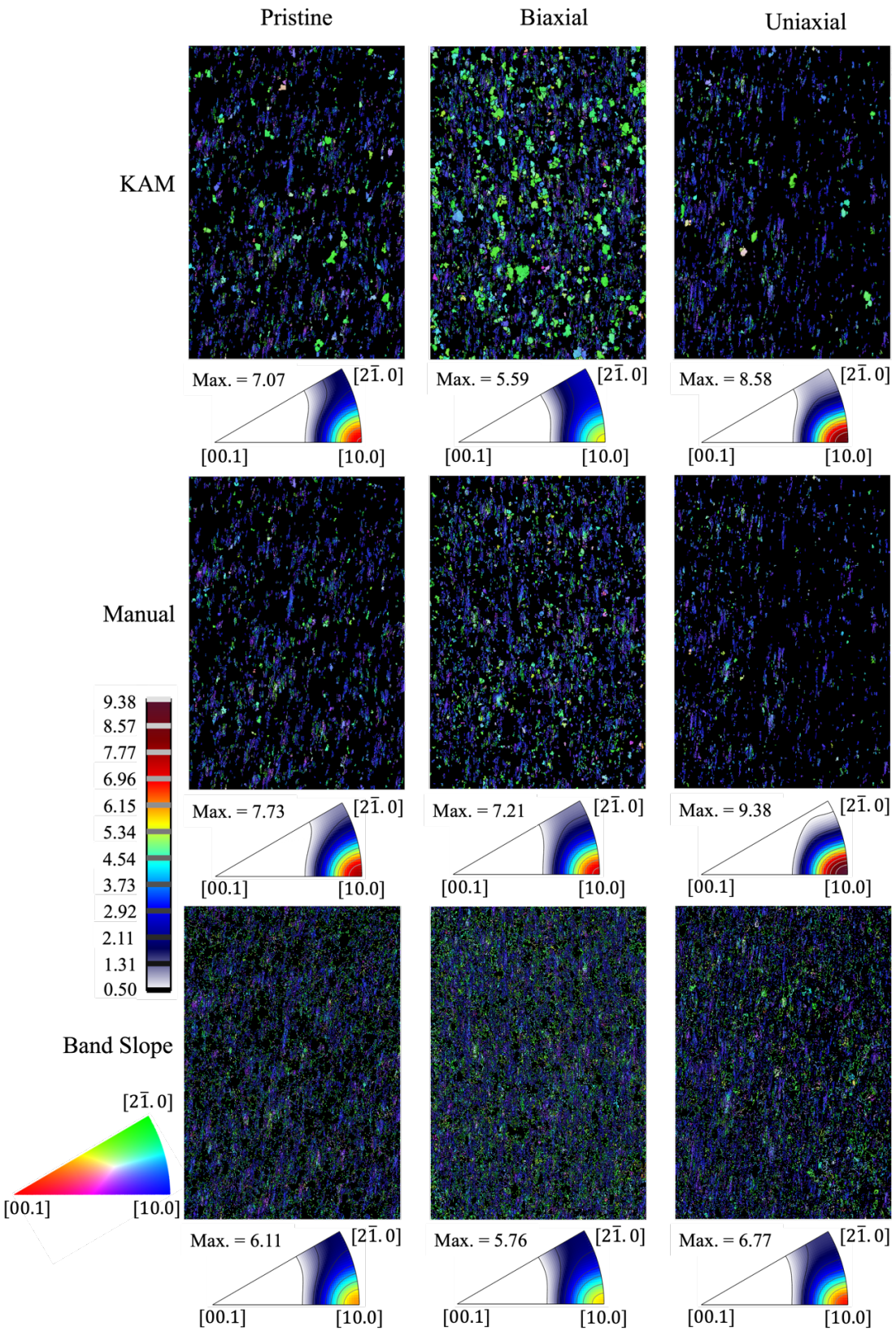

Figure 8-23: uRX partitioning of each sample and pa

8.6 FEM Input File Parameters

```
[GlobalParams]
  density = 10431.0
  initial_porosity = 0.05
  energy_per_fission = 3.2e-11 # J/fission
  displacements = 'disp_x disp_y'
  family = LAGRANGE
  order = SECOND
[]

[Problem]
  type = AugmentedLagrangianContactProblem
  reference_vector = 'ref'
  extra_tag_vectors = 'ref'
  converge_on = 'temperature disp_x disp_y'
[]
```

8.6.1 Power

```
[Functions]
  [power_history]
    type = PiecewiseLinear
    data_file = powerhistory.csv
    scale_factor = 1
  []
  [axial_peaking_factors]
    type = PiecewiseBilinear
    data_file = peakingfactors.csv
    scale_factor = 1
    axis = 1
  []
```

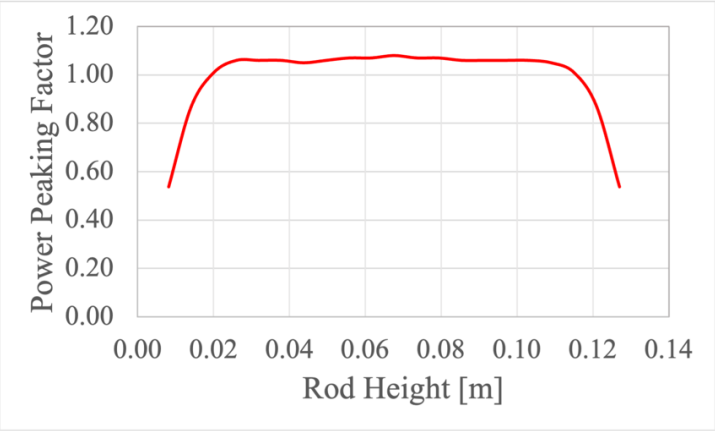

Figure 8-24: Power peaking factor normalized to the average rod linear heat generation rate.

8.6.2 Pressure

```
[ExternalPressure]
    [coolantPressure]
      boundary = '1 2 3' # cladding outer surfaces
      factor = 15.5e6
      function = pressure_ramp
    []
  []
  [pressure_ramp]
    type = PiecewiseLinear
    x = '-200 0 1e8' # time
    y = '0 1 1'      # relative reactor pressure
  []

  [PlenumPressure]
    [plenumPressure]
      boundary = 9 # all cladding inner surfaces
      initial_pressure = 2.0e6
      startup_time = 0
      R = 8.3143
      output_initial_moles = initial_moles
      temperature = ave_temp_interior
      volume = gas_volume
      material_input = fis_gas_released
      output = plenum_pressure
    []
  []
```

8.6.3 Heat Transfer

```
[CoolantChannel]
  [convective_clad_surface]
    boundary = '1 2 3'
    variable = temperature
    inlet_temperature = coolant_temp_ramp
    inlet_pressure = 15.5e6
    inlet_massflux = 3800
    rod_diameter = 9.48e-3
    rod_pitch = 1.26e-2
    linear_heat_rate = power_history
    axial_power_profile = axial_peaking_factors
  []
[]
  [coolant_temp_ramp]
    type = PiecewiseLinear
    x = '0     604800    1.00E+08'
    y = '293   550      550'
    scale_factor = 1
  []

[ThermalContact]
  [thermal_contact]
    type = GapHeatTransferLWR
    jump_distance_model = LANNING
    plenum_pressure = plenum_pressure
    variable = temperature
    primary = 5 # cladding inner surface
    secondary = 10 # pellet type 1 outer diameter
    initial_gas_types = He
    initial_fractions = 1
    roughness_coef = 1.5
    roughness_fuel = 1.0e-6
    roughness_clad = 1.0e-6
    #min_gap = 0
    emissivity_primary = 0
    emissivity_secondary = 0
    tangential_tolerance = 1e-5
  []
[]
```

8.6.4 Mechanical Contact

```
[Contact]
  [mechanical]
```

```
    primary = 5
    secondary = 10
    penalty = 6.9e10 # Approximately Young's mod @ 400C
    model =  coulomb
    formulation =  augmented_lagrange
    friction_coefficient = 0.2
    normalize_penalty = true
    tangential_tolerance = 5e-2
    normal_smoothing_distance = 0.1
    al_penetration_tolerance = 1e-6
    al_incremental_slip_tolerance = 1e-2
    al_frictional_force_tolerance = 2e-1
  []
[]
```

8.6.5 Fuel Material Models

```
[Materials]
  [fuel_thermal]
    type = UO2Thermal
    block = pellet_type_1
    thermal_conductivity_model = NFIR
    temperature = temperature
    burnup_function = burnup
  []
  [fuel_elasticity_tensor]
    type = ComputeIsotropicElasticityTensor
    block = pellet_type_1
    youngs_modulus = 2.0e11
    poissons_ratio = 0.345
  []
  [fuel_elastic_stress]
    type = ComputeFiniteStrainElasticStress
    block = pellet_type_1
  []
  [fuel_thermal_expansion]
    type = UO2ThermalExpansionMATPROEigenstrain
    block = pellet_type_1
    temperature = temperature
    stress_free_temperature = 295.0
    eigenstrain_name = fuel_thermal_strain
  []
  [fuel_relocation]
    type = UO2RelocationEigenstrain
    block = pellet_type_1
    burnup_function = burnup
    fuel_pin_geometry = fuel_pin_geometry
```

```
    rod_ave_lin_pow = power_history
    axial_power_profile = axial_peaking_factors
    burnup_relocation_stop = 0.03
    relocation_activation1 = 5000
    relocation_model = ESCORE_modified
    eigenstrain_name = fuel_relocation_strain
  []
  [fuel_volumetric_swelling]
    type = UO2VolumetricSwellingEigenstrain
    gas_swelling_model_type = SIFGRS
    block = pellet_type_1
    temperature = temperature
    burnup_function = burnup
    initial_fuel_density = 10431.0
    eigenstrain_name = fuel_volumetric_strain
  []
  [fission_gas_release]
    type = Sifgrs
    block = pellet_type_1
    temperature = temperature
    burnup_function = burnup
    grain_radius = grain_radius
    gbs_model = true
  []
```

8.6.6 Cladding Material Models

```
[clad_thermal]
    type = HeatConductionMaterial
    block = clad
    thermal_conductivity = 16.0
    specific_heat = 330.0
  []
  [clad_elasticity_tensor]
    type = ZryElasticityTensor
    block = clad
    matpro_poissons_ratio = true
    matpro_youngs_modulus = true
    temperature = temperature
    fast_neutron_fluence = fast_neutron_fluence
    cold_work_factor = 0.1
  []
  [clad_stress]
    type = ComputeMultipleInelasticStress
    tangent_operator = elastic
    inelastic_models = 'clad_plasticity'
```

```
  block = clad
[]
[clad_plasticity]
  type = ZryPlasticityUpdate
  block = clad
  temperature = temperature
  fast_neutron_flux = fast_neutron_flux
  fast_neutron_fluence = fast_neutron_fluence
  cold_work_factor = 0.1
  plasticity_model_type = PNNL
[]
[clad_zrycreep]
  type = ZryCreepLimbackHoppeUpdate
  block = clad
  temperature = temperature
  fast_neutron_flux = fast_neutron_flux
  fast_neutron_fluence = fast_neutron_fluence
  model_irradiation_creep = true
  model_primary_creep = true
  model_thermal_creep = true
[]
[thermal_expansion]
  type = ZryThermalExpansionMATPROEigenstrain
  block = clad
  temperature = temperature
  stress_free_temperature = 295.0
  eigenstrain_name = clad_thermal_eigenstrain
[]
[irradiation_swelling]
  type = ZryIrradiationGrowthEigenstrain
  block = clad
  fast_neutron_fluence = fast_neutron_fluence
  zircaloy_material_type = stress_relief_annealed
  eigenstrain_name = clad_irradiation_strain
[]
```